Twist Angle Physics in Graphene Based van der Waals Heterostructures

by

Yuanhong Luo

B.A., Cornell University (2010)
B.S., Cornell University (2010)

Submitted to the Department of Physics
in partial fulfillment of the requirements for the degree of

Doctor of Philosophy in Physics

at the

MASSACHUSETTS INSTITUTE OF TECHNOLOGY

June 2018

Author .....
Department of Physics
May 16, 2018

Certified by .....
Pablo Jarillo-Herrero
Professor of Physics
Thesis Supervisor

Accepted by .....
Scott A. Hughes
Interim Associate Department Head of Physics

Twist Angle Physics in Graphene Based van der Waals Heterostructures

by

Yuanhong Luo

Submitted to the Department of Physics
on May 16, 2018, in partial fulfillment of the
requirements for the degree of
Doctor of Philosophy in Physics

Abstract

In this thesis, I present my experimental work on twisted bilayer graphene, a van der Waals heterostructure consisting of two graphene sheets stack on top of each other. In particular, the twist angle is a new degree of freedom in this system, and has an important effect in the determination of its transport properties.

The work presented will explore the twist-dependent physics in two regimes: the large twist angle and small twist angle regimes. In the large-twist angle limit, the two sheets have little interlayer interactions and are strongly decoupled, allowing us to put independent quantum Hall edge modes in both layers. We study the edge state interactions in this system, culminating in the formation of a quantum spin Hall state in twisted bilayer graphene. In the small twist angle limit, interlayer interactions are strong and the layers are strongly hybridized. Additionally, a new long-range moiré phenomenon emerges, and we study the effects of the interplay between moiré physics and interlayer interactions on its transport properties.

Thesis Supervisor: Pablo Jarillo-Herrero
Title: Professor of Physics

Acknowledgments

The 6-year long journey for this PhD journey has not been easy, and there are many people I have to thank. Firstly, I have to show my gratitude to my advisor Pablo Jarillo-Herrero, not just for his guidance in navigating me through the field of science, but also for his compassion and humanity in some difficult phases of my life. To quote him: "We are all humans first". Thank you.

I also have to say a big thank you to my longtime teammate Javier Sanchez-Yamagishi, for imparting all his technical skills to me, and for all the tears and laughs we had along the way to complete our research and papers. But most importantly, I have to thank him for being always being a friend when I was in need. Words cannot describe how grateful I am.

I also have to thank all my lab mates who have worked with me in Pablo's group throughout these six years: Valla, Yuan, Qiong, Yafang, Joel, Dani, Mueed, and Spencer. It may have seem that I have forgotten, but I haven't. Also to my friends Zach, Ryan, Jia Shee, Ted, Helena, Danqing, Hanrong, Jingyee, Talin and Oliver. Thank you.

And also a big thanks to Monica, for always being a cheerful listening ear whenever I needed one. I can't say how much it means to me that you always cared.

I also have to thank my sister, who has been through thick and thin with me all these years. Also a shout-out to my Team Instinct Boston friends for helping me laugh when I did not necessarily feel like it, and for grounding me and keeping my sanity.

I dedicate this thesis to my mum, Lee Pei Leng, with love. I miss you very much.

THIS PAGE INTENTIONALLY LEFT BLANK

Contents

THIS PAGE INTENTIONALLY LEFT BLANK

List of Figures

Chapter 1

Introduction & Background

1.1 Thesis Introduction

In this thesis, I describe a series of experiments that explore the role of twist angle in twisted bilayer graphene, a type of van der Waals heterostructure. Twisted bilayer graphene consists of two sheets of graphene stacked on top of each other, with a relative twist between them. Although the effect of the twist angle may seem to be trivial, it turns out that the twist angle is crucial in determining the type of quantum transport observed in this system. This thesis will be divided into 4 chapters.

(1) In Chapter 1, I will provide an introduction on the physics required to understand the results of the experiments, including graphene's electronic structure and the quantum Hall effect. (2) In Chapter 2, I will detail the role of the twist angle in controlling the degree of coupling between the two graphene layers, and outline the expected quantum transport behavior in the large and small angle regimes. (3) In Chapter 3, I will present my experimental work on large twist angle twisted bilayer graphene, where we build a quantum spin Hall like state via independent control the quantum Hall edge modes in each graphene layer. (4) In Chapter 4, I will present my experimental work on small twist angle twisted bilayer graphene, where we observe a rich interplay of the effects of interlayer coupling and the emergent moiré potential.

1.2 Properties of Monolayer Graphene

Graphene is the first exfoliated two-dimensional crystal discovered in nature [1], consisting of a single layer of carbon atoms laid out in a regular honeycomb lattice. Graphene's regular honeycomb lattice allows simple derivation of its band structure to first order using the tight-binding model, and the chemical equivalence of its two sub-lattices leads to a Dirac-like dispersion (where the electron's energy goes linearly with its momentum) at low energies [2], drawing strong parallels with the relativistic massless Dirac equation. In the presence of a magnetic field, graphene's Dirac-like band leads to cyclotronic motion that are qualitatively different from two-dimensional gas systems such as silicon [3] and gallium-arsenide quantum wells [4], which were the first system used for the discovery of the integer and fraction quantum Hall effect respectively. In this section, I shall aim to describe the material and electronic properties of graphene, and develop a framework of the quantum Hall physics that results from these properties.

1.2.1 Material Properties

Graphene is an atomic thick 2-dimensional van der Waals material that was first isolated from graphite by Geim, Novoselov et. al [1] in 2004. Graphene has carbon atoms arranged in a honeycomb lattice, which can be regarded as a triangular Bravais lattice with a basis, with a lattice constant of $a = 1.42\,\text{Å}$ between adjacent carbon atoms [2]. Graphene as a material has many attractive qualities: it is a thin, highly-conducting material [5,6] which is highly flexible, but yet strong enough to withstand large mechanical and sheer stresses [7, 8]. It is also optically transparent with rich optoelectronic properties [9–11], which makes it a highly attractive material for use in many infra-red based applications.

In this thesis, the quantum electronic properties of graphene at low temperatures will be the main focus of my studies. One of the main advantages of two-dimensional materials is the ease of control of the charge density via the capacitative field effect: the number of charge carriers in the sample can be easily modulated by varying

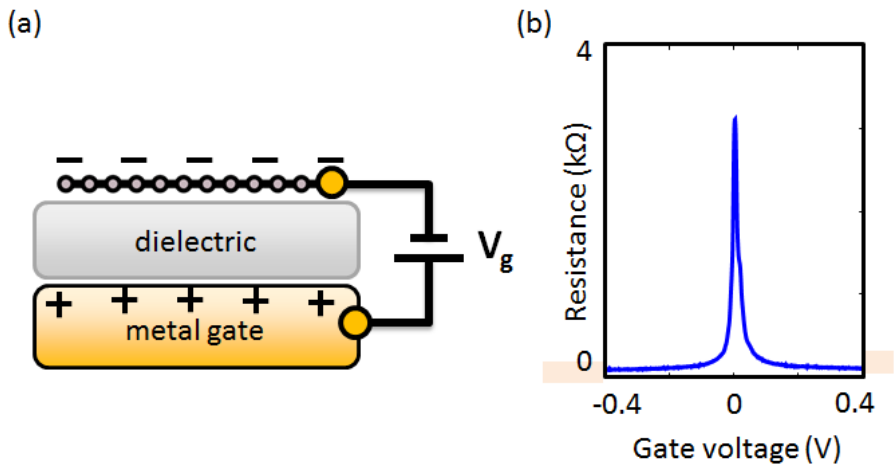

Figure 1-1: (a) Illustration of charge density modulation in two-dimensional materials via the capacitative field effect. (b) Typical 2-probe resistance trace of monolayer graphene as a function of gate voltage. The resistance reaches a maximum at the charge neutrality point.

the voltage between a metallic gate and the studied material (panel (a) of Fig. 1-1). In graphene, the lack of a band gap between the conduction and valence bands increases the ease of this process. In the course of my research, both conductive silicon substrates and evaporated metallic gates have been used to control the charge density via the field effect.

One of the key numbers that we should consider is the number density of charge carriers that we can induce in graphene via the capacitative field effect. The capacitance per area C is given by

$$C = \frac{\epsilon_r \epsilon_0}{t} \tag{1.1}$$

where t is the thickness of the dielectric, ϵ_r is the relative permittivity of the dielectric, and $\epsilon_0 = 8.85 \times 10^{-12}$ Fm^{-1} is the permittivity of free space. Thus, for a given voltage V, the number of charge carriers n we can induce is given by

$$n = \frac{C}{eV} = \frac{\epsilon_r \epsilon_0}{teV} \tag{1.2}$$

where $e = 1.602 \times 10^{-19}$ C is the elementary charge.

The two main dielectrics used in my work are silicon dioxide (which exists as

a native oxide above the conductive silicon substrate) and hexagonal boron nitride (hBN) which is also a van der Waals material [12]. For silicon oxide, the relative permittivity ranges from 3.6 to 4.2, with a typical oxide thickness of 280 nm. The breakdown electric field of silicon oxide is typically around 0.5 V/nm, allowing us to apply voltage in the range of 100 V. For hexagonal boron nitride, the relative permittivity is typically between 2.8 to 4 [13] depending on the crystal quality, and the hBN flakes used in our studies are between 10 to 50 nm. The breakdown electric field of hBN is also around 0.5 V/nm, allowing us to apply voltage in the range of 10 V. Putting these numbers together, the typical number density we can induce in graphene is in the range of $10^{12} - 10^{13}\text{cm}^{-2}$, with a corresponding Fermi energy on the order of 100 meV [2].

A typical 2-probe resistance trace vs. gate voltage for graphene is shown in panel (b) of Fig.1-1, where we observe a resistance maximum (i.e. conductance minimum) at the charge neutrality point. In many devices, inherent doping of the graphene flakes from work function mismatch [14] and the fabrication process would shift the charge neutrality point away from zero voltage. The conductance minimum is also observed to be *not* zero, which has been understood to arise from percolations through a network of electron-hole puddles due to substrate inhomogeneity and sample disorders [15]. The control of sample disorder would be a key hurdle to overcome in these studies, as they could compete with the energy scales of the electronic properties that are being studied.

1.2.2 Basic Electronic Structure

A lattice is called a Bravais lattice if it can be completely generated by a basis set of vectors B i.e. any lattice point's position vector $\vec{R}$ can be written as

$$\vec{R} = \sum_{\vec{a}_i \in B} n_i \vec{a}_i \tag{1.3}$$

where n_i is an integer.

In graphene, the lattice consists of carbon atoms laid out in a honeycomb lattice

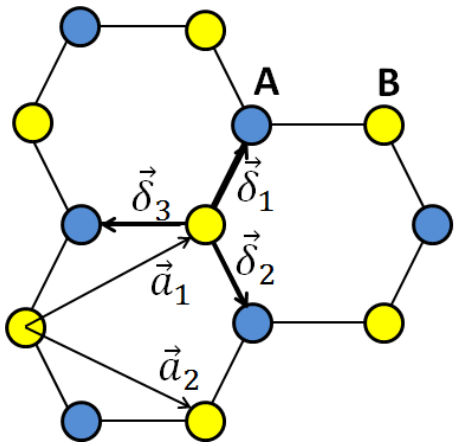

Figure 1-2: Illustration of graphene's honeycomb lattice structure. Blue and yellow carbon atoms correspond to the A and B sublattices respectively. Bravais basis vectors $\vec{a}_1$ and $\vec{a}_2$ are shown, as well as nearest neighbor displacement vectors $\vec{\delta}_i,\ i = 1, 2, 3$.

with a lattice constant $a = 1.42\,\text{Å}$. However, this is not a primitive Bravais lattice as the carbon atoms A and B in Fig.1-2 have inequivalent nearest neighbors [2]. However, one can transform it into a Bravais lattice by grouping the two atoms as a single unit, producing a triangular Bravais lattice occupied by the yellow-colored atoms only, also known as a Bravais lattice with a basis. Thus, one can describe graphene as consisting of two sub-lattices, namely the A sublattice and the B sub-lattice (colored blue and yellow respectively in Fig. 1-2). For graphene, we can define the basis set of vectors as $\vec{a}_1 = (\frac{3a}{2}, \frac{\sqrt{3}a}{2})$ and $\vec{a}_2 = (\frac{3a}{2}, \frac{\sqrt{3}a}{2})$.

We can perform a simple tight-binding calculation to obtain an approximate form of the dispersion relation of electrons in graphene. In general, the Bloch wavefunction of an electron in a crystal lattice can be written as [2]

$$|\psi_k(\vec{r})\rangle = \sum_{\vec{R}_j} e^{i\vec{k}.\vec{R}_j} \left|\phi(\vec{r} - \vec{R}_j)\right\rangle \tag{1.4}$$

where $\vec{R}_j$ is the position vector of a lattice site, and $\phi(\vec{r} - \vec{R}_j)$ represents the eigenstate of the crystal Hamiltonian at the site $\vec{R}_j$. The constructed Bloch wavefunction is easily verified to be an eigenstate of the translation operator $T(\vec{R})$:

$$
\begin{aligned}
T(\vec{R})\left|\psi_k(\vec{r})\right\rangle &= \sum_{\vec{R}_j} e^{i\vec{k}.\vec{R}_j} T(\vec{R}) \left|\phi(\vec{r}-\vec{R}_j)\right\rangle \\
&= \sum_{\vec{R}_j} e^{i\vec{k}.\vec{R}_j} \left|\phi(\vec{r}-\vec{R}_j+\vec{R})\right\rangle \\
&= e^{i\vec{k}.\vec{R}} \sum_{\vec{R}+\vec{R}} e^{i\vec{k}.(\vec{R}_j-\vec{R})} \left|\phi(\vec{r}-\vec{R}_j+\vec{R})\right\rangle \\
&= e^{i\vec{k}.\vec{R}} \left|\psi_k(\vec{r})\right\rangle
\end{aligned}
\tag{1.5}
$$

Because graphene is a Bravais lattice with a basis, we must be careful in defining the Bloch wavefunction of the electron. Without loss of generality, we can place the B sub-lattice on the sites of the triangular Bravais lattice, and define $\vec{\delta} = (-a, 0)$ as the displacement vector from atom B to A in a chosen sub-basis. Then the Bloch wavefunction of graphene can be written as

$$
\left|\psi_k(\vec{r})\right\rangle = a_{\vec{k}} \left|\psi_k(\vec{r})\right\rangle + b_{\vec{k}} \left|\psi_k(\vec{r})\right\rangle \tag{1.6}
$$

where

$$
\left|\psi_k^B(\vec{r})\right\rangle = \sum_{\vec{R}_j} e^{i\vec{k}.\vec{R}_j} \left|\phi^B(\vec{r}-\vec{R}_j)\right\rangle \tag{1.7}
$$

$$
\left|\psi_k^A(\vec{r})\right\rangle = \sum_{\vec{R}_j} e^{i\vec{k}.\vec{R}_j} \left|\phi^A(\vec{r}+\vec{\delta}-\vec{R}_j)\right\rangle \tag{1.8}
$$

represent the Bloch wavefunctions consisting of atoms at A and B sub-lattices only respectively, and $a_{\vec{k}}$, $b_{\vec{k}}$ are complex numbers in general.

We now consider the nearest hopping processes that can occur in graphene. For an A sub-lattice atom, an electron can hop to three possible nearest A sub-lattice sites with displacement vectors $\vec{\delta}_1 = \vec{a}_1 + \vec{\delta}$, $\vec{\delta}_2 = \vec{a}_2 + \vec{\delta}$, $\vec{\delta}_3 = \vec{\delta}$ relative to the B atom. The hopping energy required in this process can be calculated from methods such as linear combination of atom orbitals (LCAO), and is typically 2.8 eV in graphene [2]. Because graphene consists of only carbon atoms, by symmetry the on-site energy of

an A atom is the same of a B atom. Thus, we can drop the on-site energy term and write the tight-binding Hamiltonian H as

$$\begin{aligned} H = t \sum_{\vec{R}_j} \sum_{i=1}^{3} & \left| \phi^A(\vec{r} - \vec{R}_j + \vec{\delta}_i) \right\rangle \left\langle \phi^B(\vec{r} - \vec{R}_j) \right| \\ & + \left| \phi^B(\vec{r} - \vec{R}_j + \vec{\delta} - \vec{\delta}_i) \right\rangle \left\langle \phi^A(\vec{r} - \vec{R}_j + \vec{\delta}) \right| \end{aligned} \tag{1.9}$$

where t is the hopping energy, and the terms consider the nearest hopping terms from both A and B atoms. The action of the Hamiltonian on the graphene Bloch wavefunction is

$$\begin{aligned} H \left| \psi_k(\vec{r}) \right\rangle &= H \left(a_{\vec{k}} \sum_{\vec{R}_j} e^{i\vec{k}.\vec{R}_j} \left| \phi^A(\vec{r} + \vec{\delta} - \vec{R}_j) \right\rangle + b_{\vec{k}} \sum_{\vec{R}_j} e^{i\vec{k}.\vec{R}_j} \left| \phi^B(\vec{r} - \vec{R}_j) \right\rangle \right) \\ &= a_{\vec{k}} t \sum_{\vec{R}_j} \sum_{i=1}^{3} e^{i\vec{k}.\vec{R}_j} \left| \phi^B(\vec{r} - \vec{R}_j + \vec{\delta} - \vec{\delta}_i) \right\rangle + b_{\vec{k}} t \sum_{\vec{R}_j} \sum_{i=1}^{3} e^{i\vec{k}.\vec{R}_j} \left| \phi^A(\vec{r} - \vec{R}_j + \vec{\delta}_i) \right\rangle \\ &= a_{\vec{k}} t e^{i\vec{k}.\vec{\delta}} \left(\sum_{i=1}^{3} e^{-i\vec{k}.\vec{\delta}_i} \right) \sum_{\vec{R}_j + \vec{\delta}_i - \vec{\delta}} e^{i\vec{k}.(\vec{R}_j + \vec{\delta}_i - \vec{\delta})} \left| \phi^B(\vec{r} - (\vec{R}_j + \vec{\delta}_i - \vec{\delta}) \right\rangle \\ &+ b_{\vec{k}} t e^{-i\vec{k}.\vec{\delta}} \left(\sum_{i=1}^{3} e^{i\vec{k}.\vec{\delta}_i} \right) \sum_{\vec{R}_j - \vec{\delta}_i} e^{i\vec{k}.(\vec{R}_j + \vec{\delta} - \vec{\delta}_i)} \left| \phi^A(\vec{r} + \vec{\delta} - (\vec{R}_j + \vec{\delta} - \vec{\delta}_i)) \right\rangle \\ &= a_{\vec{k}} t \gamma^* \left| \psi_k^B(\vec{r}) \right\rangle + b_{\vec{k}} t \gamma \left| \psi_k^A(\vec{r}) \right\rangle \end{aligned} \tag{1.10}$$

where

$$\gamma = e^{-i\vec{k}.\vec{\delta}} \left(\sum_{i=1}^{3} e^{i\vec{k}.\vec{\delta}_i} \right) = 1 + e^{i\left(\frac{3ak_x}{2} + \frac{\sqrt{3}ak_y}{2}\right)} + e^{i\left(\frac{3ak_x}{2} - \frac{\sqrt{3}ak_y}{2}\right)} \tag{1.11}$$

If we use $\{\left|\psi_k^A(\vec{r})\right\rangle, \left|\psi_k^B(\vec{r})\right\rangle\}$ as our ordered basis, the Hamiltonian H written out in matrix form is

$$H = t \begin{bmatrix} 0 & \gamma \\ \gamma^* & 0 \end{bmatrix} \tag{1.12}$$

We obtain graphene's band dispersion by solving for the eigenenergies $E_\pm$ of the

Hamiltonian H:

$$\begin{aligned} E_{\pm} &= \pm t|\gamma| \\ &= \pm t\sqrt{3 + 2\cos[(\vec{\delta}_1 - \vec{\delta}_2).\vec{k}] + 2\cos[(\vec{\delta}_1 - \vec{\delta}_3).\vec{k}]} \\ &= \pm t\sqrt{3 + 2\cos\left(\sqrt{3}k_y a\right) + 4\cos\left(\frac{\sqrt{3}k_y a}{2}\right)\cos\left(\frac{3k_x a}{2}\right)} \end{aligned} \tag{1.13}$$

A simple algebraic exercise gives two zero energy solutions to dispersion equation (), and these points in momentum space are known as Dirac points:

$$\vec{K} = \left(\frac{2\pi}{3a}, \frac{2\pi}{3\sqrt{3}a}\right), \vec{K}' = \left(\frac{2\pi}{3a}, -\frac{2\pi}{3\sqrt{3}a}\right) \tag{1.14}$$

If we expand the dispersion relation around point $\vec{K}$, to first order in $\vec{p} = \hbar(\vec{k} - \vec{K})$, we obtain a linear energy dispersion around the Dirac points:

$$E_{\pm}(\vec{p}) = \pm v_F|\vec{p}| \tag{1.15}$$

where $v_F = \frac{3ta}{2\hbar} \approx 10^6$ m/s is the Fermi velocity. An expansion around the other Dirac point $\vec{K}'$ yields the same energy relation. For a typical number density of $n = 10^{-12}\text{cm}^{-2}$, we obtain a Fermi wavelength $k_F = \sqrt{\pi n}$ on the order of 10^8m^{-1}, with a corresponding Fermi energy on the order of 100 meV [2].

The existence of two equivalent energy spectra at the two Dirac points gives rise to a degeneracy known as valley degeneracy. Coupled with the electron's spin degeneracy of two, the total degeneracy of the system g is 4 [2]. A graphical plot of the dispersion relation is shown in Fig. 1-3:

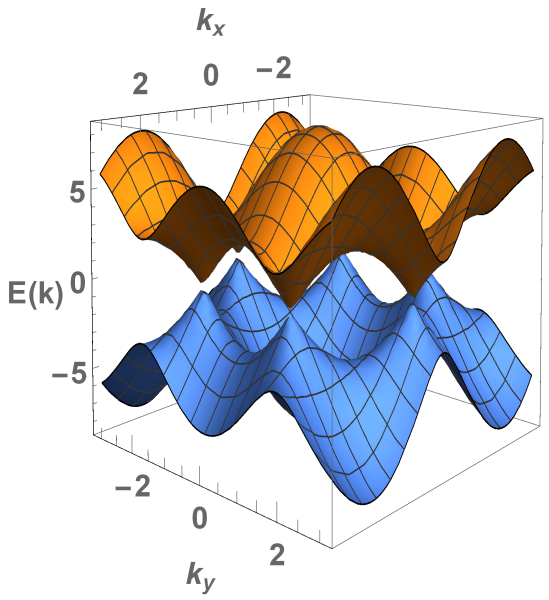

Figure 1-3: Graphical plot of graphene's band dispersion. The dispersion is linear around the Dirac points.

1.2.3 Integer Quantum Hall Effect in Graphene

One of the most striking features of the quantum Hall effect is the observation of quantized conductances in units of $e^2/h = 3.87 \times 10^{-5}$S ($e$ is the elementary charge. h is Planck's constant), a phenomenon which was first observed in silicon-based systems in 1980 [3]. One of the most remarkable facts is that the integer quantum Hall effect is observed in a wide range of samples regardless of the details of geometry and sample disorder, with quantized values accurate to one part in a billion, making it a possible metrology standard in the definition of the kilogram [16].

The integer quantum Hall effect in a two-dimensional system can be understood via the formation of Landau levels in the presence of a sufficiently strong magnetic field, where there are large energy gaps between two Landau levels where the density of states is essentially zero [17, 18]. When the Fermi energy is in the middle of a Landau level, the density of states is not zero and the bulk allows electrical conduction through the system. However, a conundrum arises when the Fermi energy is in an energy gap between two Landau levels: can the system still carry a current when the

bulk becomes insulating?

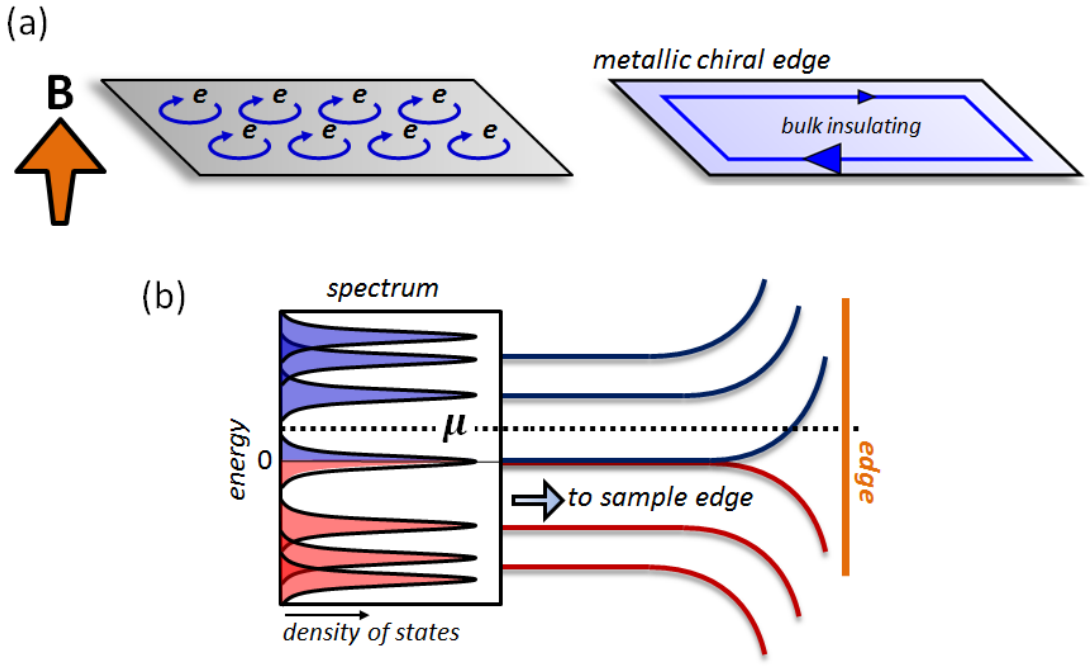

Figure 1-4: (a) Charge carriers undergo cyclotronic motion in the presence of a magnetic field. Skipping orbits along the edge of a sample creates metallic chiral edge states each with a ballistic conductance of e^2/h. (b) The "bathtub" model of the quantum Hall effect. Energy bands disperse upwards (downwards) for electron-like (hole-like) carriers near the edge of a sample. The Hall conductance is the number of edge channel crossings at the sameple edge at a chemical potential μ.

One possible answer to the above question is for the edges of the system to carry the current. From a semi-classical picture, we can qualitatively understand how this occurs: charge carriers in a magnetic field undergoes cyclotron motion in closed orbits in the bulk, thus unable to take part in electrical conduction. However at the edges, the confinement potential does not allow charge carriers to undergo complete cyclotron motion; a charge carrier hitting the edge would be specularly reflected, and creates a resultant edge channel which "hops" along the edges in a series of incomplete cyclotron orbits (panel (a) of Fig.1-4). Additionally, there is a defined direction of propagation, or chirality, associated with these edge channels: the direction in which

the charge carrier propagates is dependent on its charge and magnetic field direction as determined by the Lorentz force law, and more importantly the chirality will be different on opposite sides of the sample. The chirality of the edge states result in suppressed backscattering and dissipation-less transport, and each edge state results in a ballistic conduction channel with e^2/h conductance, which is one of the hallmark observations of the quantum Hall effect [19].

The quantum Hall effect can also be understood via the energy dispersion relations in the presence of a confinement potential: the "bathtub" model. In panel (b) of Fig.1-4, we see that the energy dispersion of charge carriers are flat in the bulk of the sample, which is expected for the quantization of kinetic energy for Landau levels. However, towards the sample of the edges, the energy bands are forced to disperse up or down (for electron-like and hole-like carriers respectively) to ensure that the charge carriers are bounded within the sample. As we adjust the Fermi energy of the system, the number of band crossings at the edges gives the corresponding number of ballistic edge channels [19].

In a classical two dimensional gas, the Landau level problem is given by [18]

$$\frac{(\vec{p} - q\vec{A})^2}{2m}\psi = E\psi \tag{1.16}$$

where $\nabla \times \vec{A} = \vec{B}$ is the applied magnetic field. The problem can be re-cast into a simple harmonic oscillator system [18] with the well-known energy spectrum:

$$E_{n,\text{classical}} = \left(n + \frac{1}{2}\right)\hbar\omega_c, n \in \mathbb{Z}^+ \tag{1.17}$$

where $\omega_c = \frac{qB}{m}$ is the cyclotron frequency of a charge carrier of mass m and charge q in a magnetic field B. However, because of graphene's linear energy dispersion around the Dirac point, the lack of an effective mass alters the qualitative nature of the Landau levels. One possible way to solve for the Landau levels in graphene is to use the zero mass limiting case of the two-dimensional Dirac equation, whose Hamiltonian is given by

$$H = \begin{bmatrix} mv_F^2 & v_F\ \vec{p}.\vec{\sigma} \\ v_F\ \vec{p}.\vec{\sigma} & -mv_F^2 \end{bmatrix} \tag{1.18}$$

where $\vec{p}$ is the momentum of the charge carrier, and $\vec{\sigma}$ is a vector whose components are the Pauli matrices $\sigma_x = \begin{bmatrix} 0 & 1 \\ 1 & 0 \end{bmatrix}$ and $\sigma_y = \begin{bmatrix} 0 & -i \\ i & 0 \end{bmatrix}$ respectively. In the presence of a magnetic field, we replace the kinetic momentum $\vec{p}$ by the canonical momentum $\vec{p} + q\vec{A}$, to obtain

$$H = \begin{bmatrix} mv_F^2 & v_F(\vec{p} - q\vec{A}).\vec{\sigma} \\ v_F(\vec{p} - q\vec{A}).\vec{\sigma} & -mv_F^2 \end{bmatrix} \tag{1.19}$$

For a spinor $\begin{bmatrix} \chi_1 \\ \chi_2 \end{bmatrix}$ that is an eigenstate of the Dirac Hamiltonian, and using the well-known identities $(\vec{a}.\vec{\sigma})(\vec{b}.\vec{\sigma}) = \vec{a}.\vec{b} + i\left(\vec{a} \times \vec{b}\right).\vec{\sigma}$ and $(\vec{p} - q\vec{A}) \times (\vec{p} - q\vec{A}) = iq\vec{B}$, we arrive at the following equations for the spinor components:

$$\begin{aligned} \left(\vec{p} + q\vec{A}\right)^2 \chi_1 &= \left(\frac{E^2}{v_F^2} - m^2 v_F^2 - qB\right) \chi_1 \\ \left(\vec{p} - q\vec{A}\right)^2 \chi_2 &= \left(\frac{E^2}{v_F^2} - m^2 v_F^2 + qB\right) \chi_2 \end{aligned} \tag{1.20}$$

These equations are reminiscent of the classical two-dimensional gas Landau level problem, where we can identify a new spectral parameter $\zeta = \frac{E^2}{v_F^2} - m^2 v_F^2 \mp qB$ with the energy solutions given in equation [1.14]. Taking into account the different possible signs of the charges, we obtain the following energy spectrum for both electron-like and hole-like carriers:

$$E_n = \mathrm{sgn}(N)\sqrt{m^2 v_F^4 + 2|qB|\hbar v_F^2(|N|)}, N \in \mathbb{Z} \tag{1.21}$$

In the limit of zero effective mass, the Landau level energies in graphene are given by:

$$E_N = \mathrm{sgn}(N) v_F \sqrt{2eB\hbar|N|}, N \in \mathbb{Z} \tag{1.22}$$

Each Landau level has a degeneracy n_{LL} given by

$$n_{LL} = 4\frac{B}{\Phi_0} \tag{1.23}$$

where $\Phi_0 = \frac{h}{e}$ is the magnetic flux quantum, and the factor of 4 comes from the valley and spin degeneracies in graphene. Coupled with the number density control via the capacitative field effect, we can control the location of the Fermi energy in relation to the Landau level energies at any magnetic field. As mentioned previously, the quantized Hall conductances are observed when the bulk becomes insulating i.e. the Fermi energy lies in between two Landau levels. In this case, the number of edge states is given by the number of filled Landau levels, also known as the filling factor ν defined to be $\nu = \frac{n}{n_{LL}}$ for a given number density n in the system. In the case of graphene, the measured quantum Hall filling factors would be [20]

$$\nu = 4(N + \frac{1}{2}), N \in \mathbb{Z} = \pm 2, \pm 6, \pm 10, ... \tag{1.24}$$

The factor of half in the quantum Hall sequence of graphene arises from the massless Dirac nature of the carriers [20], where the zero effective mass results in the co-existence of both electron-like and hole-like carriers in the zeroth Landau level, a feature which is absent in both classical gas and massive Dirac two-dimensional gas systems. Additionally, while the band gaps between Landau levels in a classical system is constant, the square root dependence on the Landau level index in graphene means that the band gaps between Landau levels decreases, with the maximum band gaps between the zeroth and first Landau levels. This has a significant implication on the quality of the quantized Hall conductance measured in graphene; sample disorder spreads the localized density of states in a Lorentzian fashion [21], and a sample disorder which is too high will mix neighboring Landau levels which destroys the conductance quantization. As an order of estimate, the largest Landau level gap in

graphene at a magnetic field of 10 T is around 100 meV.

The value of 100 meV is the typical order of magnitude of the disorder energy of a silicon substrate [15], which illustrates the need for fabrication techniques that can further screen out the role of disorder if we are to study electronic properties at smaller energy scales. The use of hBN, which is also a two-dimensional material, and self-cleaning in the assembly of van der Waals heterostructures [12] are indispensable techniques that were used to reduce disorder in our samples, and these methods will be later discussed later in the thesis.

Chapter 2

Twist Angle: A Degree of Freedom in van der Waals Heterostructures

In this chapter, the role of the twist angle in van der Waals heterostructures will be examined, with a focus on twisted bilayer graphene, a system where two sheets of graphene are stacked on top of each other. I will first elucidate how the twist angle controls the momentum coupling between the two graphene layers, and explore how we can exploit this control to form different type of electronic systems in the large and small twist angle limit.

In particular, for large twist angles, I will illustrate how we can exploit the decoupling between the two graphene layers at low energies to independently control the edge modes in each layer to form a quantum spin Hall system. In the small twist angle case, the role of a new emergent momentum scale controlled by the moiré potential will be examined, and expectations of its effect on twisted bilayer graphene systems will be inferred from previous studies on graphene/hBN van der Waals heterostructures. My experimental work in these two regimes will be covered later in Chapter 3 and Chapter 4 respectively.

2.1 Twist Angles & Momentum Coupling

As a starting point to theoretically predict the electronic properties of twisted bilayer graphene, we consider how the twist angle between the two graphene sheets controls the interlayer coupling. There are two main approaches outlined in literature: the low-energy continuum model [22] and the lattice approach [23, 24]. In this section, I shall outline the approach used by Shallcross et al. [24], with the lattice model geometrically arguing the emergence of a natural momentum coulping scale without resorting to any approximations. The twist angle is a continuous variable; as such, we do not expect twisted bilayer graphene to be a strictly periodic, or commensurate, structure. However, we can derive the condition required on the twist angle such that the system is commensurate, which would then allow us to use all the machinery of Bloch's theorem to create a first-order prediction of the electronic properties of twisted bilayer graphene.

Let $\vec{a}_1$ and $\vec{a}_2$ be the Bravais lattice vectors of a single unrotated graphene layer. Then the position vector of any lattice point on this graphene layer can be written as $m_1\vec{a}_1 + m_2\vec{a}_2$ where m_1 and m_2 are integers. Now suppose we stack another graphene layer on top with some relative twist angle θ, and we observe some feature above a specific lattice point on the unrotated layer (AB stacking, AA stacking, etc.). We now seek the exact same feature somewhere else in the twisted bilayer graphene, whose position vector we can write as $n_1\vec{a}_1 + n_2\vec{a}_2$ where n_1 and n_2 are integers. If the structure is *commensurate*, the two vectors must be related via a rotation i.e.

$$m_1\vec{a}_1 + m_2\vec{a}_2 = R(n_1\vec{a}_1 + n_2\vec{a}_2) \tag{2.1}$$

where R is a rotation matrix, and can be written in Cartesian coordinates as

$$R = \begin{bmatrix} \cos(\theta) & -\sin(\theta) \\ \sin(\theta) & \cos(\theta) \end{bmatrix} \tag{2.2}$$

However, it would be more illuminating to re-write the rotation matrix R using the graphene Bravais lattice vectors $\vec{a}_1, \vec{a}_2$ as our basis. In this basis,

$$R = \begin{bmatrix} \cos(\theta) - \frac{1}{\sqrt{3}}\sin(\theta)) & -\frac{2}{\sqrt{3}}\sin(\theta) \\ \frac{2}{\sqrt{3}}\sin(\theta) & \cos(\theta) + \frac{1}{\sqrt{3}}\sin\theta \end{bmatrix} \tag{2.3}$$

Since m_1, m_2, n_1, n_2 are all integers, enforcing the commensurability condition requires all the entries of R in the Bravais lattice to be *rational*. This leads to a set of twist angles for which the twisted bilayer graphene is a commensurable structure:

$$\cos(\theta) = \frac{3q^2 - p^2}{3q^2 + p^2} \quad p, q \in \mathbb{Z} \tag{2.4}$$

For this class of commensurate angles, we can obtain the Bravais lattice vectors for the twisted bilayer graphene in terms of the monolayer graphene Bravais lattice vectors $\vec{a}_1, \vec{a}_2$ and p, q (which determines the twist angle). There are two cases to consider, which is determined by $\delta = \frac{3}{\gcd(p,3)}$.

For $\delta = 1$,

$$\begin{aligned} \vec{t}_1 &= \frac{1}{\gamma}\left[(p+3q)\vec{a}_1 - 2p\vec{a}_2\right] \\ \vec{t}_2 &= \frac{1}{\gamma}\left[2p\vec{a}_1 + (3q-p)\vec{a}_2\right] \end{aligned} \tag{2.5}$$

For $\delta = 3$,

$$\begin{aligned} \vec{t}_1 &= \frac{1}{\gamma}\left[-(p+q)\vec{a}_1 + 2q\vec{a}_2\right] \\ \vec{t}_2 &= \frac{1}{\gamma}\left[2q\vec{a}_1 + (q-p)\vec{a}_2\right] \end{aligned} \tag{2.6}$$

where $\gamma = \gcd(3q+p, 3q-p)$. The corresponding reciprocal vectors are therefore given by:

For $\delta = 1$,

$$\begin{aligned} \vec{g}_1 &= \frac{\gamma}{3(3q^2+p^2)}\left[(p+3q)\vec{b}_1 + 2p\vec{b}_2\right] \\ \vec{g}_2 &= \frac{\gamma}{3(3q^2+p^2)}\left[-2p\vec{b}_1 + (3q-p)\vec{b}_2\right] \end{aligned} \tag{2.7}$$

For $\delta = 3$,

$$\begin{aligned}\vec{g}_1 &= \frac{\gamma}{3(3q^2+p^2)}\left[(q-p)\vec{b}_1 + 2q\vec{b}_2\right] \\ \vec{g}_2 &= \frac{\gamma}{3(3q^2+p^2)}\left[-2q\vec{b}_1 - (p+q)\vec{b}_2\right]\end{aligned} \tag{2.8}$$

where $\vec{b}_1, \vec{b}_2$ are the reciprocal vectors of the unrotated graphene layer.

Interlayer interactions in twisted bilayer graphene can be described by matrix elements connecting momentum eigenstates of the unrotated and rotated graphene layers. Denoting these eigenstates in each layer as $\left(\left|\phi^{(1)}_{i_1,\vec{k}_1}\right\rangle, \left|\phi^{(2)}_{i_2,\vec{k}_2}\right\rangle\right)$ respectively, we can write a typical matrix element of the interlayer Hamiltonian as $\left\langle \phi^{(1)}_{i_1,\vec{k}_1}\right| V^{(1)} \left|\phi^{(2)}_{i_2,\vec{k}_2}\right\rangle$ where $V^{(1)}$ is the single layer graphene potential. Since the potential is periodic, we can apply Bloch's theorem to write both the layer potential and wavefunctions using the reciprocal vectors $\vec{G}_1, R\vec{G}_2$ in each layer respectively (the R labels rotation in the second layer):

$$\begin{aligned}V^{(1)} &= \sum_{\vec{G}'_1} V^{(1)}_{\vec{G}'_1} e^{i\vec{G}'_1.\vec{r}} \\ \phi^{(1)}_{i_1,\vec{k}_1} &= \sum_{\vec{G}'_1} c^{(1)}_{i_1,\vec{k}_1+\vec{G}''_1} e^{i\left(\vec{k}_1+\vec{G}''_1\right).\vec{r}} \\ \phi^{(2)}_{i_2,\vec{k}_2} &= \sum_{R\vec{G}_2} c^{(2)}_{i_2,\vec{k}_2+R\vec{G}_2} e^{i\left(\vec{k}_2+R\vec{G}_2\right).\vec{r}}\end{aligned} \tag{2.9}$$

Thus, evaluating the matrix element involves two main parts: an electronic integral which depends on the details of the orbitals, and a geometric integral which serves as a momentum selection rule dictating the allowed momentum shifts when an electron hops between the layers. Specifically,

$$\begin{aligned}\left\langle \phi^{(1)}_{i_1,\vec{k}_1}\right| V^{(1)} \left|\phi^{(2)}_{i_2,\vec{k}_2}\right\rangle = \sum_{\vec{G}'_1,\vec{G}''_1,R\vec{G}_2} \int c^{(1)*}_{i_1,\vec{k}_1+\vec{G}''_1} V^{(1)}_{\vec{G}'_1} c^{(2)}_{i_2,\vec{k}_2+R\vec{G}_2} \times \\ \int d^3r e^{i}[\vec{G}'_1 - (\vec{k}_1+\vec{G}''_1) + \vec{k}_2 + R\vec{G}_2]\end{aligned} \tag{2.10}$$

The top line of equation (2.10) corresponds to the electronic integral, while the bottom line corresponds to the momentum selection rule, since the integral evaluates to a Dirac delta function. Recognizing that $\vec{G}_1' - \vec{G}_1''$ is just another reciprocal vector $\vec{G}_1$ in the unrotated layer, we can express the momentum selection rule as:

$$\vec{G}_1 - R\vec{G}_2 = \vec{k}_2 - \vec{k}_1 \equiv \Delta\vec{k} \tag{2.11}$$

Note that equation (2.11) is essentially the same as the real space commensurability problem discussed earlier in this section, with an additional term $\Delta\vec{k}$. The goal of the problem is therefore the same: can we find momentum shifts $\Delta\vec{k}$ such that electrons can hop between layers obeying the momentum selection rule? While the solutions are complicated to derive, the results are easily quoted and verifiable [24]. Expressing $\Delta\vec{k}$ as a linear combination of the reciprocal vectors given in equation (2.7) and (2.8) i.e. $\Delta\vec{k} = l_1\vec{g}_1 + l_2\vec{g}_2,\ l_1, l_2 \in \mathbb{Z}$, we have

$$\Delta\vec{k} = n_1\vec{g}_1^{(c)} + n_2\vec{g}_2^{(c)}, \Delta\vec{G} = n_1\vec{b}_1 + n_2\vec{b}_2, n_1, n_2 \in \mathbb{Z} \tag{2.12}$$

where for $\delta = 1$,

$$\begin{aligned} \vec{g}_1^{(c)} &= -\frac{2p}{\gamma}(\vec{g}_1 + 2\vec{g}_2) \\ \vec{g}_2^{(c)} &= \frac{2p}{\gamma}(2\vec{g}_1 + \vec{g}_2) \end{aligned} \tag{2.13}$$

and for $\delta = 3$,

$$\begin{aligned} \vec{g}_1^{(c)} &= -\frac{2p}{\gamma}\vec{g}_1 \\ \vec{g}_2^{(c)} &= -\frac{2p}{\gamma}\vec{g}_2 \end{aligned} \tag{2.14}$$

Because of the exponential suppression of the amplitudes of the Fourier components given by the electronic integral in equation (2.10) [24], matrix elements of the interlayer Hamiltonian which obey the selection rule has a significant amplitude only when the $\Delta\vec{G}$ is small, i.e. the integers n_1, n_2 in the solutions of equation (2.12) need

to be small as well. Thus, this implies that the momentum scale at which significant interactions occur are given by the vectors $\vec{g}_1$ and $\vec{g}_2$.

By equation (2.4), we can re-write the coupling vectors $\vec{g}_1$ and $\vec{g}_2$ in terms of the twist angle. In particular, a simple algebraic exercise shows that in all cases, the magnitude of the coupling vectors are given by

$$|\vec{g}_{1,2}^{(c)}| = \frac{4}{\sqrt{3}} \sin \frac{\theta}{2} \tag{2.15}$$

The main implication of equation (2.15) is that only the twist angle determines the interlayer interactions: all details of the lattice in twisted bilayer graphene has "disappeared" in the final result.By controlling the twist angle, we can thus control the strength of interactions between the two layers: when the twist angle is large, the coupling momentum is correspondingly large, and the two layers are decoupled at low energy scales. Conversely, when the twist angle is small, interactions are strong at low energy scales.

2.2 Large Twist Angle Physics

From the previous section, the role of the twist angle is to control the magnitude of the coupling momentum between the two layers. Heuristically, one can envision this as the momentum displacement between the Dirac points of the two layers. In the low energy continuum approximation [22], the Dirac points are separated by a momentum vector $\Delta\vec{K} = 2\vec{K}\sin\left(\frac{\theta}{2}\right)$. In the case where the twist angle θ is large, the bands of both layers only hybridize at high energies comparable to the M point of graphene [2, 25]. Thus at low energies, we can treat the two graphene layers in twisted bilayer graphene to be decoupled in the bulk.

Although the physics in the large twist angle case is relatively simple to understand, we can exploit the decoupling in the bulk to engineer novel edge state systems using the monolayer quantum Hall effect. One of the main objectives in my research is to create a quantum spin Hall type system in twisted bilayer graphene by independently controlling the edge modes in each layer.

2.2.1 Creating a Quantum Spin Hall State

The quantum spin Hall state is an important two-dimensional topological state of matter: when interfaced with superconductors and magnetic materials, it is predicted to form topological qubits which have applications in quantum computing [26–28]. These states have been reported in various material systems, such as cadmium telluride/mercury telluride quantum wells [29], as well as two-dimensional materials like tungsten telluride [30]. In simple terms, the quantum spin Hall state can be regarded as two copies of the quantum hall effect, consisting of two counter-propagating edge modes with opposite spin polarizations, with a quantized conductance of $\frac{2e^2}{h}$. Since the two edge modes propagate in opposite directions, these edge modes could possibly hybridize and gap each other out, leading to complete backscattering that would destroy the quantized conductance. However, in the aforementioned material systems, a combination of time-reversal and crystal symmetry protect these edge modes [31–33].

For graphene, it was initially believed that it could host a quantum spin Hall state

at charge neutrality [34] i.e. at $\nu = 0$ in a strong magnetic field: if the Zeeman effect is dominant, the exchange interactions would form a pair spin polarized edge modes which cross at charge neutrality, resulting in a quantized conductance of $\frac{2e^2}{h}$ [35]. However, besides the role of spin, valleys are also an important factor in determining the electronic properties of graphene. In particular, lattice anisotropies can result in couplings between the valleys that can favor other electronic ground states, such as a canted anti-ferromagnet, Kekulé distortions and charge density waves [35]. The combination of spin and valleys create a rich $SU(4)$ space for which different electronic ground states can exist, depending on the details of lattice effects, electron-electron, and electron-phonon interactions [35].

Although early experimental studies measured a longitudinal resistance which is not zero for the $\nu = 0$ state [20, 36], suggesting that with further reduction of sample disorder, a quantum spin Hall state could be observed at charge neutrality. However, subsequent devices made with improved fabrication techniques (such as suspended graphene and graphene encapsulated with hBN) showed an insulating state at charge neutrality, at fields as low as in the 1T range [37–39]. The observation of an insulating phase at relatively low magnetic fields ruled out the quantum spin Hall state as the electronic ground state in graphene at charge neutrality: the role of lattice coupling between the valleys must be considered in determining the electronic ground state. Additionally, it was also shown that the $\nu = 0$ state is not spin polarized, which further limits the possible ground states at charge neutrality [39].

One important experimental study on the ground state of the $\nu = 0$ system was performed by Young et. al [40]. The key idea was to differentiate the coupling of the perpendicular and total magnetic fields to the valleys and spins in graphene: the spins are sensitive to the Zeeman field which depends on the total magnetic field, whereas lattice anisotropies are only sensitive to the perpendicular field due to the two-dimensionality of the material [35]. The observation of an insulating state suggested that symmetry breaking due to lattice anisotropies are more dominant than the Zeeman effect. However, it would be possible to increase the role of the Zeeman effect if the total magnetic field is increased while keeping the perpendicular

field constant. This could be achieved by tilting the sample in the presence of a very strong magnetic field in the range of 40T. The authors of the paper demonstrated that by increasing the total magnetic field while keeping the perpendicular field constant, they are able to tune the $\nu = 0$ state continuously from an insulating state to a state with a conductance close to $\frac{2e^2}{h}$, the expected conductance of a quantum spin Hall system.

The nature of the suspected quantum spin Hall state was further determined through non-local measurements. While the edge modes within the material system is protected against backscattering due to spin protection, these edge modes are able to equilibrate within metallic contacts due to spin mixing, resulting in interrupted edge states between any pair of metallic contacts with a resistance of $\frac{h}{e^2}$ [40]. By varying the geometry of the contacts and the combination of source-drain contacts, they demonstrated that the edge modes that emerge in the $\nu = 0$ in a high in-plane magnetic field is consistent with a quantum spin Hall edge mode transport [40]. This method of non-local measurements would also be used and described further in Chapter 3.

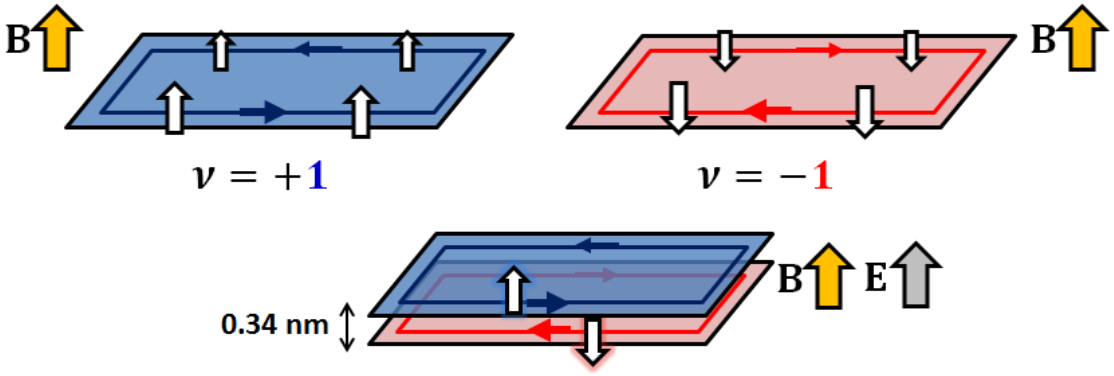

Figure 2-1: The $\nu = +1$ and $\nu = -1$ states in graphene have opposite chiralities and spin polarizations. Stacking the two edge states on top of each other, which is possible in large angle twsited bilayer graphene, can possibly host a quantum spin Hall system.

While a quantum spin Hall state can be achieved in monolayer graphene, it requires the use of an extremely high magnetic field, which limits its applications in

forming topological qubits since superconductors is also an essential ingredient. We want to find another platform for where we can achieve a quantum spin Hall state at much lower magnetic fields, and large angle twisted bilayer graphene is a highly possible candidate. As discussed in Chapter 1, the $\nu = 1$ and $\nu = -1$ quantum Hall edge states are spin polarized with opposite chiralities. If we can independently put each of these edge modes in the two separate layers, we would have essentially created a quantum spin Hall state (Fig. 2-1). The decoupling between the two layers would be key for the edge modes to be controlled independently, thus necessitating a large twist angle between the two layers. The experimental work performed on this system would be covered in Chapter 3.

2.3 Small Twist Angle Physics

At small twist angles, the scale of the momentum coupling vector becomes comparable to the typical Fermi energy in our measured systems. As such, interlayer interactions becomes significant and the two layers are strongly coupled via interlayer hybridizations. A new long-range periodic potential, known as the moiré potential, also emerges which also affects the transport properties of twisted bilayer graphene. This section gives a brief background behind the formalism of the moiré effect, and a brief run through of various experimental studies which have examined this phenomenon in various two-dimensional materials.

One of the most important emergent phenomenon at small twist angles is the moiré effect.

2.3.1 Moiré Potentials & Superlattices

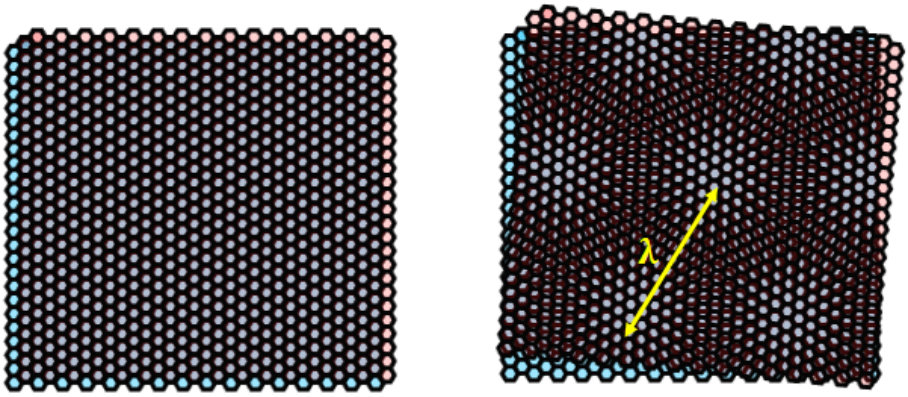

Figure 2-2: A small twist between two periodic layers creates a long range pattern known as the moiré effect, with a new moiré wavelength λ introduced into the system.

The moiré phenomenon is a geometric effect that arises from two periodic layers, creating a pattern with a new length scale (known as the moiré wavelength) which is not present in the individual layers [41]. At small twist angles, the emergent moiré pattern is a long range effect, with a moiré wavelength that is much larger than the underlying lattice constants as seen in Fig. 2-2.

One of the more illuminating ways to envision the moiré effect is to analyze it in the frequency domain [41]. Any periodic function has a Fourier representation; in two dimensions, one can write a periodic function $r(x, y)$ as

$$r(x, y) = \sum_{n \in \mathbb{Z}} a_n \cos[2\pi n f(x \cos\theta + y \sin\theta)] \tag{2.16}$$

where f is the fundamental frequency of the periodic system and θ is the phase shift of the system. By assigning the x and y coefficients as a single frequency vector $\vec{f} = \begin{bmatrix} f\cos\theta \\ f\sin\theta \end{bmatrix}$, we can interpret the stacking of two periodic layers as the vectorial sum of the two constituent frequency vectors. Note for a periodic profile that is not strictly sinusoidal, there is theoretically an infinite combination of resultant moiré frequency vectors one can construct for different choices of n for each layer. However, in small angle twisted bilayer graphene, only moiré vectors that correspond to low energies matters due to the small magnitude of the coupling momentum i.e. we want a frequency vector which is small as well. One can construct such a frequency vector from two layers by considering the *difference* between the constituent frequency vectors i.e.

$$\begin{aligned} \vec{f}_m &= \vec{f}_1 - \vec{f}_2 \\ f_{m,x} &= f_1 \cos\theta_1 - f_2 \cos\theta \\ f_{m,y} &= f_1 \sin\theta_1 - f_2 \sin\theta \end{aligned} \tag{2.17}$$

where $\vec{f}_m$ is the frequency of the moiré pattern due stacking of two periodic layers 1 and 2. The resultant moiré wavelength λ_m can then be determined using the following basic relations:

$$\begin{aligned} f_m \equiv |\vec{f}_m| &= \sqrt{f_{m,x}^2 + f_{m,y}^2} \\ \lambda_m &= \frac{c}{f_m} \text{ for some constant } c \end{aligned} \tag{2.18}$$

For the two layer scenario, a simple algebraic exercise shows that

$$\begin{aligned} f_m &= \sqrt{f_1^2 + f_2^2 - 2f_1 f_2 \cos(\theta_1 - \theta_2)} \\ \Rightarrow \lambda_m &= \frac{\lambda_1 \lambda_2}{\sqrt{\lambda_1^2 + \lambda_2^2 - 2\lambda_1 \lambda_2 \cos(\theta_1 - \theta_2)}} \end{aligned} \tag{2.19}$$

where λ_i is the wavelength in layer i, and we can identify the twist angle as $\theta = \theta_1 - \theta_2$.

The earliest studies of the moiré effect in two dimensional materials occurred in epitaxially grown graphite [42]. During the growth process, the top layer of the graphite can be displaced rotationally relative to the underlying layers, creating a discernible moiré pattern that can be examined by scanning tunneling spectroscopy [42, 43]. Additionally, by measuring the tunneling current at different tip energies, they are able to obtain the density of states as a function of energy [43, 44]. This information allowed the authors to deduce two main effects of the small twist angle: the twisted layers hybridize to lower the energy of the van Hove singularities, and renormalize the Fermi velocities to a lower value compared to monolayer graphene [44]. These observations were further confirmed by other experimental studies such as ARPES [45].

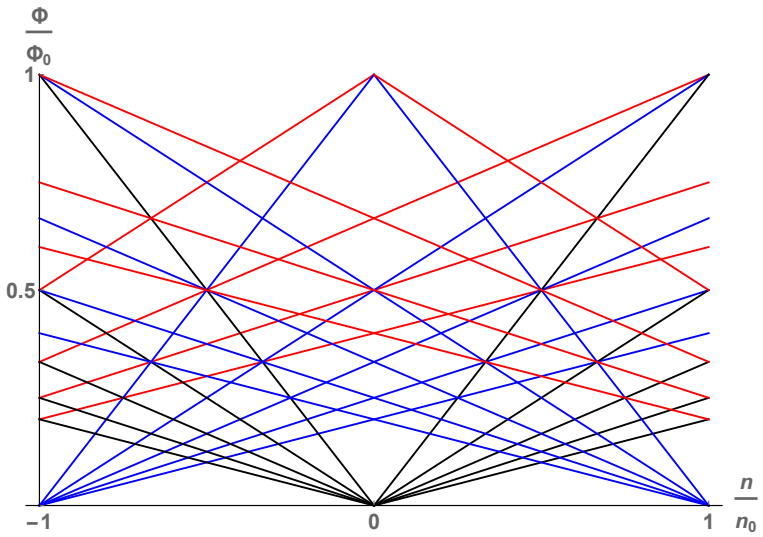

Figure 2-3: Plot of a Wannier ladder for $s = -2, -1, 0, 1, 2$ and $t = -10, -9, ..., 9, 10$. Black, blue and red lines correspond to $|s| = 0, 1, 2$ respectively.

With the advent of more advanced fabrication techniques which can greatly reduce the sample disorder in van der Waals heterostructures, transport studies in high quality samples revealed one of the most spectacular effects of the moiré effect: the Hofstadter butterfly. The Hofstadter butterfly arises from the competition of two length scales: the lattice wavelength (which could arise from a lattice constant or a moiré wavelength) and the magnetic length $l_B = \sqrt{\frac{\hbar}{eB}}$. When the two length scales become comparable, one unit cell of the periodic structure can hold one unit of magnetic flux quantum, resulting in a fractal splitting of the Landau levels in a recursive fashion [46]. Re-plotting the Hofstadter butterfly using the number density n and magnetic flux Φ gives an equivalent (and more convenient) representation of the Hofstadter butterfly known as a Wannier ladder shown in Fig. 2-3, where each of the straight lines have the equation

$$\frac{n}{n_0} = t\frac{\Phi}{\Phi_0} + s \tag{2.20}$$

where n_0 is the number density of a fully filled unit cell, s is a Block band filling index similar to the function of the Landau level labeling index, and t corresponds to the Hall conductivity of the particular state [47–49].

In graphene, due to the small lattice constant of 1.42 nm, a magnetic field of on the order of 10000 T is required for the Hofstadter butterfly to be observed, a field which is practically impossible to achieve with current technologies. However, one can exploit the moiré effect to create a unit cell with a much larger wavelength, and hence observe the Hofstadter butterfly at much lower magnetic fields. The first van der Waals system used to explore this effect was the graphene/hBN heterostructure [47–49]. hBN has a similar honeycomb lattice as graphene, with a slight lattice mismatch of 1.8% with the graphene lattice constant [50]. Based on equation (2.19), for a zero degree twist angle between the two layers, a maximum moiré wavelength of 14 nm can be achieved, requiring only 40T for to put one magnetic flux quantum in a unit cell, which is achievable in various high magnetic field lab facilities.

In the case of twisted bilayer graphene, since both layers are identical, the moiré

wavelength expression takes on a much simpler form, where

$$\lambda_{m,\mathrm{TBLG}} = \frac{a}{2\sin\frac{\theta}{2}} \tag{2.21}$$

This expression reveals an additional promise for studying moiré physics in twisted bilayer graphene: since the wavelength increases continuously as the twist angle becomes smaller, in theory we could build a system with extremely large moiré wavelengths which have been inaccessible in other small twist van der Waals heterostructures. In particular, the larger range of moiré wavelengths available in twisted bilayer graphene offers greater flexibility in studying the interplay of moiré physics and interlayer hybridization effects. Chapter 4 explores my experimental work in this regard, where we have observed exotic transport properties that is radically different from monolayer graphene.

THIS PAGE INTENTIONALLY LEFT BLANK

Chapter 3

Helical Edge State Conduction in Large Angle Twisted Bilayer Graphene

3.1 Introduction

This chapter of the thesis describes the experimental work and results on large angle twisted bilayer graphene, where we engineer a bilayer quantum spin Hall like state by independently controlling the edge states in each layer of graphene.

3.1.1 Experimental Objectives

As outlined in Chapter 2, the aim of the experiment is to realize a quantum spin Hall state in large angle twisted bilayer graphene, where we can exploit the decoupling between the two graphene layers to independently control the quantum Hall edge modes by tuning the total charge density and electric field applied across the system. The main questions that I aim to address are as follow:

1) What is the nature of the quantum Hall effect in large angle twisted bilayer graphene? In particular, do edge modes in the system exhibit any form of interaction, despite being decoupled in the bulk?

2) Is it possible to create a quantum spin Hall state in large angle twisted bilayer graphene?

3) Can large angle twisted bilayer graphene support fractional quantum Hall states?

3.2 Experimental Background

3.2.1 Broken Symmetry States in Graphene

As mentioned in the previous section, each Landau level in graphene has an overall four fold degeneracy due to both spin and valley degeneracies. While the integer quantum Hall effect can be understood via the Landau level single-particle picture, electron-electron interactions can create further symmetry breaking which gives rise to new correlated electronic states.

The first source of electron-electron interactions arises from exchange interactions. Exchange interactions arise from the exchange statistics of indistinguishable particles: electrons with the same spin tend to be further apart compared to electrons of opposite spins [17, 18]. In the presence of a magnetic field and Coulombic interactions, this gives rise to two competing effects: the magnetic field can create a ferromagnetic state by gapping out the Landau level into two spin polarized bands, thereby lowering the Coulombic energy in the system via this exchange interaction. However, due to the Pauli exclusion principle, electrons with the same spin must have different spatial wavefunctions, thereby increasing the Fermi level i.e. the kinetic energy in the system. For the ferromagnetic state to be favorable, a very flat band is required: the kinetic energy cost does not overwhelm the decrease in the Coulombic interactions between the electrons.

In the case of graphene, the pristine nature of the crystal results in very little disorder-widening of the Landau levels, and the weak spin-orbit coupling in graphene [51, 52] screens very little of the electron-electron interactions, and this is especially true in the zeroth Landau level where the number density is low. Thus, exchange inter-

actions are strong in graphene, and various interaction induced gaps are observed at half and quarter filling of the various Landau levels [39]. In particular, the $\nu = \pm 1$ states have been observed to be spin polarized states with opposite spin polarizations and chiralities, which is consistent with the exchange interaction model described previously [39]. The $nu = \pm 1$ states would become instrumental in creating a quantum spin Hall system.

3.2.2 Fractional Quantum Hall Effect in Graphene

Another important many-body state that can arise from electron interactions is the fractional quantum Hall effect. where Hall conductances are observed at *fractional* values of e^2/h. This effect was first discovered in gallium-arsenide systems, but requiring samples that are much more pristine measured at lower temperatures [4]. While the integer quantum Hall effect can be understood via a single particle picture, the fractional quantum Hall effect invokes a richer hierarchy of electron interactions, with some states having complex non-abelian statistics such as the even denominator $\nu = \frac{1}{2}, \frac{5}{2}$ states [53, 54]. For the purpose of this thesis, I shall give a brief background on the simpler fractional quantum Hall states with filling factors $\frac{p}{2p+1}$, $p \in \mathbb{Z}$, which are also known as the hierarchy states.

The hierarchy states in a classical two-dimensional gas can be understood via the composite fermion picture [55, 56], where an electron is paired with two magnetic vortices to create the composite fermion. Within this formalism, the hierarchy states can be thought of resulting from the *integer* quantum Hall states of these composite fermions, where the fractions at filling factors $\nu = \frac{1}{3}, \frac{2}{5}, \frac{3}{7}, ...$ correspond to the Landau level labeling index $1, 2, 3, ...$ respectively.

The first observed fractional quantum Hall effect came from studies on suspended graphene [37,38], where the removal of the substrate's disordered potential created a clean enough system for the $\nu = \frac{1}{3}$ state to be observed. Subsequent studies on hBN encapsulated graphene observed fractions at filling factors at all the thirds, except for $\nu = \frac{5}{3}$, which the authors attributed to a diminished energy gap due to the mixing of the spin and valley states by electron-electron interactions [57]. In this chapter, we

will show that the fractional quantum Hall effect can be supported in twisted bilayer graphene, with the difference in observations that differs from the aforementioned monolayer graphene studies.

3.2.3 Previous Transport Studies on Large Angle Twisted Bilayer Graphene

Transport studies on twisted bilayer graphene have historically been limited due to two main reasons: twisted bilayer graphene obtained via chemical vapor deposition (CVD) have too much disorder, while naturally exfoliated graphene bilayers are Bernal-stacked. Initial transport studies on twisted bilayer graphene relied either on CVD grown sources [58], or monolayer graphene that has been fortuitously folded over on itself [107]. For the transport studies on CVD grown twisted bilayer graphene, the observed quantum Hall plateaus seemed more consistent with a small twist angle case [58], whereas transport studies on the folded-over graphene observed two sets of Shubnikov-de Haas oscillations with two distinct periods, suggesting decoupled transport behavior [107]. However, for both these studies, only a single gate was used, which limits the understanding of the transport behavior in twisted bilayer graphene due to the lack of electric field control.

However, with the advent of fabrication techniques that allowed controlled stacking of van der Waals heterostructures, high quality dual-gated twisted bilayer graphene samples can be obtained. The first transport study on dual-gated twisted bilayer graphene was reported by Sanchez-Yamagishi et al [82]. In this study, the dual-gating allowed complete control of the total charge density and electric field applied, and the authors demonstrated Landau level crossings which is completely consistent with two decoupled graphene layers i.e. spin, valley, and (more importantly) *layer* are good quantum labels to describe the system. Another important observation from this study was the possible interactions between the edge states, in particular when one layer was doped to $\nu = +2$ and the other layer to $\nu = -2$. Quantum Hall states exhibit dissipation-less transport due to its chirality which prevents backscattering; if

these edge states do not interact, we expect a zero longitudinal resistance to be measured. However, the authors observed a highly insulating state, suggesting that these edge states hybridize to create a transport gap at the edge i.e. a strong backscattering path in the system.

3.3 Experimental Details

The experimental study typically follows a three-step process: 1) Fabricating the twisted bilayer graphene van der Waals heterostructure, 2) Making electrical contacts and metallic gates via lithographic methods, and 3) transport measurement in a low temperature cryostat equipped with a magnetic field. High quality samples of dual-gated twisted bilayer graphene encapsulated in hBN were fabricated via a dry transfer pickup method, where the details are outlined in Appendix A.

3.4 Helical Edge States and Fractional Quantum Hall Effect in a Graphene Electron-Hole Bilayer

The following section is a text reproduction from Sanchez-Yamagishi and Luo et. al [60].

Helical 1d electronic systems are a promising route towards realizing circuits of topological quantum states that exhibit non-abelian statistics [61–64]. Here, we demonstrate a versatile platform to realize 1d systems made by combining quantum Hall (QH) edge states of opposite chiralities in a graphene electron-hole bilayer at moderate magnetic fields. Using this approach, we engineer helical 1d edge conductors where the counterpropagating modes are localized in separate electron and hole layers by a tunable electric field. These helical conductors exhibit strong nonlocal transport signals and suppressed backscattering due to the opposite spin polarizations of the counterpropagating modes. Unlike other approaches used for realizing helical states [65–67], the graphene electron-

hole bilayer can be used to build new 1d systems incorporating fractional edge states [37, 38]. Indeed, we are able to tune the bilayer devices into a regime hosting fractional and integer edge states of opposite chiralities, paving the way towards 1d helical conductors with fractional quantum statistics [68–71].

A helical 1d conductor is an unusual electronic system where forward and backward moving electrons have opposite spin polarizations. Theoretically, helical states can be realized by combining QH edge states with opposite spin and opposite chiralities [61,64]. Most experimental efforts though have focused on materials with strong spin-orbit coupling at zero magnetic field [65–67]. However, a QH edge state approach offers greater flexibility in system design with less dependence on material parameters. Moreover, a QH platform could harness the unique statistics of fractional QH states. Recent proposals have predicted that such a system, in the form of a fractional quantum spin Hall state, for example, could host fractional generalizations of Majorana bound states [68–71]. To simultaneously realize QH states with opposite chiralities, it is necessary to have coexisting electron-like and hole-like bands. Electron-hole QH states are observed in semi-metals, but suffer from low hole-mobilities [72,73]. In this respect, graphene is attractive because it has high carrier mobilities and electron-hole symmetry. In fact, the graphene electron and hole bands can be inverted by the Zeeman effect to realize helical states [74, 75], but requires very large magnetic fields [40, 76]. A similar outcome could be realized more easily in a bilayer system, where electric fields can dope one layer into the electron band and the other into the hole band. At moderate magnetic fields, this electron-hole bilayer will develop QH edge states with opposite chiralities in each layer. Note that unlike edge states in a lateral quantum Hall p-n junction [77], the electron-hole bilayer boundary will host modes that are 1) counterpropagating, and 2) spaced apart by sub-nanometer distances. Here, we demonstrate such a graphene electron-hole bilayer, which we use to realize a helical 1-dimensional conductor made from QH edge states.

The studied devices consist of two monolayer graphene flakes that are stacked with a relative twist misalignment (panels (a) and (b) of Fig. 3-1). The twist causes a low

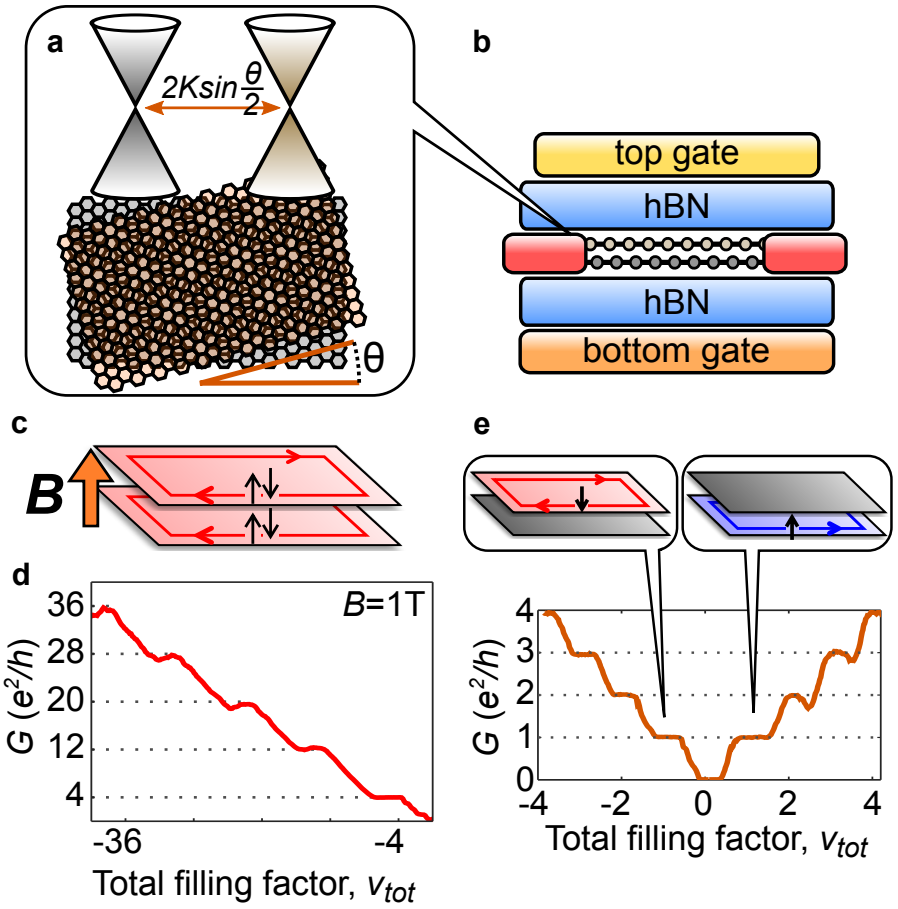

Figure 3-1: Quantum Hall effect in twisted bilayer graphene with broken symmetry states. (a) Stacking two graphene layers with a relative twist decouples the Dirac cones from each layer via a large momentum mismatch. In a magnetic field, each layer will develop monolayer graphene-like Landau levels despite the tiny 0.34nm interlayer spacing. (b) Device schematic of twisted bilayer graphene encapsulated in hBN with dual-gates. Contact electrodes are depicted in red. (c) Cartoon of twisted bilayer QH edge states when both layers are at filling factor -2. Each layer has a spin degenerate edge state with a hole-like chirality. (d) 2-probe conductance of a twisted bilayer graphene device at B = 1 T as a function of ν_{tot}. The sequence is exactly double the monolayer graphene sequence of $(2, 6, 10, 14...)\frac{e^2}{h}$26,27. A contact resistance has been subtracted to fit the $\nu_{tot} = -4$ plateau to $4\frac{e^2}{h}$. (e) 2-probe conductance of the same device at $B = 4$T showing broken-symmetry states. Contact resistances have been subtracted from the negative and positive ν_{tot} sides of the data. Note that this trace is taken with a small interlayer displacement field in order to observe all integer steps (see color map in panel (e) of Fig. 3-2. Cartoons depict proposed edge state configurations in the (0,-1) and (+1,0) states.

energy decoupling of the layers, despite their tiny 0.34nm interlayer spacing [22, 44], that allows each layer to develop independent edge states in a magnetic field [44,78–80]

(panel (c) of Fig. 3-1). We fabricate a dual-gated structure where top and bottom gates allow us to control the total charge density of the twisted bilayer and the interlayer electric field (Figure 1b). We define the total applied electron density as $n_{tot} = (C_T V_T + C_B V_B)/e$, where C_T and C_B are the top and bottom gate capacitances per unit area, V_T and V_B are the top and bottom gate voltages, and e is the electron charge. In a magnetic field, B, we consider the total filling factor $\nu_{tot} = n_{tot}(h/e)/B$, which is the number of filled Landau levels (h/e) is the magnetic flux quantum, where h is Planck's constant). Applying antisymmetric gate voltages will impose an interlayer electric field that shifts charges between layers, causing them to have different filling factors. We present this experimental knob as the applied displacement field $D = (C_T V_T - C_B V_B)/2$ divided by the vacuum permittivity ϵ_0.

To establish the degree of interlayer coupling in our devices, we begin by measuring the QH effect. The QH effect is a sensitive probe of electron degeneracy and the underlying symmetries of the Landau levels; as such, the graphene QH effect is different for monolayers [20, 36], AB-stacked bilayers [81], and twisted bilayers [78–80, 82]. Panel (d) of Fig. 3-1 shows a 2-probe conductance measurement, G, as a function of ν_{tot} in a twisted bilayer device at $B = 1$ T. The filling factors of the top and bottom layers are equal during the measurement ($\nu_{top} = \nu_{bottom} = \nu_{tot}/2, D = 0$), resulting in a QH plateau sequence double that of monolayer graphene due to the layer degeneracy. This sequence demonstrates that a large twist misalignment leads to a weak interlayer coupling that does not split the layer degeneracy, and therefore the system can be modeled as two monolayer graphene sheets conducting in parallel [82, 83].

In low-disorder samples, electron exchange interactions break the graphene spin-valley degeneracy, leading to QH ferromagnetism 31-33. We observe such degeneracy breaking at higher field as a sequence of plateaus at all integer multiples of e^2/h from -4 to 4 ($B = 4$ T, Figure 1e). This can be explained by exchange-driven breaking of spin-valley symmetry in each of the graphene layers, combined with the effects of displacement field. For example, at $\nu_{tot} = 0$, both layers are charge neutral and we observe an insulating state ($G = 0$), similar to the exchange-driven insulating state observed in neutral monolayer graphene [39, 40, 85].

Decreasing ν_{tot} from 0 to -1, a small applied displacement field causes charge to be removed from the top layer preferentially. The result is a transition to a $1e^2/h$ plateau, which we explain as conduction through a hole-like edge state in the top layer while the bottom layer remains insulating (panel (e) of Fig. 3-1, left cartoon). Conversely, increasing ν_{tot} to 1 preferentially adds charges to the bottom layer, resulting in an electron-like edge state with conductance of $1e^2/h$ (panel (e) of Fig. 3-1, right cartoon). We label these states by the filling factors on each layer as $(\nu_{bottom}, \nu_{top}) = (0, -1)$ and $(1, 0)$. In monolayer graphene, the filling factor $\nu = \pm 1$ states are thought to be spin polarized due to the combined effects of Zeeman and QH ferromagnetism [39, 77]. At $\nu = 1$, the spin magnetic moment is aligned with the magnetic field; for the hole-like $\nu = -1$ edge state the spin is flipped since it originates from the bulk excited state. If the same effect occurs in twisted bilayer graphene, it should be possible to create a pair of helical edge states with opposite chiralities and opposite spin polarizations by realizing coexisting $\nu = 1$ and $\nu = -1$ states.

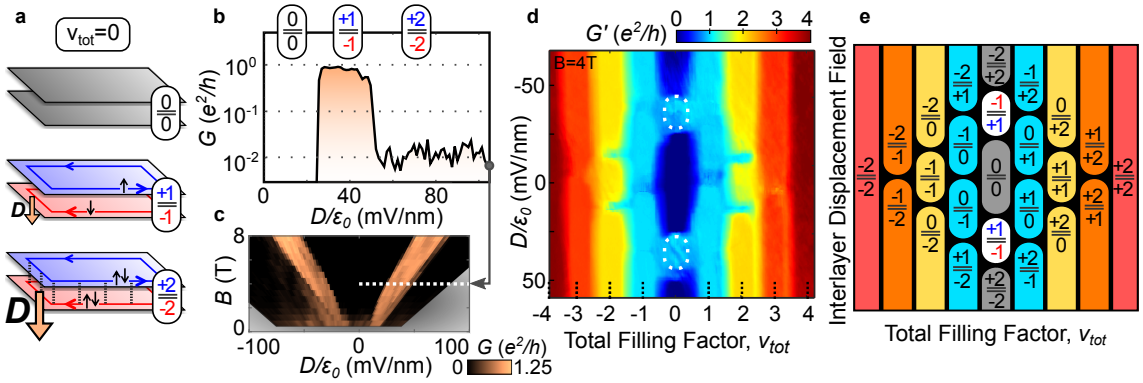

Figure 3-2: Transport in graphene electron-hole bilayers. (a) Cartoons depicting edge state configurations with $\nu_{top} = -\nu_{bottom}$. (b) Conductance for $\nu_{tot} = 0$ as a function of displacement field at $B = 4$T. The (-1,+1) state is conductive while the (-2,+2) state is insulating. (c) Magnetic field dependence of $\nu_{tot} = 0$ line. (d) 2-probe conductance map, G', as function of ν_{tot} and D. Conductance is given by $\nu_{tot}\frac{e^2}{h}$ for all configurations except for the $(\pm 1, \mp 1)$ states. Contact resistances have been subtracted from the positive and negatives sides of the data to fit the $\nu_{tot} = \pm 1$ plateaus. (e) Schematic map of possible filling factor combinations.

We now explore the outcomes when the twisted bilayer is electron-hole doped

such that the layers have edge states of opposite chiralities. Starting with each layer in the insulating state at charge neutrality $(0, 0)$, we imbalance the bilayer with a displacement field such that the charge density from each layer is of equal magnitude but of opposite sign ($\nu_{top} = -\nu_{bottom}$, $\nu_{tot} = 0$, panel (a) of Fig. 3-2). As the displacement field increases, the system first transitions to a conductive state of order e^2/h, and then transitions sharply to another insulating state at higher displacement fields (panels (b) and (c) of Fig. 3-2). Assuming that transitions correspond to layer filling factor changes, we assign the conductive states to the $(\pm 1, \mp 1)$ charge configurations, and the insulating states at higher D magnitudes to the $(\pm 2, \mp 2)$ states. We have consistently observed this conductance sequence in all large-twist bilayer graphene devices that display broken-symmetry states (9 devices in total), with $(\pm 1, \mp 1)$ state conductances varying from 0.8 to 1.5 e^2/h.

To verify the assignment of the $(\pm 1, \mp 1)$ states, we study a wider range of edge state configurations away from $\nu_{tot} = 0$. Panel (d) in Fig. 3-2 shows the 2-probe conductance as a function of ν_{tot} and displacement field. The $((\pm 1, \mp 1)$ states form clearly defined plateaus in the map (white dotted circles). We model the sequence by considering all possible combinations of filling factors in the graphene zeroth Landau level with broken spin-valley degeneracy. The resulting map in panel (e) of Fig. 3-2 matches the entire sequence of plateau transitions observed in the 2-probe conductance (panel (d) of Fig. 3-2) and 4-probe longitudinal resistance measurements (see appendix A Fig. A-1). Furthermore, capacitance measurements on a different sample reveal that the bulk is insulating for all plateaus in the map, as expected for QH states (appendix A Fig. A-2). The consistency of the model with the observed plateaus supports the assignment of the conductive $\nu_{tot} = 0$ states to the $(\pm 1, \mp 1)$ filling factor configurations.

The measured conductances of nearly all the filling factor configurations are given by: $G = \nu_{tot} e^2/h$. Noticeably, only the $(\pm 1, \mp 1)$ states depart from this pattern. When ν_{bottom} and ν_{top} have the same sign, this formula follows directly from the parallel conductance contributions of QH edge states in each layer. But for electron-hole bilayer combinations, such as the $(+2, -2)$ or $(+2, -1)$ states, this equation implies

that conductance contributions from each layer can cancel. For this to occur, there must be a backscattering process that couples opposite chirality edge states between layers (panel (a) of Fig. 3-2, bottom) [82]. Moreover, temperature dependence of the insulating $G = 0$ ($(\pm 2, \mp 2)$ states suggests that this backscattering leads to a complete transport gap (appendix A Fig. A-4). Interlayer backscattering requires tunneling between the closely spaced layers, which may be enhanced at the edge even if it is suppressed in the bulk. In contrast, the same backscattering process is nearly absent in the $(\pm 1, \mp 1)$ states, resulting in a conductive plateau of order e^2/h for a device with greater than 5 μm long edges.

We now show that the $(\pm 1, \mp 1)$ states conduct through counter-propagating edge modes by measuring the nonlocal voltage response in the same device. In the nonlocal measurement, a voltage V_{NL} is measured between adjacent contacts far away from the electrodes where a current I_M is sourced and drained. We find that the nonlocal resistance $R_{NL} = V_{NL}/I_M$ of the $(\pm 1, \mp 1)$ states is 10 to 1000 times larger than the other conductive states (panel (c) of Fig. 3-3, white dotted regions and panel (d) of Fig. 3-3). This nonlocal signal sharply differentiates the $(\pm 1, \mp 1)$ states from being either normal chiral edge states or diffusive conductors: the voltage drop along a chiral edge state is zero, while in a diffusive bulk conductor the nonlocal voltage far away from the source drain electrodes is exponentially suppressed. In contrast to a weak bulk response, the strong nonlocal resistance of the $(\pm 1, \mp 1)$ states signifies that current flows predominately along the edge, with both forward and backward propagating modes equilibrating at the electrodes to give a voltage drop.

Based on the transport data collected – the mapping of the QH plateau sequence and the edge state nonlocal signal – we conclude that at filling factors $(\pm 1, \mp 1)$ conduction occurs through a pair of QH edge states with opposite chiralities (middle cartoon, panel (a) Fig. 3-2). Backscattering between the two counter-propagating modes is strongly suppressed, resulting in a highly conductive 1d transport channel with conductance ranging from 0.8 to 1.5 e^2/h for devices of different edge lengths (0.2-16 μm) (details in appendix A Fig. A-6). This is contrasted with the spin-degenerate $(\pm 2, \mp 2)$ states, where interlayer tunneling leads to insulating behavior in the same

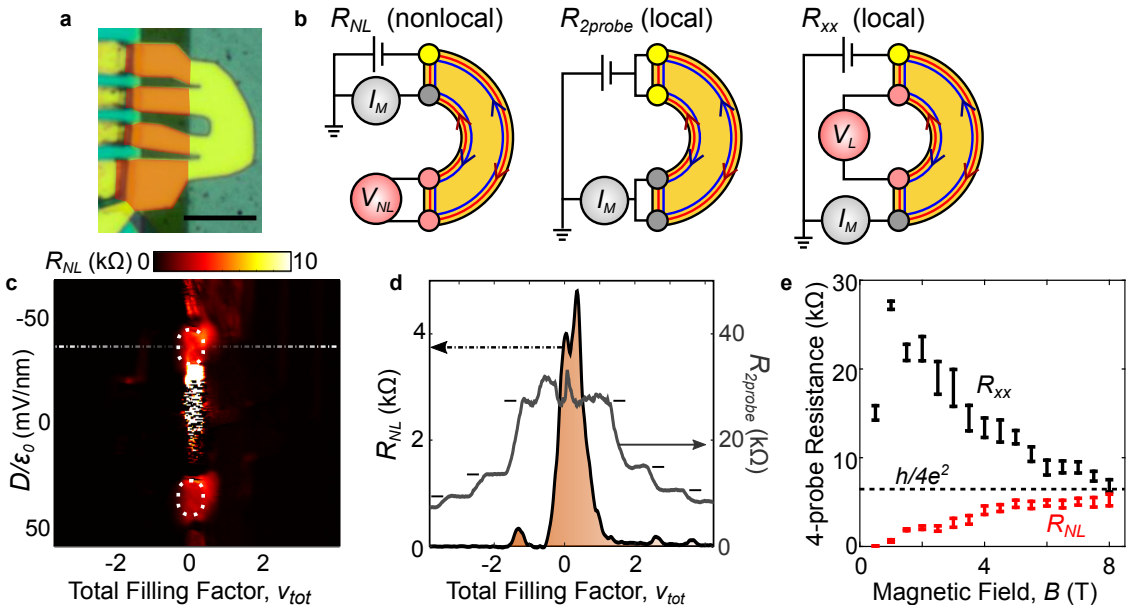

Figure 3-3: Nonlocal measurements of helical edge states. (a) Optical image of 4-probe device with 5 μm scale bar. Graphite leads are highlighted in red, and the gold top-gate which covers the device is highlighted in yellow. (b) Schematic of different measurement configurations for the 4-probe device. (c) Nonlocal resistance, R_{NL}, as a function of ν_{tot} and displacement field, D. Dashed white circles highlight the $(\pm 1, \mp 1)$ states which exhibit a strong nonlocal signal, indicating transport through highly conductive counterpropagating edge modes. Axis ranges are identical to panel (d) of Figure 3-2. In the (0,0) insulating state, R_{NL} fluctuates strongly due to low current signals near the noise limit (bright white features). (d) R_{NL} (black line, left axis) compared to 2-probe resistance, R_{2probe}, (grey line, right axis) of constant D line cut through (+1,-1) state (dashed line in panel (c)). R_{NL} is near zero when R_{2probe} exhibits a conductance plateau, since the voltage drop along a chiral edge state is zero. During plateau transitions, the bulk becomes conductive, resulting in a small peak that is suppressed by the nonlocal geometry of the measurement. (e) Magnetic field dependence of R_{NL} and R_{xx} in (+1,-1) state. In the ballistic limit, each edge segment has resistance $\frac{h}{e^2}$, independent of device length, leading to a 4-probe resistance of $\frac{h}{4e^2}$ that is observed at high fields.

devices (panel (a) Fig. 3-2). A simple explanation for the difference is that the counter-propagating modes of the $(\pm 1, \mp 1)$ states have opposite spin polarizations, which are the expected Zeeman plus exchange-driven ground states for monolayer graphene at $\nu = \pm 1$ [39, 77]. When the spin-wavefunctions on each layer are orthogonal, interlayer tunneling processes are forbidden and the edge states are protected from backscattering. The result is a pair of helical edge states in the $(\pm 1, \mp 1)$ electron-hole

bilayer.

The expected conductance of the helical edge states is $2e^2/h$ when backscattering is completely suppressed (each edge contributes 1 e^2/h in parallel). In our 2-probe measurements, we identify a significant reduction in the conductance due to contact resistances from the electrode-edge state interfaces (see appendix A). To avoid this effect, we measure the 4-probe resistance of the $(+1, -1)$ states as a function of magnetic field in both local (R_{xx}) and nonlocal configurations (R_{NL}) (panel (e) Fig. 3-3). Above 1.5 T, R_{NL} increases slowly until it saturates at high fields, while R_{xx} decreases to approach a similar value, despite the two measurements probing edges of very different lengths. Moreover, the measurements approach $h/(4e^2)$ – the expected value for ballistic counter-propagating edge states that fully equilibrate at the contacts. The convergence of R_{xx} and R_{NL} suggests that backscattering in the helical $(\pm 1, \mp 1)$ states decreases steadily to zero with increasing magnetic field, resulting in a length-independent edge segment resistance of h/e^2.

We now turn to the low field regime of the $(\pm 1, \mp 1)$ states (panel (e) Fig. 3-3). At zero magnetic field, the nonlocal resistance is insignificant (1-10 Ω); as the magnetic field rises to 1.5 T, R_{NL} sharply increases by a factor of 100. This coincides with the emergence of clearly distinguished plateaus at $(\pm 1, \mp 1)$ in both the R_{NL} and R_{2probe} maps (appendix A.7). We interpret the sharp increase in R_{NL} as the onset of conduction in the helical edge states at 1.5 T, a comparatively low field that is encouraging for future efforts to engineer topological superconductivity in this helical conductor [61, 64].

One unique advantage of building a helical 1-dimensional conductor from QH edge states is the possibility of extending the system to fractional edge states [37, 38]. As a promising step in this direction, we have observed the fractional QH effect in our high-quality devices. Panel (a) of Fig. 3-4 shows an R_{xx} measurement taken at $B = 9$ T, where clear minima are observed at fractional values of $\nu_{tot} = \pm 1/3, \pm 2/3, \pm 4/3, and \pm 5/3$. Simultaneous with the R_{xx} minima, we observe plateaus in $1/R_{xy}$ Hall measurements (panels (b) and (c) of Fig. 3-4). From the location of the line cuts in panel (b) of Fig. 3-4, we deduce that one layer is in the $\nu = 0$ insulating state, while

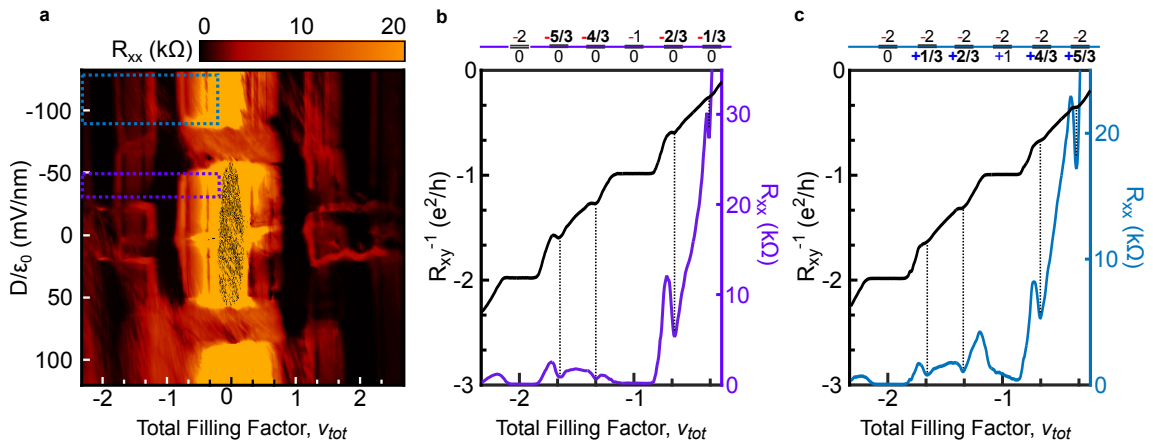

Figure 3-4: Fractional QH effect in twisted bilayer graphene. (a) Rxx measurements at B = 9 T as a function of ν_{tot} and D shows clear minima at fractional values of $\nu_{tot} = \pm 1/3, \pm 2/3, \pm 4/3, \pm 5/3$ indicating fractional quantum Hall states. Some electron-hole regions are obscured by contact-resistance effects at high fields. (b & c) Comparison of R_{xx} and R_{xy} line cuts showing the bilayer fractional quantum Hall effect. R_{xx} minima at fractional values of ν_{tot} line up with plateaus in the measurement of $1/R_{xy}$. Plotted lines are averages over a range of D field values as indicated by the colored rectangles in the colormap. For the line trace in (b), measurements correspond to fractional states in the top layer and an insulating $\nu = 0$ state in the bottom layer. For (c), data corresponds to electron-hole combinations.

the other layer hosts a fractional edge state. Interestingly, we also observe fractional states in the electron-hole bilayer regime (panel (c) Fig. 3-4), with clear fractional QH states that we identify with the $(+1/3, -2)$, $(+2/3, -2)$, $(+4/3, -2)$ and $(+5/3, -2)$ states. The Hall measurements follow $1/R_{xy} = \nu_{tot} e^2/h$, suggesting again the role of interlayer tunneling, in this case resulting in coupling and complete backscattering between fractional and integer edge states on different layers. These observations of fractional QH states pave the way towards realizing a fractional quantum spin Hall state – a key ingredient in recent proposals to construct fractional generalizations of Majorana Fermions [68–70].

3.4.1 Challenges in Measuring Electron-Hole Systems

All 2-probe measurements include the effects of contact resistance originating from the metal electrodes, the metal-graphene interface, and the graphene leading up to

the primary device region. This is often seen as a suppression of the conductance of quantum Hall plateaus. We find that this effect can be corrected by subtracting a single contact resistance value for negative negative filling factors, and a different value for positive filling factors, where details of the procedure is outline in Appendix A.

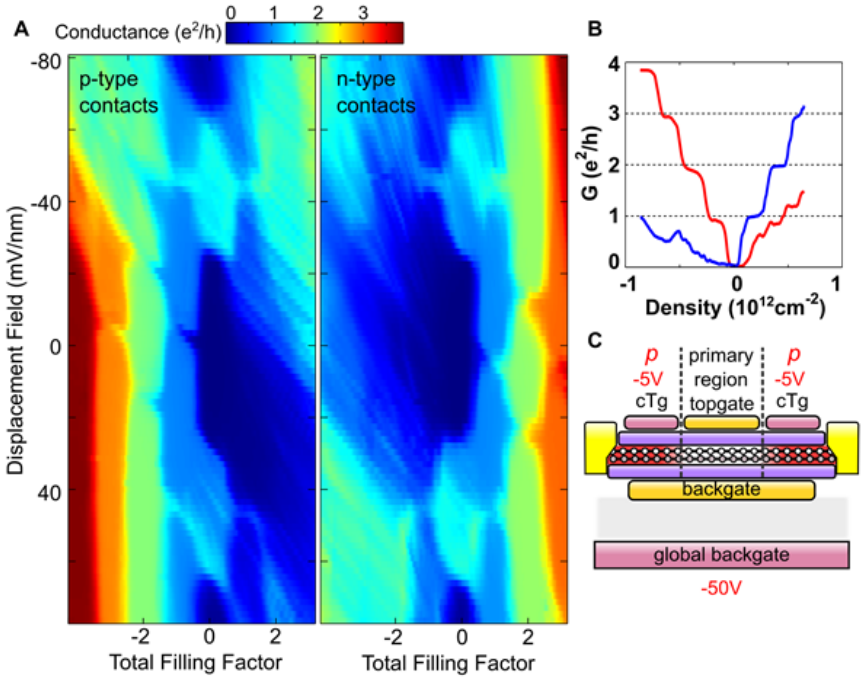

Figure 3-5: Gate-tunable contacts can switch from making good contact to either negative ν_{tot} states or positive ν_{tot} states (Sample B). (A) Conductance maps for a device with gate tunable contacts. P-doped contacts result in clear measurements of the p-side of the data (negative filling factor) with strong suppression of the conductance for the n-side (positive filling factor). The converse is true for n-doped contacts. In both measurements the contact resistance in the well-measured plateaus is less than 100 Ohms. (B) Conductance plateaus for p-doped (red) and n-doped (blue) contacts. (C) Cross-section cartoon of device. The contact topgates (cTg) and the global backgate control the doping of the twisted bilayer graphene between the primary region of the device and the metal electrodes.

One cause of the asymmetry in the contact resistance between the negative and positive filling factors comes from the formation of pn junctions in the graphene which lead to extra resistance. These arise because of changes in doping in the graphene between the dual gated region and the contacts. For example, chromium-gold alloy electrodes tend to locally p-dope graphene near the contact, which will naturally

cause a pn junction to arise when measuring n-doped graphene. The formation of pn junctions can be controlled by using extra gates to control the sign of the charge density outside of the primary device region under study. The effect of this can be seen in Fig. 3-5, which shows the measurement of conductance plateaus in a twisted bilayer graphene device for p-doped contacts and n-doped contacts. In the case of p-doped contacts, there is no pn junction formed when measuring negative filling factors and the plateaus have a very small contact resistance of order 100 Ω. By contrast, measurements of the positive filling factors has a very strongly suppressed conductance with the p-doped contacts. The map can be inverted by switching to n-doped contacts. To accomplish this contact doping control we use a device structure that has extra local topgates and a global Si backgate which dopes the twisted bilayer graphene all the way up to the metal electrodes. This allows us to tune the doping of the bilayer outside of the main region.

The formation of pn junctions at the contact interface presents a fundamental issue when measuring an electron-hole bilayer edge state. Because the state is made up of both p-doped and n-doped graphene, there will always be a pn junction formed when the contacts are of only one doping type. In fact, we observe that this effect can nearly shut off current injection into one of the layers, since the pn junction necessarily passes through zero density, which is insulating at high magnetic fields [77]. A measurement of this effect is presented in Fig. 3-6. Often, we observe that the conductance of the helical edge states will be close to the conductance of the $\nu_{tot} = -1$ plateau, as conductance is limited to only one of the layers. Using graphite contacts (as for sample W discussed in section 3.4), somewhat mitigates this problem since graphite has a similar work function to graphene and hence has less contact doping effects.

By having multiple gate-tunable contacts, it should be possible to have simultaneous independent contacts to both the top and bottom layers by having simultaneously contacts which are p-doped and n-doped. Fig. 3-7 shows a test of this idea using a 4-probe device with independent topgates on each of its contacts to locally control the doping. As expected, the conductance of the (-1,0) state is maximized for p-doped contacts, and likewise the (0,+1) state conductance is maximized for n-doped

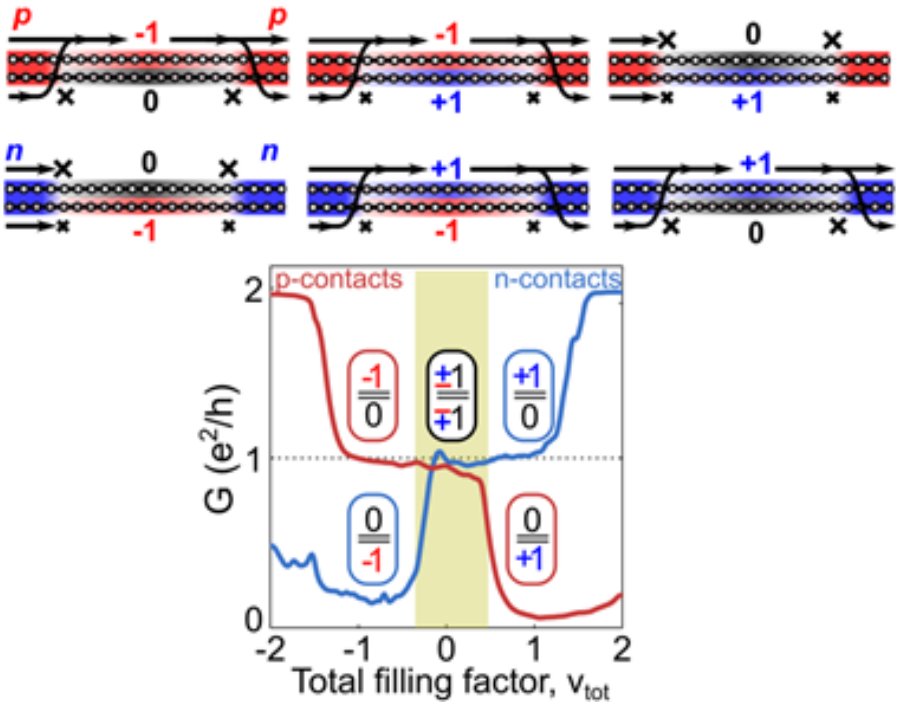

Figure 3-6: Gate tunable contacts can selective inject current into only one layer (Sample B). Top – Cartoons show current flow paths depending on the filling factor of the layers and whether contacts are p-doped or n-doped. Current flow is blocked at pn junctions because the zero density state is insulating. Bottom – Conductance near the $(\pm 1, \mp 1)$ states for p-dope and n-dope contacts. In the $(\pm 1, \mp 1)$ states, the contacts can only inject current effectively into one layer.

contacts. By contrast, the (-1,+1) state conductance is maximized when there are two pairs of both n-doped and p-doped contacts. This is another confirmation of the electron-hole bilayer nature of the helical $(pm1, \mp 1)$ states.

3.4.2 Epilogue & Further Developments

The experiment outlined in the previous section definitively answers the questions outlined in section 3.1.1. In particular, we observe that quantum Hall modes at the edges interact strongly, where the Hall conductance of the system is given by the *sum* of the filling factors in both layers. The exception to the rule is the case where both layers have $\nu = +1$ and $\nu = -1$ states, where spin protection is the most likely mechanism that prevents hybridization between the edge modes. The suppressed interlayer tunneling in this regime allows the creation of a quantum spin

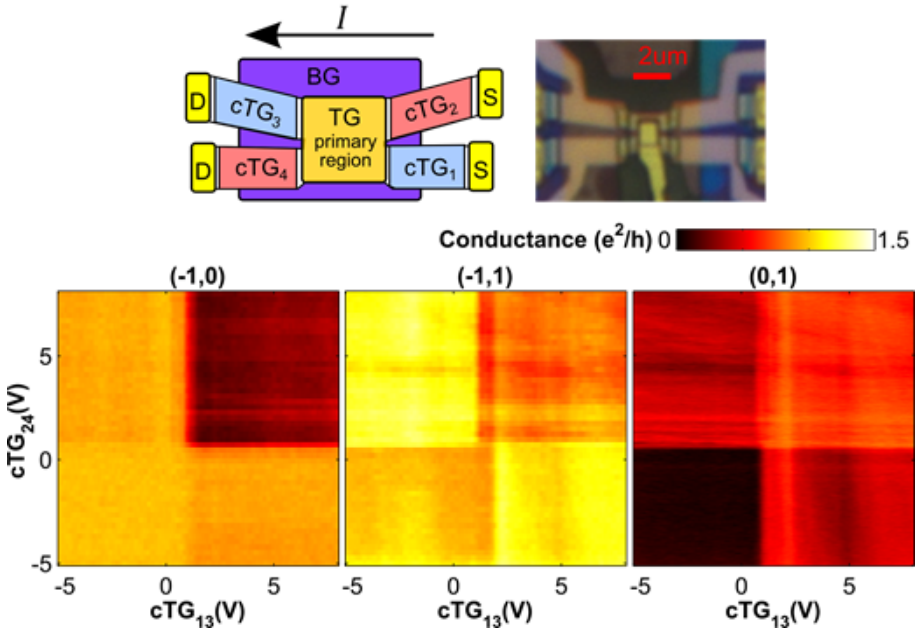

Figure 3-7: Simultaneous p- and n-type contacts gives the best measurement configuration (Sample B). Top – Cartoon schematic and optical image of device with four independent gate-tunable contacts labeled cTG1,2,3,4. Bottom – Conductance maps in (-1,0) (-1,1) and (0,1) states as a function of the contact topgate values. 2-probe conductance is measured between the source and drain electrodes (S and D in the top cartoon). cTG1 and cTG3 are swept together (cTG13) and likewise for cTG2 and cTG4 (cTG24). For the (-1,0) state, the highest conductance is for p-type contacts (negative cTG). Similarly, the (0,1) state has highest conductance for n-type contacts (positive cTG). By contrast, the (-1,1) state measurement has the highest conductance when there is simultaneous both p-type and n-type contacts (cTG13 and cTG24 opposite sign). This is further evidence that the (-1,1) state is made up of both p-type and n-type states.

Hall state, whose existence is supported by non-local measurements and capacitance measurements which rule out alternative conductive electronic states in the bulk. We also demonstrated, for the first time, that large angle twisted bilayer graphene can support fractional quantum Hall edge states.

Some further questions follow from the completion of this work. Firstly, the existence of fractional quantum Hall states in twisted bilayer graphene could prove to be a potential platform for building a fractional quantum spin Hall state, which has been predicted to host more complex non-abelian statistics [68–70]. Secondly, our work observed interactions between integer and fractional quantum Hall edge modes, whose Hall conductance is consistent with an interlayer tunneling mechanism.

Since fractional quantum Hall edge modes are expected to have very weak tunnelling behavior [89–91], the nature of these edge modes interactions remains a theoretical curiosity and should be further investigated.

THIS PAGE INTENTIONALLY LEFT BLANK

Chapter 4

Strong Interactions in Small Angle Twisted Bilayer Graphene

4.1 Introduction

This chapter of the thesis describes the experimental work and results on small angle twisted bilayer graphene, where we observe the effects of the interplay between interlayer hybridization between the graphene layers and the moiré potential on the transport properties in this small angle regime.

4.1.1 Experimental Objectives

Although there have been many transport studies on the effects of the moiré potential in van der Waals heterostructures, these experiments have mainly been confined to graphene/hBN systems, where interlayer hybridization effects are minimal due to the large band gap in hBN [92]. Additionally, the size of the moiré wavelengths have been limited by the lattice mismatch between graphene and hBN, whereas this would not be the case in small angle twisted bilayer graphene. The main questions that I aim to address are as follow:

1) What is the combined effect of the moiré potential and strong interlayer hybridizations on the magneto-transport properties on small angle twisted bilayer graphene?

2) Are there certain twist angles that exhibit special transport behavior?

4.2 Experimental Details

The steps involved in the experimental study is similar to that outlined in Chapter 3. The key difference is the need to precisely control the twist angle between the two graphene sheets, and this is achieved via the "tear-and-twist" method which is outlined in Appendix B. The main idea behind this method is to partially tear a flake of graphene, rotate it with the desired twist angle, and transfer it onto the remaining portion. By using the same piece of graphene, we can ensure that both layers of graphene in the twisted bilayer graphene have the same original crystallographic orientation, allowing us to definitively control the twist angle. With this method, we can control the twist angle to a precision of 0.1°.

4.3 Initial Experimental Results

The first experimental results came as a fortuitous accident: while making many samples of large angle twisted bilayer graphene, one of the measured samples happened to have a small twist angle. Fig. 4-1 shows the two probe-conductance trace of this particular sample as a function of number density at zero magnetic field. The most striking feature of the conductance trace is the marked difference in behavior compared to monolayer graphene (shown in dashed lines), suggesting strong interlayer coupling effects. On closer inspection, we observe three main characteristics: (1) prominent trace features are symmetric about the charge neutrality point, (2) the existence of two insulating states at a density corresponding to full filling of the superlattice cell, even though we have two graphene sheets at a high number density, (3) prominent conductance dips near half-filling of the superlattice unit cell.

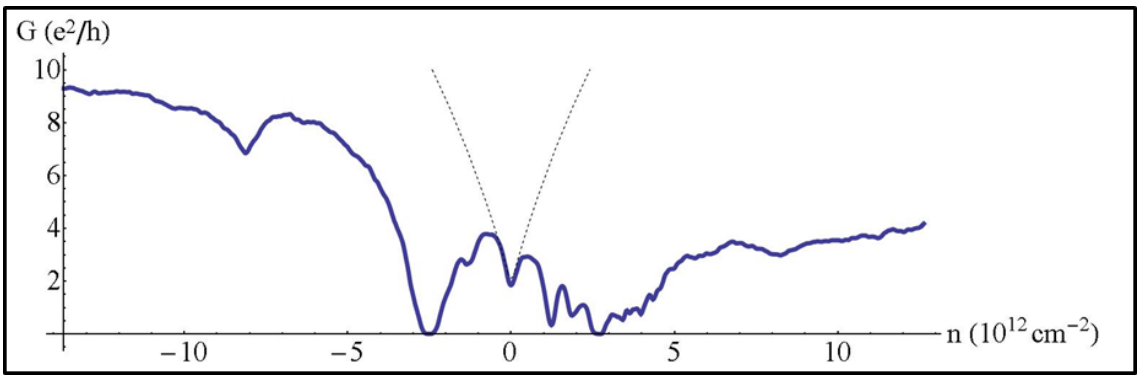

Figure 4-1: Two-probe conductance trace of a small angle twisted bilayer graphene sample at zero magnetic field. Dotted inset line shows the typical conductance curve of monolayer graphene. Striking transport features are observed, including insulating states at full filling of the superlattice cell, and conductance dips near half filling.

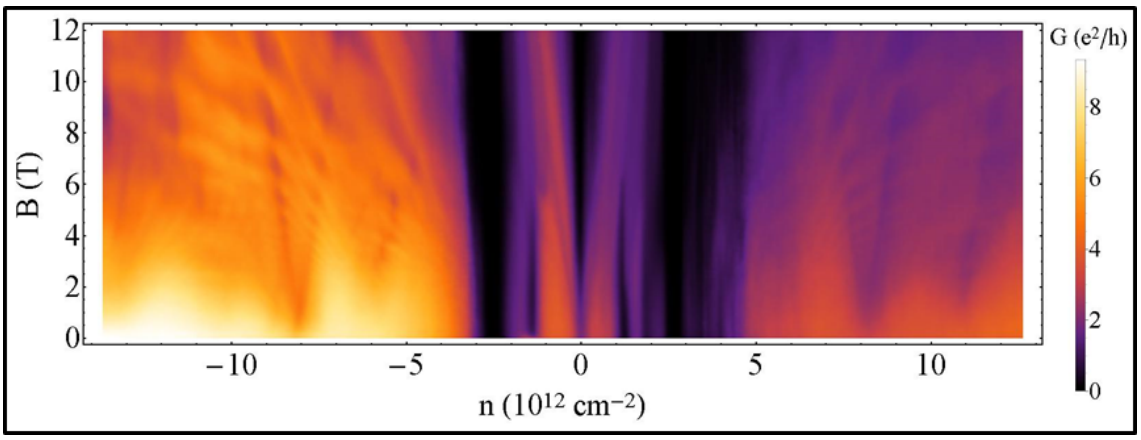

Figure 4-2: Two-probe magneto-conductance measurement of a small angle twisted bilayer graphene sample. Insulating states are not observed to disperse with increasing magnetic field. Multiple satellite fans are also observed to emanate from several locations. Conductance dips near half filling of the superlattice is observed to disappear at higher magnetic fields.

Fig. 4-2 shows a magneto-transport measurement of the small angle sample as a function of number density n and magnetic field B. We observe three main features in this measurement: (1) the insulating states do not disperse with magnetic field, suggesting that it is a constant density feature, (2) the appearance of multiple satellite

Landau fans emanating from multiple number density positions, in addition to the main central Landau fan at charge neutrality, (3) the conductance dips near half-filling of the superlattice cell disappears at higher magnetic fields.

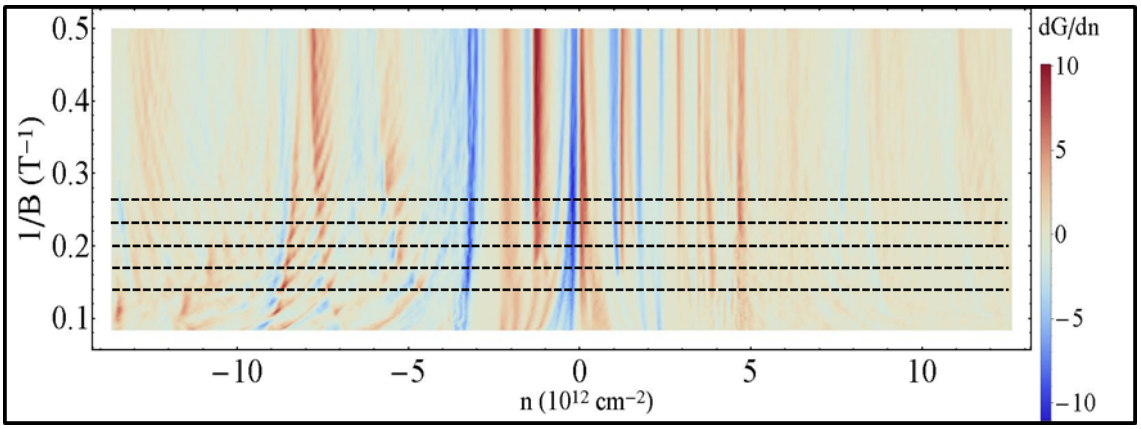

Figure 4-3: Derivative of the magneto-conductance measurement in Fig. 4-2, but plotted in $1/B$ instead to accentuate the periodic crossings of the satellite fans. Dotted inset lines shows the periodic crossings. Fitting the periodicity gives a twist angle of 1.1° in this sample.

An estimate of the twist angle was extracted from the periodic crossings of the satellite fans. Fig. 4-3 shows the magnetotransport measurement plotted in $\frac{1}{B}$, which emphasizes the periodic crossings. Periodicity in $\frac{1}{B}$ suggest an inherent area in the system (like in Shubnikov-de Haas oscillations), where the superlattice area would be a natural area in this case. The periodicity in the fan crossings is expected to correspond to fitting an integer number of magnetic flux quantum in each superlattice unit cell with area A_{SL} i.e. $\frac{\Phi_0}{B} = nA_{SL}, n \in \mathbb{Z}$. Fitting the data according to this relation yields a superlattice area of 1.4×10^{-12} cm^2, which corresponds to a twist angle of 1.1° and a superlattice cell density of 2.48×10^{12} cm^{-2}, which is consistent with our magnetotransport data.

Unfortunately, this sample was a two-probe device which meant that we could not perform 4-probe measurements of longitudinal resistances and Hall conductances. But the set of data obtained from this sample offered great insight to the unusual transport properties in small angle twisted bilayer graphene, especially the insulating

states at the superlattice density, and possible electron-electron interactions at half-filling. Our subsequent work on small angle twisted bilayer graphene sought to further investigate these properties, which is covered in the following section.

4.4 Superlattice-Induced Insulating States and Valley-Protected Orbits in Twisted Bilayer Graphene

The following section is a text reproduction from Cao, Luo et al. [93].

Twisted bilayer graphene (TwBLG) is one of the simplest van der Waals heterostructures, yet it yields a complex electronic system with intricate interplay between moiré physics and interlayer hybridization effects. We report on electronic transport measurements of high mobility small angle TwBLG devices showing clear evidence for insulating states at the superlattice band edges, with thermal activation gaps several times larger than theoretically predicted. Moreover, Shubnikov-de Haas oscillations and tight binding calculations reveal that the band structure consists of two intersecting Fermi contours whose crossing points are effectively unhybridized. We attribute this to exponentially suppressed interlayer hopping amplitudes for momentum transfers larger than the moiré wavevector.

The plethora of available two dimensional materials has led to great interest in investigating novel quantum phenomena that can originate from assembling them into van der Waals heterostructures [94]. One of the simplest such heterostructures is twisted bilayer graphene (TwBLG), consisting of two sheets of monolayer graphene stacked on top of each other with a relative twist angle. Despite the material simplicity, an intricate interplay between moiré physics and interlayer hybridization effects exists in TwBLG — one striking consequence is that the heterostructure can host an insulating state even though it comprises two sheets of high quality conductors. The intrinsic band gap is due to interlayer hybridization; this is in contrast to the graphene/hexagonal boron nitride (h-BN) moiré heterostructure where the band gap

at charge neutrality [47,95] arises from other mechanisms such as sublattice symmetry breaking, strain effects, and many-body interactions [96–98]).

Due to the different orientation of the two graphene lattices in TwBLG, a periodic modulating potential related to the resultant superlattice moiré pattern emerges. Furthermore, the bands in both graphene layers can readily hybridize and exhibit strong interlayer coupling [22, 25, 99–101]. The extent of the hybridization depends critically on the relative twist angle θ. For $\theta > 3°$, the Dirac cones of the two layers are separated far apart in momentum space, and hybridization occurs at high energies and densities [45, 102] which are typically inaccessible in transport experiments. On the other hand, for small θ, hybridization occurs at low energies between nearby K points of opposite layers, leading to a drastically reduced Fermi velocity which has been confirmed by scanning tunneling microscopy experiments [43, 44, 103, 104].

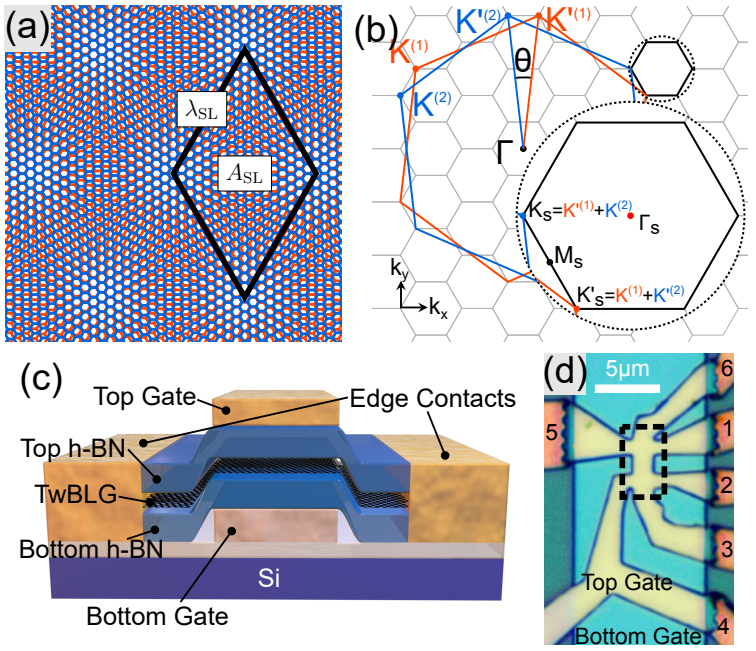

Figure 4-4: (a) Schematic of TwBLG and its superlattice unit cell. $\lambda_{SL} = \frac{a}{2\sin(\theta/2)}$ (a is the lattice constant of graphene) is the moiré period and $A_{SL} = \frac{\sqrt{3}}{2}\lambda_{SL}^2$ is the unit cell area. (b) The orange and blue hexagons denote the original Brillouin zones of graphene layer 1 and 2 respectively. In k-space, the band structure is folded into the MBZ which is defined by the mismatch between the hexagonal Brillouin zones of the two honeycomb lattices. (c) Illustration of the cross section of our device. (d) Optical image of $\theta \approx 1.8°$ device S1. The hall bar in the dashed rectangular region is completely free of bubbles and ridges.

In a moiré superlattice [Fig. 4-4(a)], the band structure must be reconsidered in a mini Brillouin zone (MBZ) that corresponds to the superlattice unit cell, as shown in Fig. 4-4(b). At low twist angles, theory suggests that the interlayer interaction significantly distorts the band structure of TwBLG, such that the system can no longer be described by two weakly coupled Dirac cones at low energies (which is valid for large angle TwBLG) [80, 105]. In particular, various calculations predict that a single-particle gap can be opened at the Γ_s point of the MBZ in a specific range of twist angles when the lowest energy superlattice bands are filled [Fig. 4-5(b)] [80,106]. This can be understood to arise from the strong interlayer coupling in small angle TwBLG, which allows for substantial interlayer Bragg reflections off the superlattice potential. On the other hand, a long-range periodic potential in itself is insufficient to open a gap at the superlattice points in a graphene/h-BN heterostructure, as there is no low-energy state in h-BN that can couple to the graphene bands [92]. Despite these theoretical predictions for TwBLG, no experimental evidence to date directly points to the existence of global energy gaps when the superlattice bands are completely filled [107, 108].

In this Letter, we report observations of insulating states at the superlattice band edges in small angle TwBLG via transport measurements, where we measure thermal activation gaps of 50 meV and 60 meV on the electron and hole sides respectively. Additionally, in the quantum Hall regime, the eight-fold degeneracy of the Dirac points transitions to a four-fold degeneracy near the superlattice band edge. Finally, by comparing Shubnikov-de Haas oscillations with a tight-binding model, we deduce that the band structure consists of two intersecting Fermi contours whose crossing points are essentially not hybridized due to the exponentially suppressed hopping amplitudes for momentum transfers much larger than the moiré wavevector [24, 101, 109].

We fabricated fully-encapsulated TwBLG devices with $\theta < 2^\circ$ using a modified dry-transfer method [86]. The samples are dual-gated for independent control of the total charge density and interlayer potential difference [109]. A local metallic bottom gate is used to screen the charge impurities present in the silicon oxide substrate, and

one-dimensional edge contacts are used to contact the TwBLG [86]. A 'tear-and-stack' technique was also developed to enable sub-degree control of the twist angle [109,123]. We used an *ab initio* tight-binding model for the calculation of band structures and related quantities [106,109].

Our samples show Hall mobilities exceeding $\sim 20\,000\,\mathrm{cm^2\,V^{-1}\,s^{-1}}$ at $T = 4\,\mathrm{K}$. Fig. 4-5(a) shows the conductivity of two TwBLG samples: sample S1 with a low twist angle (we focus on device S1 in this Letter, but data on other small angle TwBLG devices with similar behaviors are also presented in the supplement [109]) and sample S0 with a large twist angle ($> 3°$). In both samples, the conductivity minimum centered at zero density corresponds to the degenerate Dirac points in both layers of graphene. However, for the small angle sample S1, we observe two insulating states occurring at total carrier densities of $n \approx \pm 7.5 \times 10^{12}\,\mathrm{cm^{-2}}$, which are symmetric on both sides of the charge neutrality point.

We attribute these insulating states to the gaps occurring at the Γ_s point of the MBZ when the lowest-energy superlattice bands are fully filled. The *ab initio* tight-binding calculation of the commensurate $\theta = 1.8°$ TwBLG is shown in Fig. 4-5(b). The low-energy bands of TwBLG retain the valley polarizations of its constituent graphene layers, *i.e.* valley continues to be a valid quantum label for these bands. The bands colored in orange correspond to K-valleys, while the blue bands correspond to K'-valleys. Although the K valley of one graphene layer and the K' valley of the other layer occupy the same k-points in the MBZ along the Γ_s—K_s line (purple lines), their hybridization is suppressed because of the large momentum mismatch in the original graphene Brillouin zone, as explained later in this Letter. Therefore, valley still provides a 2-fold degeneracy even far away from the Dirac point, and the total density required to fill up to the insulating gaps is equal to 4 times the MBZ area: 2 from the valley quantum number and 2 from spin. From the deduced density $n = \pm 7.5 \times 10^{12}\,\mathrm{cm^{-2}}$ at the center of the insulating states, we derive the unit cell area of the superlattice to be $A_{\mathrm{SL}} = 4/n = 53.3\,\mathrm{nm^2}$, with a corresponding twist angle of $\theta = 1.8°$. This agrees well with our target value of $\theta = (2.0 \pm 0.5)°$.

To study thermally activated transport of the insulating states, we measured the

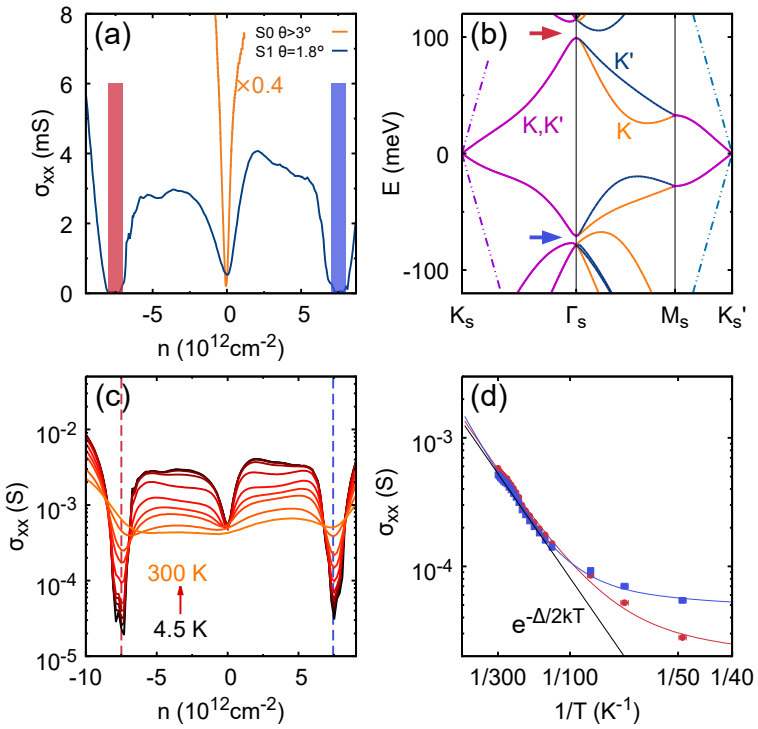

Figure 4-5: (a) Comparison of the conductivity of a large angle TwBLG device S0 and a small angle device S1. The vertical bars around $n = \pm 7.5 \times 10^{12}\,\mathrm{cm}^{-2}$ indicate the insulating states in device S1. (b) Tight-binding band structure of TwBLG with $\theta = 1.8°$. Dashed lines denote the monolayer graphene dispersion with Fermi velocity $v_F = 1 \times 10^6\,\mathrm{m\,s}^{-1}$. The color of the bands denotes the valley polarization: K (orange), K' (navy blue), and valley-degenerate (purple). The arrows indicate the direct band gaps at Γ_s. (c) Temperature dependent conductivity of device S1. (d) Arrhenius plot of the conductivity of the insulating states [indicated by dashed lines in (c)]. Blue and red denote the electron and hole side insulating states respectively. Thermal activation gaps of $\sim$ 50 meV and $\sim$ 60 meV are estimated from the slope for the electron-side and hole-side insulating states respectively.

temperature dependence of the conductivity of sample S1 [Fig. 4-5(c-d)]. The insulating states' conductivities drop by more than an order of magnitude from 300 K to 50 K, and start to saturate below T =50 K. An Arrhenius-like behavior is evident at higher temperatures. From the slope in the Arrhenius plot between 100 K and 300 K, we estimate the thermal activation gaps to be $\sim$ 50 meV and $\sim$ 60 meV for the electron-side and hole-side insulating states respectively. The deviation from Arrhenius-like behavior at low temperatures may be attributed to a variable-range hopping mechanism [109, 111].

Ab initio tight-binding calculation following Ref. [106] shows a gap size of 6mV at the electron side and semi-metallic bands on the hole side, as shown in Fig. 2(b). Other theories range from showing no gap [22, 25, 78, 101] to T =10 meV gaps on both electron and hole sides [80, 105]. In a departure from all these models, our measured activation gaps are much larger than any of these predictions. Contributing factors may include an underestimation of the interlayer interaction strength in these calculations, but these are unlikely to account for most of the difference. Physical effects of lattice strain, as recently proposed to explain the energy gap in monolayer graphene/h-BN structures, may also play a significant role [96,97]. A third possibility is an excitonic instability, as reported for Bernal bilayer graphene [112–114]. The small single-particle gap and the 2D nature of the system make it possible for the excitonic binding energy to be the larger energy scale.

Next, we apply a perpendicular magnetic field to the TwBLG sample. Fig. 4-6 shows the longitudinal resistivity, ρ_{xx}, and the Hall conductivity, σ_{xy}, as a function of the total density n and the magnetic field B. In a magnetic field, the Hall conductivity quantizes according to $\sigma_{xy} = \nu e^2/h$, with the filling factor $\nu = n\phi_0/B$, where $\phi_0 = h/e$ is the flux quantum. The central Landau fan that originates from the Dirac cone near zero density generates filling factors of $\nu = \pm 4, \pm 12, \pm 20, \ldots$. This sequence is double that of the monolayer graphene quantum Hall sequence of $\nu = \pm 2, \pm 6, \pm 10, \ldots$, indicating that at low energies a massless Dirac dispersion is retained despite the strong interlayer hybridization [78, 82].

However, the Landau fans originating from the insulating states differ markedly from the massless Dirac nature of the central Landau fan. As shown in Fig. 4-6(c), the Landau level sequence near the insulating states is $\nu = 0, \pm 4, \pm 8, \pm 12, \pm 16, \ldots$, indicating a non-Dirac massive band [115]. The 4-fold degeneracy of this sequence is attributed to the spin degeneracy and the Fermi contour degeneracy from the valley quantum number near the Γ_s point. The lack of a Berry phase on the other hand indicates a parabolic band edge at the insulating states [80]. Additionally, we observe a sign change of σ_{xy} at $n \approx +(-)3 \times 10^{12}\,\mathrm{cm}^{-2}$, indicating a transition of massless Dirac electron-like (hole-like) carriers to massive hole-like (electron-like) carriers.

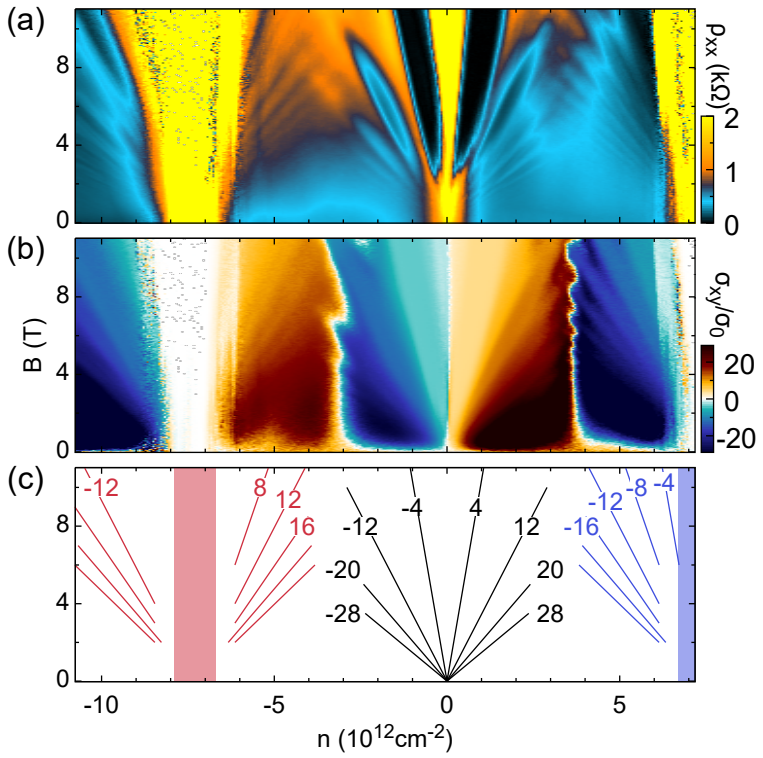

Figure 4-6: (a) Longitudinal resistivity and (b) Hall conductivity in unit of $\sigma_0 = e^2/h$ versus the total density and the magnetic field. Measurements are taken at $T = 40\,\mathrm{mK}$. (c) Reconstructed Landau level structure from the plateau values. The central Landau fan emanating from the Dirac point at zero density has an 8-fold degenerate half-integer quantum Hall sequence, while the Landau fans originating from the superlattice gaps have a 4-fold degenerate massive parabolic quantum Hall sequence.

We further investigate this transition by examining the density of states $D(E)$ in TwBLG through Shubnikov-de Haas (SdH) oscillations. By fitting the temperature-dependence of the SdH oscillation amplitude to the Lifshitz-Kosevich formula, we can obtain the cyclotron mass m^* at the Fermi energy, which for a two-dimensional system is proportional to the density of states per Fermi pocket at the Fermi energy, *i.e.* $m^* = \frac{h^2}{2\pi} D(E)/N$, where N is the degeneracy. The blue data points in Fig. 4-7(a) are the extracted cyclotron masses as a function of total density. For TwBLG, m^* is expected to peak at the van Hove singularities [115] and to approach zero at both the Dirac point and the superlattice gaps. This is consistent with our observation that the slope of m^* vs. density changes sign, in correspondence to the sign of the charge carrier extracted from Hall measurements. Additionally, we find that near the Dirac

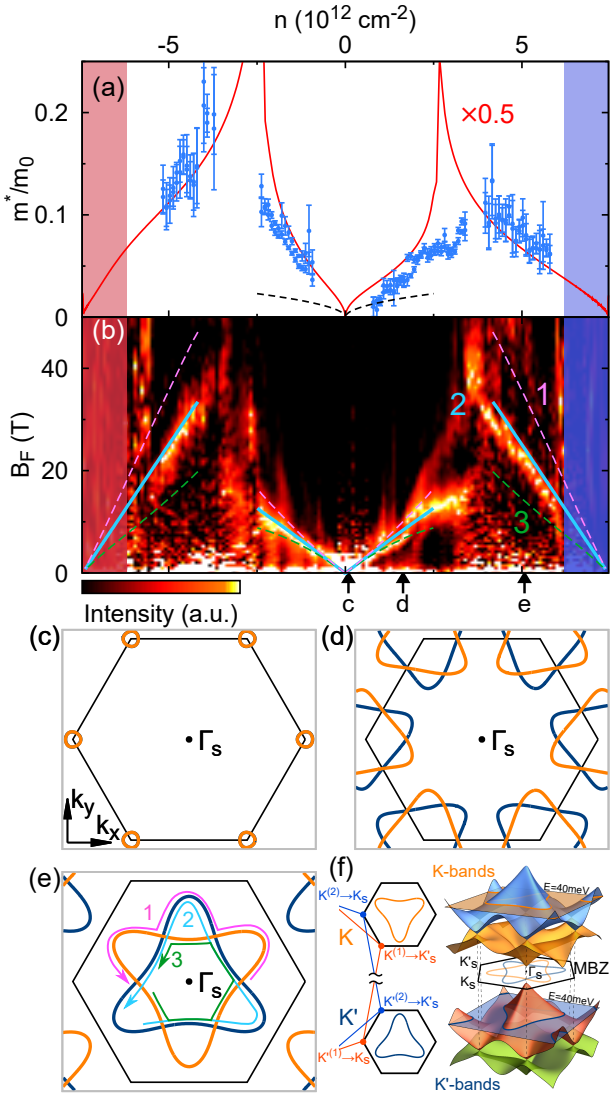

Figure 4-7: (a) Cyclotron masses and (b) oscillation frequencies extracted from SdH measurements. The red curve is the numerically calculated cyclotron mass (normalized by a factor of 0.5) and the black dashed curve is the effective mass if the interlayer interaction is ignored. Lines colored pink, blue and green denote the expected slope for the outer star orbit, triangular orbits and inner hexagon orbit shown in (d) and (e). (c-e) Fermi contours at densities shown as arrows positioned below the density axis in (b). Orange orbits are K-polarized, and blue orbits are K'-polarized. (f) 3-D Illustration of the low-energy band structure. The two sets of bands are valley-polarized in the original K, K' valleys of the constituent layers. For example, the K sub-bands result from the hybridization of $K^{(1)}$ and $K^{(2)}$ Dirac cones. The same applies for the K' sub-bands.

points, m^* is about 2.5 times larger than that of monolayer graphene, indicating a similar reduction in the Fermi velocity as observed in other studies [43, 44, 103, 104].

The experimental data agrees well with theoretically calculated m^* [red curve in Fig. 4-7(a)] up to a uniform scaling factor of 0.5 for all densities, which may be attributed to underestimation of the band width in the *ab initio* calculations [116] or to corrections to the m^* term in the Lifshitz-Kosevich formula for 2D systems [117].

Further information about the band structure is obtained from analysis of SdH oscillation frequency at different gate voltages. Fig. 4-7(b) shows the Fourier transform of the oscillations in $1/B$ at each gate voltage. The oscillation frequency provides the area of the Fermi pocket. One expects a linear relationship between the oscillation frequency and the total density: $B_F = (\phi_0/N)|n|$. Near the Dirac point at low densities, we observe a small oscillation frequency corresponding to the circular Fermi contour as shown in Fig. 4-7(c). As we increase the density, the slope gives $N = 8$, as expected from the 2-fold layer, valley, and spin degeneracies. Near the insulating states, we find a single oscillation frequency with $N = 4$. Calculated band structures present a Star-of-David Fermi contour, which suggests three possible electron orbits as illustrated in Fig. 4-7(e): (1) the outer star orbit, (2) the triangular orbits, and (3) the inner hexagon orbit. We overlaid the numerically extracted areas of these three types of orbits on top of the experimental data in Fig. 4-7(b), and only the triangular orbit fits with the experimental data. A similar scenario occurs for the Star-of-David Fermi contours around the valley points of the MBZ as shown in Fig. 4-7(d). This suggests that the crossing points of the two triangular orbits are protected [118].

The large momentum mismatch between the original graphene K and K' points provides a natural explanation for the suppressed hybridization. The MBZ arising from the moiré pattern folds the graphene band structures of both layers and creates degeneracies within it. The degree of hybridization at these degenerate crossings depends on the interlayer hopping amplitude: crucially, this amplitude varies exponentially with the momentum difference of the original states, with a characteristic momentum scale of the moiré wavevector k_{SL} [24, 25, 101, 109]. Since the $K^{(1)}$ and $K^{(2)}$ points (superscript labels the layer) are separated by a momentum less than k_{SL}, the Dirac cones at $K^{(1,2)}$ hybridize strongly, and similarly for the $K'^{(1,2)}$ pair as well. These two pairs of hybridized Dirac cones form two time-reversed Fermi surfaces of

opposite valley polarizations. Finally, while these two Fermi contours intersect within the MBZ, coupling these states requires a momentum difference corresponding to the inter-valley momentum of monolayer graphene [see Fig. 4-7(f)], which is much larger than k_{SL}. The exponentially small interlayer hopping amplitude at this momentum leaves the crossings effectively unhybridized. As a result, we observe a single Fermi surface area consistent with the pair of triangular valley polarized orbits.

In summary, we have experimentally studied the magnetotransport properties of high-quality TwBLG samples in the low twist angle regime, where we have observed insulating states induced by strong interlayer interactions. The larger than theoretically predicted gap sizes observed in the experiment indicate the possibility of other effects beyond the superlattice modulation and interlayer hybridization, such as strain and many-body interactions, therefore providing motivation for further theoretical and experimental studies in TwBLG.

4.4.1 Epilogue & Further Developments

The experiment outlined in the previous section showed the rich range of transport behavior that arises from the interplay between interlayer hybridizations and the moiré potential in small twist angle graphene. In particular, we observe insulating states in multiple samples, with thermal activation gaps in the range of 50 meV. Ab-initio calculations show that for a certain range of twist angles, a global band gap is expected at full filling of the superlattice unit cell, which explains the existence of insulating states at these densities. We also observe a difference in the Berry curvature of the charge carriers around the charge neutrality point and the superlattice density, where the former retains its half-integer Dirac quantum Hall sequence and the latter transits to a massive, non-Dirac quantum Hall sequence.

However, a few questions remain unanswered from the completion of this work. Firstly, the measured thermal activation gaps are several times larger than that predicted by ab-initio calculations, and the role of interactions in explaining this discrepancy remains to be investigated. Secondly, the conductance dips at half-filling of the superlattice unit cell was not fully understood at the completion of this work.

However, further work performed by Yuan et. al. [119, 120] suggested that the twist angle of 1.1^{circ} is extremely crucial, since this angle is of the "magic angles" where the Fermi velocity is renormalized to zero [101], which would strongly enhance the effects of electron-electron interactions. At this magic angle, both Mott insulator type behavior and intrinsic superconductivity are observed in this system, which could serve as a possible explanation for the initially observed conductance dips.

THIS PAGE INTENTIONALLY LEFT BLANK

Appendix A

Supplementary Information for Helical Edge State Conduction in Twisted Bilayer Graphene Experiment

A.1 Method Outline

All twisted bilayer graphene devices were made using a dry-transfer process [86, 87] to create a van der Waals heterostructure consisting of hBN-graphene-graphene-hBN layers. The devices all are dual-gated with a top and bottom gate electrode. For the device leads which contact the dual-gated region, we used two different approaches: graphite contacts and gate-tuned contacts. Graphite contacts provide the simplest approach, where graphite is used as the electrode material to contact the twisted bilayer graphene. The advantage of graphite is that it has a work function similar to graphene, and hence does not cause strong local doping at the contact interface. As a result, graphite can provide good contact to both electron-doped and hole-doped graphene layers, even at high magnetic fields. Graphite contacts are used for the device data presented in Figure 1, 2 and 3 of the main text. An alternative method is

to use local gate electrodes which separately gate the twisted bilayer graphene outside the primary dual gated region. The advantage of this method is that contact resistances can be controllably reduced to sub-100Îľ range, even at high magnetic fields, but can only be used to contact well either electron-doped or hole-doped graphene.

A summary of the typical fabrication steps are as follows:

1. Hexagonal boron nitride and graphene flakes are exfoliated on Si/SiO_2 chips which have been pre-cleaned first in a Pirahna solution, followed by a hydrofluoric acid bath. Graphene flakes are then identified by optical microscopy and checked for cleanliness with an atomic force microscope (AFM).

2. Flakes are picked up and transferred using a transparent polymer stamp made from either polypropylene carbonate (PPC) or polycarbonate (PC). The top hBN crystal is picked up first using the stamp, and then subsequently the hBN is used to pick up two graphene flakes (via strong interlayer van der Waals forces) and then the bottom hBN. The graphene flakes are rotated so that natural edges are mis-aligned to avoid producing a low twist angle sample. For graphite contacts, a layer of thin graphite (<20nm thick) is also picked up that overlaps with the graphene layers to provide electrical contact.

3. The complete stack consisting from top to bottom of hBN-graphene-graphene-hBN is then transferred onto a bottom gate electrode made of either graphite or a thin layer of Pd/Au 40:60 alloy (20nm). The device discussed in the main text is made on a graphite bottom gate. The stack is then measured in an AFM to check for regions free of bubbles and ripples in the stack. To increase flatness, the stack is also either heat cleaned in forming gas ($Ar:H_2$) or in vacuum at high temperatures of 550 degrees Celsius for 30mins to redistribute trapped residue between the flakes.

4. An isolated top gate electrode is made using ebeam lithography and evaporating Cr:Au (1nm:30-50nm). The device geometry is then defined using reactive ion etching in a gas mixture of CHF_3:O_2:Ar, where the metal topgate and additional PMMA is used as an etch mask.

5. A bridge contact is made to the metal topgate by depositing cross-linked PMMA and then Cr:Au. The cross-linked PMMA avoids shorting to the exposed

graphene at the edges of the device.

6. Final edge contacts are made to the device by an additional reactive ion etch step and then subsequently evaporating Cr:Au contacts using the same PMMA mask. A rotation stage set at a 15 degree angle is used during the evaporation to make sure the metal properly coats the sidewalls of the device to ensure good 1d edge contact.

A.2 Contact Resistance Subtraction

A 2-probe measurement of quantum Hall edge states will include an extra resistance from the electrodes leading up to the measurement area of the device. We correct for this contact resistance by extracting the resistance offset of a conductance plateau from its expected quantized value, for example, by fitting the $\nu = -1$ plateau to $\frac{e^2}{h}$. We then take this contact resistance and subtract it from the entire measurement. The procedure is considered valid if a single contact resistance subtraction causes all other conductance plateaus to match an integer multiple of $\frac{e^2}{h}$ (see for example the data in panel (d) of Figure 3-1). We find that the contact resistance does change for positive and negative values of ν_{tot}, due to the formation of pn junctions at the electrode-graphene interface (more discussion below). As such, we perform separate contact resistance corrections for the negative and positive sides of a ν_{tot} sweep (this is the case for the data in panel (e) of Figure 3-1 and panel (d) of Figure 3-2 in section 3.4). At 4T, the device discussed in Figures 3-1-3-3 in section 3.4 has a contact resistance of 0.6 kΩ for negative ν_{tot} and 2.0 kΩ for positive ν_{tot}tot. Since the contact resistance effects for the helical $(\pm 1, \mp 1)$ are currently unknown, the measurement for the electron-hole bilayer configurations in panels (b) & (c) of Figure 3-2 in section 3.4 are presented in the raw uncorrected form.

A.3 Additional measurements of filling factor transitions

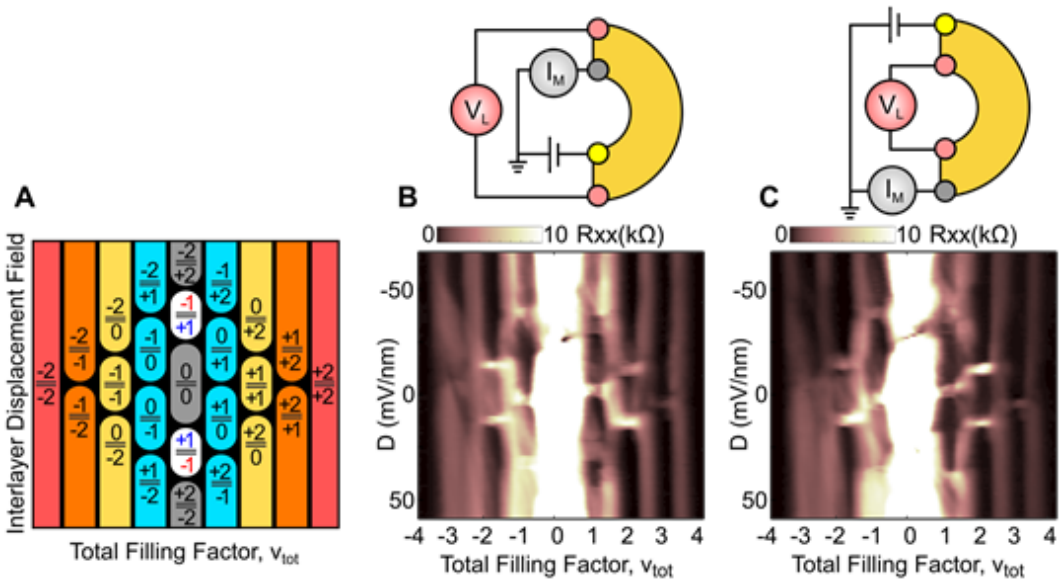

Figure A-1: 4-probe resistance maps show filling factor transitions. Data is for sample W presented in Fig. 3-1- 3-3 of section 3.4. Measurement is performed in two configurations (B) and (C), with the transitions matching the expected state sequence described in panel (e) of Fig 3-2 of section 3.4 (reproduced here) and matches the plateau transitions observed in the 2-probe conductance data. Measurement is at B = 4T.

A.4 Capacitance Measurements

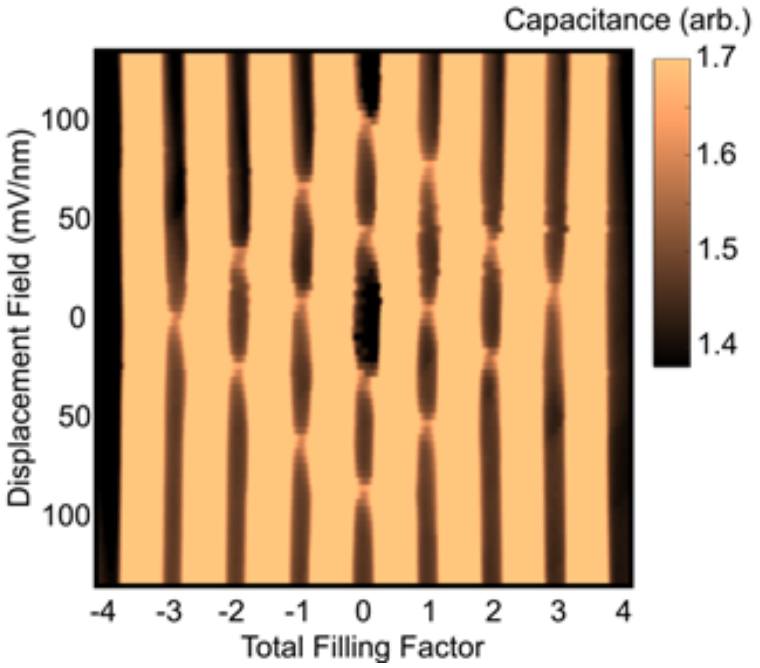

Figure A-2: Capacitance measurement on a twisted bilayer graphene device showing bulk state transitions (Sample O). Measurement signal is proportional to the device capacitance from the graphene bilayer to both gate electrodes. Low signal (black) corresponds to gapped/insulating states. High signal (orange) corresponds to high density of states/conductive states. Sequence of transitions matches 2-probe data and model presented in panels (d) and (e) of Figure 3-2 in section 3.4. Measurement is at $B = 18\text{T}$.

A.5 Temperature Dependence Measurements

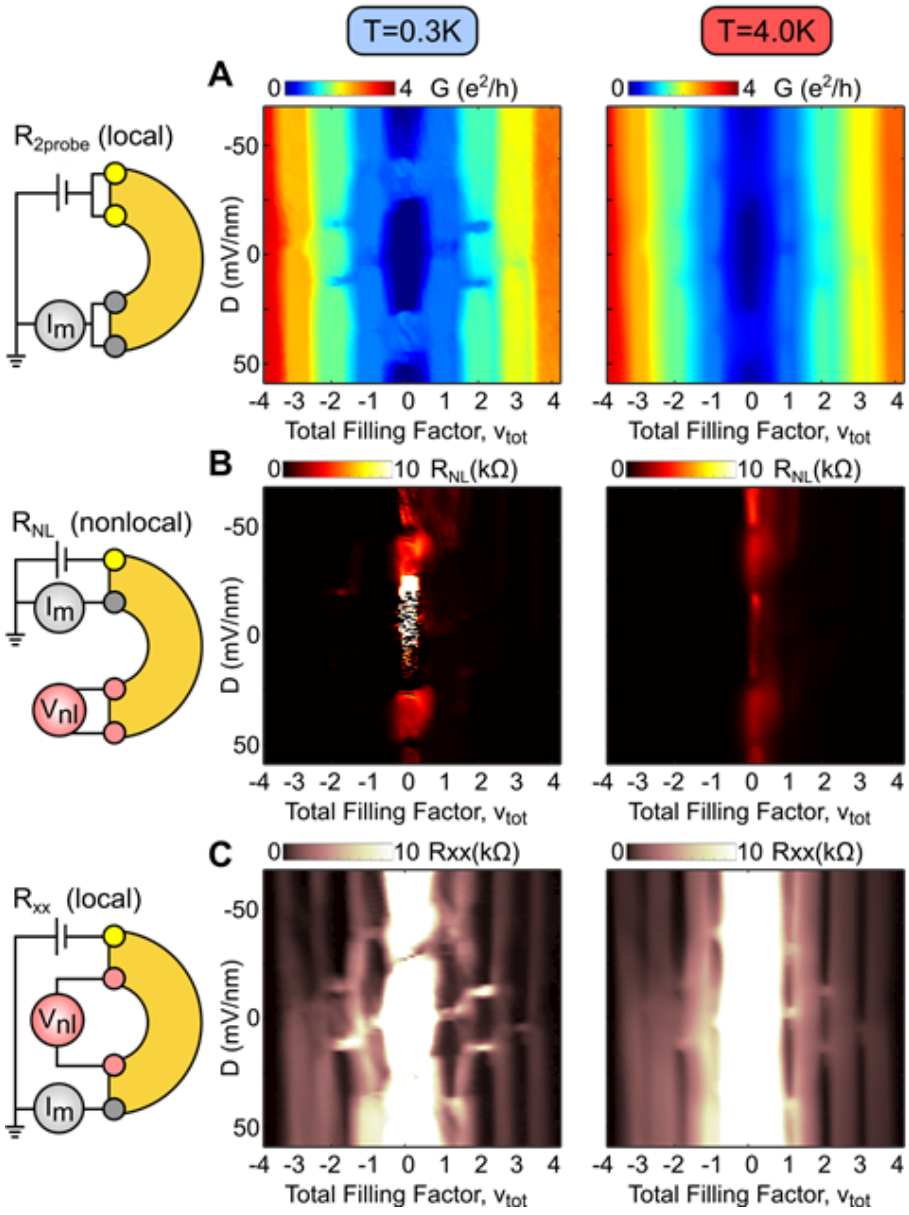

Figure A-3: Comparison of transport measurements at base (0.3 K) and elevated temperatures (4 K). Data is for sample W presented in Figures 3-1-3-3 of section 3.4. Columns from left to right correspond to 0.3 K and 4.0 K temperatures, respectively. Rows from top to bottom are the 2-probe conductance, nonlocal resistance, and local 4-probe resistance. Temperature causes a smooth broadening of all transport features.

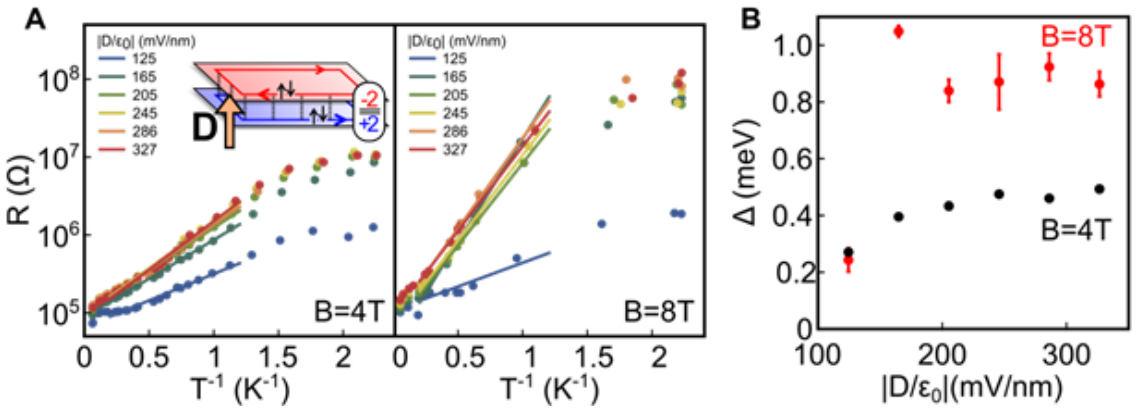

Figure A-4: Temperature dependence of the (+2,-2) insulating state at 4 T and 8 T shows an activated dependence, suggesting a full hybridization gap at the sample edge between the counter-propagating edge states. Data is for Sample W presented in Figures 3-1-3-3 of section 3.4. (A) 2-probe resistance as a function of inverse temperature for (+2,-2) state at 4 T and 8 T. Lines show fit to activated temperature dependence $R \sim R_0 e^{\frac{\Delta}{2k_B T}}$. (B) Extracted activated gaps as a function of displacement field.

The $(\pm 2, \mp 2)$ states are characterized by deep insulating behavior that increases with magnetic field. Figure A-4 shows the temperature dependence of the resistance in the (+2,-2) state at different electric and magnetic fields. The resistance shows an activated temperature dependence: $R\ R_0 e^{\frac{\Delta}{2k_B T}}$. The extracted activated gap increases with increased magnetic field (panel (b) of Figure A-4). The observation of thermally activated behavior suggests that a hybridization gap is developing between the counter-propagating $(\pm 2, \mp 2)$ edge states originating from interlayer tunneling at the edge.

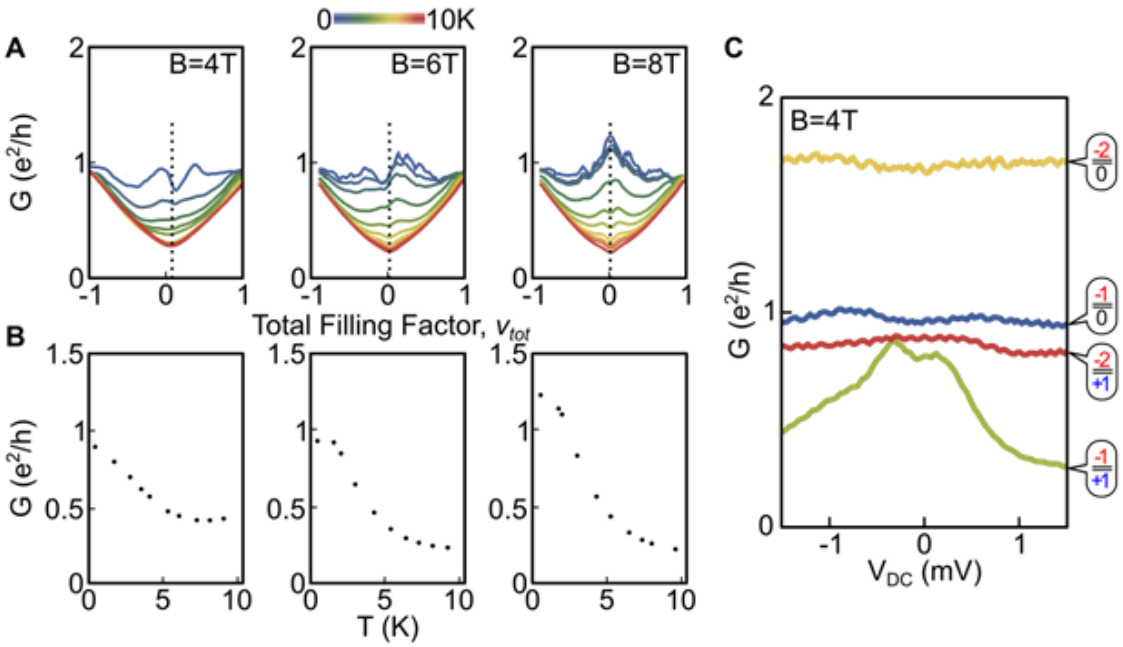

Figure A-5: Temperature and bias dependence of helical states. Data is for sample W presented in Figures 3-1-3-3 of section 3.4. (A) Conductance as a function of total filling factor at different temperatures (0.3 K to 10 K) and magnetic fields. (+1,-1) state is centered at total filling factor zero. (B) Conductance of the (+1,-1) state as a function of temperature. Data is taken from points intersecting the vertical dotted line in the top datasets. The conductance through the helical edge states increases with higher magnetic fields and lower temperatures. (C) DC voltage bias dependence of differential conductance for different filling factor configurations. All measurements show a flat bias dependence except the helical (+1,-1) state, which shows an overall decrease in differential conductance with increasing voltage bias.

A.6 (+1,-1) Measurements in Different Devices

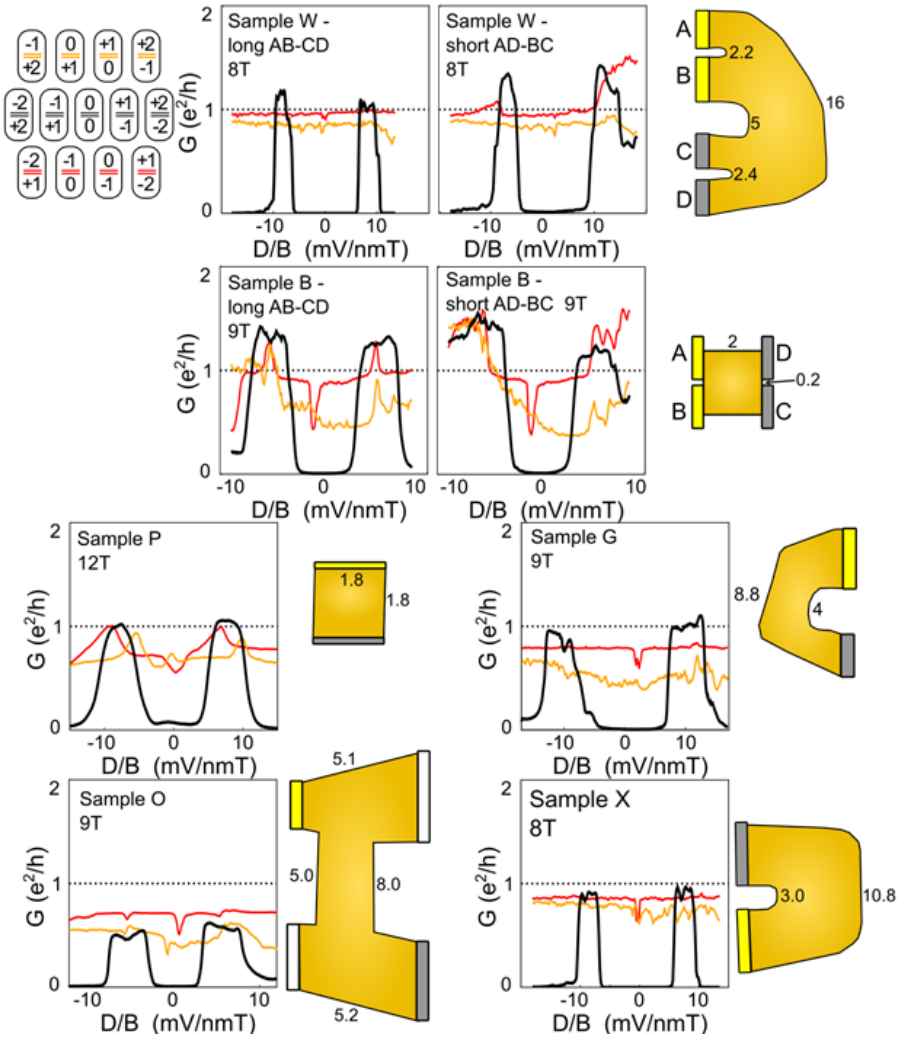

Figure A-6: Raw conductance of the $\nu_{tot} = 0$ line for different devices showing conductive $(\pm 1, \mp 1)$ states (no contact resistance correction). Conductance, G, is plotted as a function of the displacement field divided by the magnetic field, since the displacement value for the transitions scales roughly linearly with magnetic field. Conductance at $\nu_{tot} = 0$ (black lines) is compared to the conductance at $\nu_{tot} = -1$ (red lines) and $\nu_{tot} = +1$ (yellow lines). The observed states are given by the filling factor configurations in the top left corner. Cartoons depict outline of sample geometry, with edge lengths given in units of microns. Data for section 3.4 came from sample W. Note that the conductance of the $\nu_{tot} = +1$ states (yellow lines) is consistently smaller than the $\nu_{tot} = -1$ states (red lines) due to asymmetry in the contact resistances for negative and positive ν_{tot}.

A.7 4-probe Resistance Measurements of Helical Edge States

If backscattering is possible between the helical edge states and spatially homogeneous, then we expect that the edge resistance will scale linearly with the edge length. In this case, it follows straightforwardly that the 4-probe resistance measurement will depend on the edge lengths as $R_{4probe} \propto L_{SD}L_V/\sum L_i$, where L_{SD} and L_V are the edge lengths between the source-drain electrodes and voltage probes, respectively, and $\sum L_i$ is the sum of the edge lengths between contacts. In this situation of diffusive edge conductance, we would expect that the R_{xx} measurement discussed in section 3.4 would be 15.2 times greater than the R_{NL} measurement, which is very close to the measured ratio at $B = 1.5$T. But, as the magnetic field increases, the measurements converge, indicating a length-independent edge resistance.

In the absence of backscattering, a pair of helical edge states will act a ballistic 1d wire running along the edge of the sample. As is typical for 1d conductors, invasive contacts can interrupt the edge state by causing equilibration between the forward and backward moving modes. In this case, each edge segment between contacts will have a length-independent resistance of h/e^2. In a device with 4 contacts, a longitudinal resistance measurement (such as the R_{NL} and R_{xx} configuration discussed in section 3.4) will give a value of $h/(4e^2)$ since 1/4 of the current flows through the quantum resistor between the two voltage probes. This is the value that the R_{xx} and R_{NL} measurements converge to with increasing magnetic field (panel (e) of Figure 3-3).

A.8 Low Magnetic Field Measurements

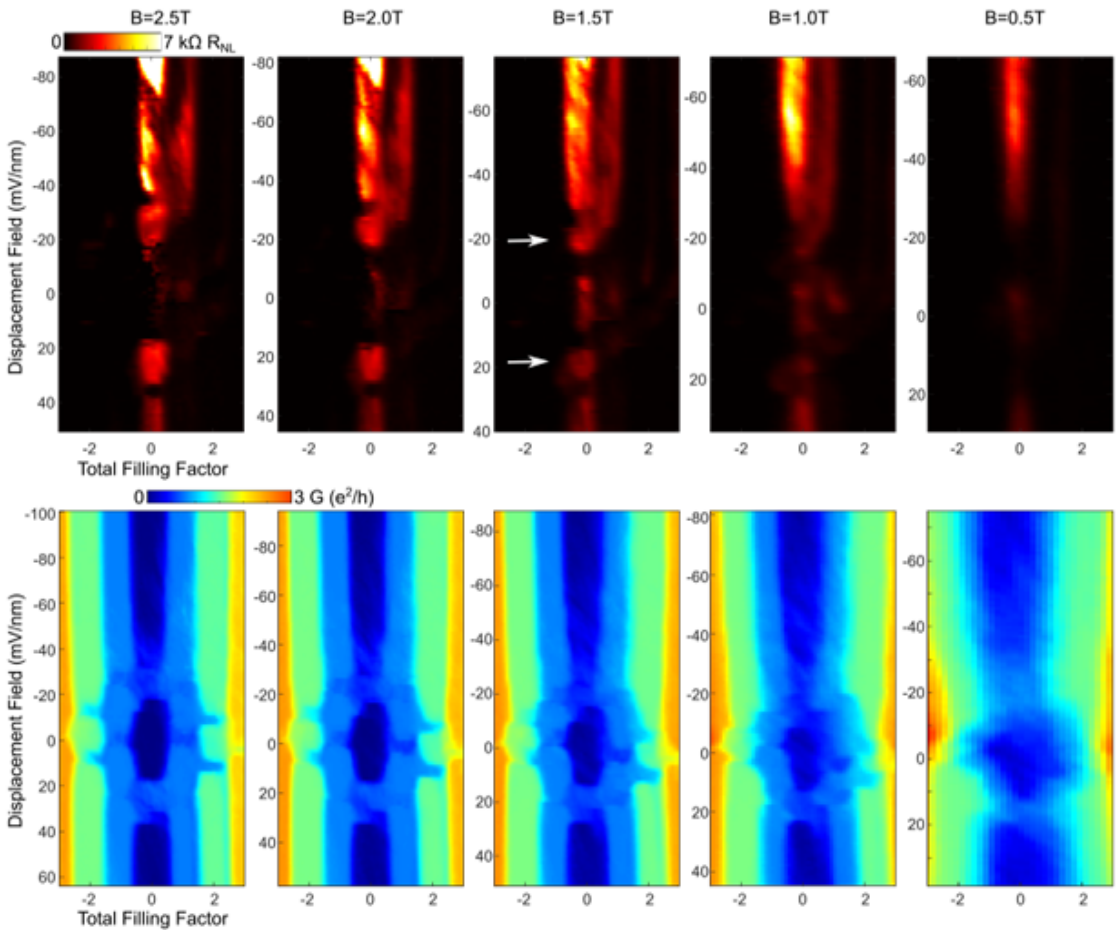

Figure A-7: Onset of helical edge states at low magnetic fields. Data is for sample W presented in Figures 3-1-3-3 of section 3.4. Color plots show the low magnetic field development of the nonlocal resistance (top) and the 2-probe conductance (bottom), as a function of displacement field and total filling factor. At $B = 1.5$T, distinct nonlocal features can be seen $(\pm 1, \mp 1)$. At the same magnetic field, clearly defined plateaus in conductance can be seen originating from the $(\pm 2, \mp 2)$, $(0, \mp 2)$, $(\pm 1, 0)$ states. The data indicates well developed broken symmetry states and helical edge states at this low magnetic field.

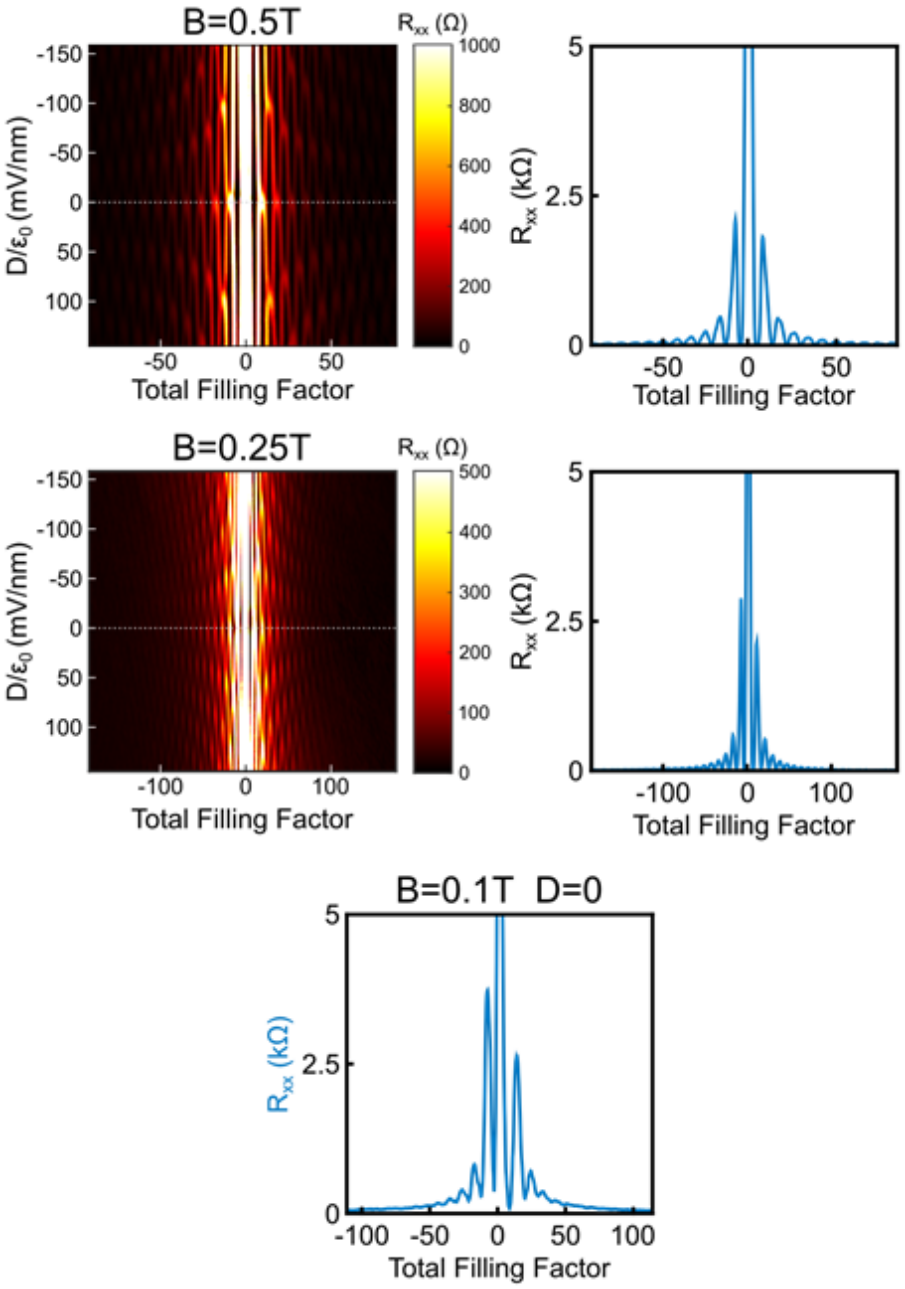

Figure A-8: Magnetoresistance at low magnetic fields consisting of 4-probe longitudinal resistance measurements for device W discussed in Figures 3-1-3-3. R_{xx} peaks show Landau level crossing structure characteristic of twisted bilayer graphene devices [82]. The well-developed R_{xx} minima at such low magnetic fields highlight the high quality of this device.

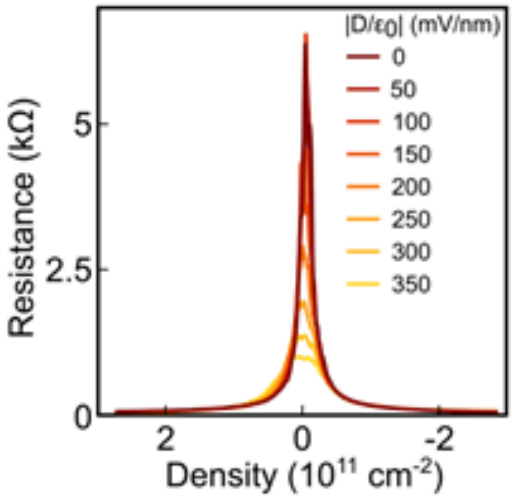

Figure A-9: 4-probe resistance at zero magnetic field as a function of total density and displacement field. At zero magnetic field, interlayer displacement field causes the charge-neutrality point resistance to decrease. The resistance at the charge neutrality point steadily decreases with displacement field [82]. This behavior is in contrast to AB-bilayer graphene, where the effect of a displacement field is to open up a bandgap at the Dirac point [121], leading to a diverging resistance [122]. The measurement is performed at 0.3 K.

THIS PAGE INTENTIONALLY LEFT BLANK

Appendix B

Supplementary Information for Superlattice-Induced Insulating States and Valley-Protected Orbits in Twisted Bilayer Graphene

B.1 Sample Fabrication

Our samples are prepared with a modified dry-transfer method, and a 'tear & stack' technique is used to control the twist angle in twisted bilayer graphene (TwBLG). Monolayer graphene flakes and hexagonal boron nitride (h-BN) flakes are first exfoliated on Si chips with 285 nm of SiO_2. The exfoliated chips are examined under a Zeiss optical microscope and the positions of monolayer graphene flakes larger than 30 µm in one dimension and h-BN flakes with thickness between 10∼40 nm and larger than 50 µm are recorded. Graphene flakes with relatively large length/width ratio are preferred because it facilitates the tearing process.

Using a home-built micro-manipulation stage, we first pick up a piece of h-BN with a PC [Poly (Bisphenol-A Carbonate)] / PDMS (Polydimethylsiloxane) stack on a glass slide at 90 °C. We then bring the h-BN into contact with only one half of

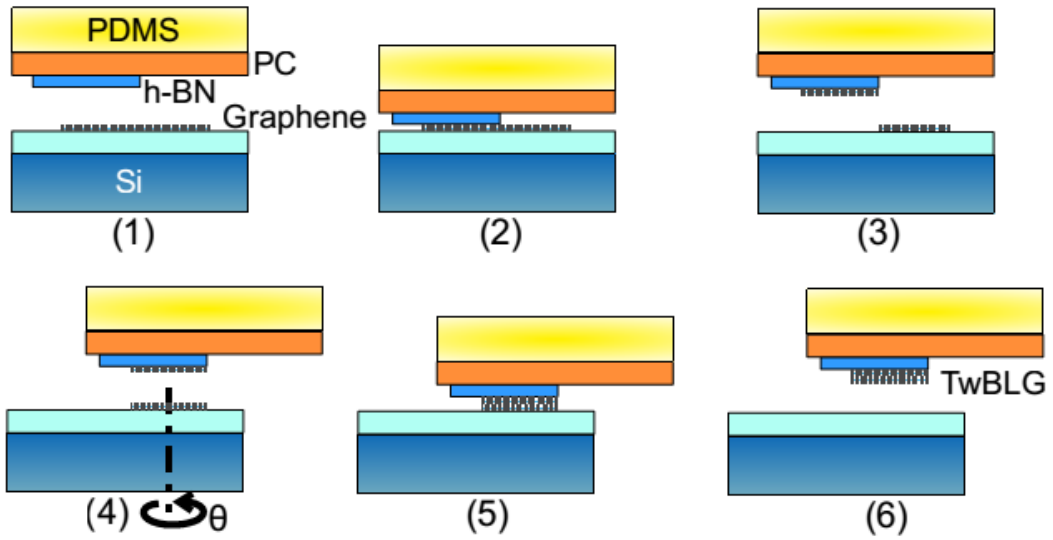

Figure B-1: Illustration of the "tear-and-stack" method.

a target graphene flake. The van der Waals force pins one half of the graphene to the h-BN flake, while the substrate holds onto the other half. Lifting up the van der Waals-bonded half forces the graphene to tear at the edge of the hBN. When the graphene is successfully separated, we rotate the chip bearing the remaining graphene by angle θ. The remaining graphene is picked up whilst maintaining the orientation, overlapping part of the first half that is already in contact with the h-BN. At this point, the twist angle is set by the angle θ. Finally we pick up an h-BN flake as the bottom layer and release the entire stack onto a metal gate. An example of the resulting stack is shown in Fig. B-2. A similar method is independently developed in Ref. [123].

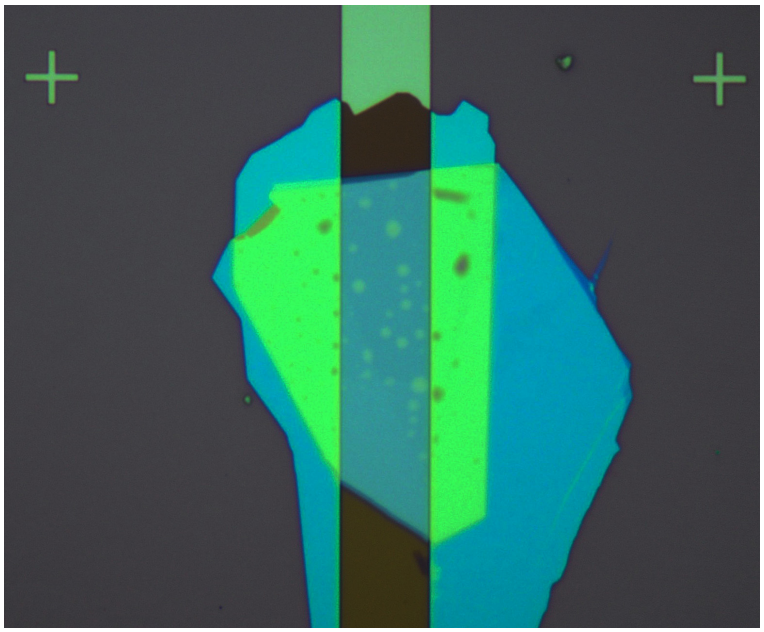

Figure B-2: A TwBLG stack on a metallic back gate.

After the stack is made, we first characterize it with atomic force microscopy (AFM) to find bubble-free regions and Raman spectroscopy to qualify the twist angle. We then use electron-beam lithography (EBL) and reactive ion etching (RIE) to fabricate the top gate, edge-contact the TwBLG, and define the geometry of the sample. First, we use EBL on a 950A5 PMMA mask to define the top gate. 30$\sim$40 nm of Au or Pd/Au is evaporated and lifted off as the top gate. Then, we write a second PMMA mask as an etch mask with EBL. An $Ar/CHF_3/O_2$ etching recipe is used to define the Hall bar geometry of the device. Finally, we write a third PMMA mask to define the geometry of the electrode leads. The device is first RIE-etched with this mask to expose the edges of the TwBLG, and metal (Au or Pd/Au) is then immediately evaporated and lifted off using the same mask. The contact resistance of these edge contacts is usually a few hundred ohms (a few kilo-ohms in the worst case).

We use the Elionix F-125 EBL system with 125 kV acceleration voltage in Microsystems Technology Laboratories (MTL) at MIT and STS ICP RIE (RIE-8) at Center for Nanoscale Systems (CNS), Harvard University.

B.2 Device Characterization

B.2.1 Atomic Force Microscopy (AFM)

We use AFM to characterize the flatness of the device. After dry-transferring and removing the PC from the sample, we scan the top surface of the device with tapping mode AFM to find regions that are free of bubbles and wrinkles. Fig. B-3(a) shows the AFM image of device S1 before patterning into a Hall bar. It can be seen that the Hall bar is atomically flat despite the bubbles in other regions of the device.

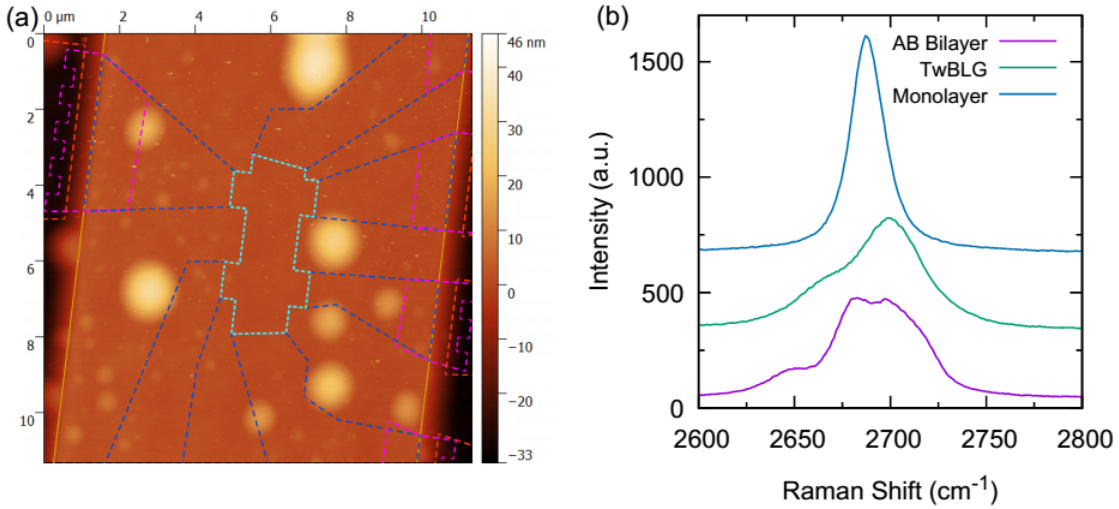

Figure B-3: (a) AFM image of device S1. The light blue dashed lines outline the device region that was fabricated into a Hall bar, which is free of bubbles and wrinkles. The length/width of the Hall bar region is 2.5 µm/1.5 µm. (b) 2D peak of the Raman spectrum of AB bilayer graphene, a TwBLG with small twist, and monolayer graphene.

B.2.2 Raman Spectrum

It is reported in Ref. [124] that the Raman spectrum of TwBLG is sensitive to its twist angle, especially the 2D peak centered around $2680\,\mathrm{cm}^{-1}$. We use the shape of the 2D peak to qualitatively differentiate between large twist angle and small twist angle TwBLG. Fig. B-3(b) shows the 2D Raman peak of AB bilayer graphene, a small twist TwBLG, and monolayer graphene. Small twist TwBLG has a 2D peak that is much broader than the monolayer peak and usually has an additional shoulder. On the other hand, large twist TwBLG has a spectrum very similar to monolayer graphene due to the decoupled Dirac cones for its low energy band structure. Currently we do not have enough calibration and data resolution to precisely determine the twist angle of a particular sample, and this method serves more of a qualitative purpose.

B.3 Theoretical Calculations

B.3.1 Band Structure

S.F. and E.K. performed *ab initio* tight-binding calculations of the $\theta = 1.79°$ commensurate TwBLG structure. In this calculation, a Wannier transformation is performed based on the density functional theory calculation with the exchange-correlation functional of Perdew, Burke, and Ernzerhof (PBE) type [125]. The tight-binding hopping parameters are extracted between p_z orbitals in the bilayer graphene and generalized to generic graphene stacks with arbitrary translations and twist angles. The form of the interlayer hoppings depends on both the interlayer pair distance and orientation with respect to their underlying monolayer crystals. The *ab initio* tight-binding Hamiltonian in our calculations has intralayer hopping terms up to eight nearest neighbors, and interlayer coupling terms with planar cutoff distance of 4.9 Å. See Ref. [106] for more details.

B.3.2 Valley Polarization

The valley polarization of the eigenstates, as shown in section 4.4 Fig. 4-5 and panels (c)-(f) of Fig. 4-7, are evaluated by projecting the eigenstates onto the plane wave basis in each layer.

In the superlattice with unit cell vectors $\vec{b}_1$ and $\vec{b}_2$, a Bloch state $\psi_{\vec{\tilde{k}}}$ with momentum $\vec{\tilde{k}}$ satisfies the Bloch equation $\tilde{T}(\vec{b}_i)\psi_{\vec{\tilde{k}}} = e^{-i\vec{\tilde{k}}\cdot\vec{b}_i}\psi_{\vec{\tilde{k}}}$ under translation operators $\tilde{T}$ for the superlattice. However, $\psi_{\vec{\tilde{k}}}$ can be further decomposed under the group representations for the translation operators of the smaller original unit cells. $\psi_{\vec{\tilde{k}}} = \sum_{\vec{G}} \phi^{\vec{\tilde{k}}}_{\vec{G}}$ where $\vec{G}$ is the superlattice reciprocal lattice vector and $T(\vec{v}_i)\phi^{\vec{\tilde{k}}}_{\vec{G}} = e^{-i(\vec{\tilde{k}}+\vec{G})\cdot\vec{v}_i}\phi^{\vec{\tilde{k}}}_{\vec{G}}$, where $\vec{v}_i$ are unit cell vectors of either graphene layer. The $\phi^{\vec{\tilde{k}}}_{\vec{G}}$ is the projected Bloch component at momentum $\vec{\tilde{k}} + \vec{G}$ in the monolayer Brillouin zone. To project out the Bloch wavefunction characters, we compute the norm $|\phi^{\vec{\tilde{k}}}_{\vec{G}}| \sim |\sum_{\vec{r}_i} e^{-i(\vec{\tilde{k}}+\vec{G})\cdot\vec{r}_i}\psi_{\vec{\tilde{k}}}(\vec{r}_i)|$ for the relevant $\vec{\tilde{k}}$ and bands $\psi_{\vec{\tilde{k}}}(\vec{r}_i)$. $\vec{r}_i$ are the positions for basis sites in either layer of the superlattice. The results show dominant components for $\vec{\tilde{k}} + \vec{G}$ in only one of the valleys, either K or K' of the monolayer Brillouin zone. Because of the existence of a tiny intervalley hopping probability, the valley polarization is not 100 %, but the probability of being in one valley is always more than 1 order of magnitude larger than being in the other valley for the $\theta = 1.79°$ superlattice.

B.3.3 Angular Dependence

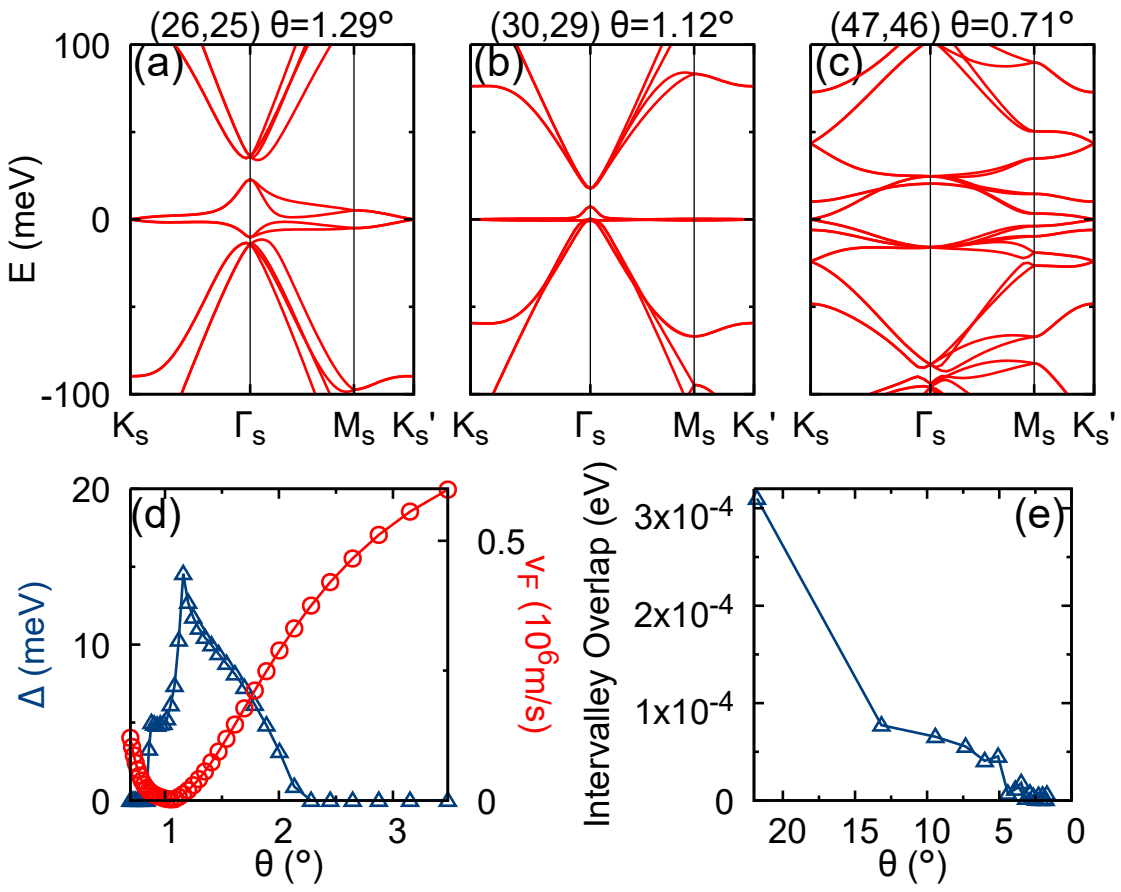

Figure B-4: (a-c) Band structure calculations for $\theta = 1.29°$, $1.12°$ and $0.71°$. (d) The global energy gap and the Fermi velocity obtained from the band structures of different twist angles. (e) The intervalley overlap matrix element for different twist angles.

It is shown in various literature and our calculation that the Fermi velocity in a TwBLG does not drop monotonically with decreasing twist angle. It actually reaches zero at a non-zero twist angle θ_0, which varies from $1.0{\sim}1.5°$ in literature [101, 105]. Below this angle, the topology of the low-energy bands changes qualitatively and the Fermi velocity increases again.

The size of the superlattice gap at Γ_s is also non-monotonic with the twist angle. Above θ_0, the gap size generally increase with decreasing twist angle. At extremely low twist angles below θ_0 however, the gap vanishes again. Fig. B-4 shows the band

structure calculated for $\theta = 1.29°$, $1.12°$ and $0.71°$ with an *ab initio* tight-binding model. The critical angle θ_0 is $1.1°$ from the calculation, and the gap vanishes at about $0.84°$.

We can also calculate the overlap matrix element of the interlayer coupling between eigenstates from opposite valleys for different twist angles. The result is shown in panel (e) of Fig. B-4. As expected, the matrix element drops quickly as the twist angle decreases due to the decreased magnitude of the MBZ reciprocal lattice vector. Therefore for twist angles $< 5°$the interlayer coupling do not mix the valleys effectively.

B.3.4 Electric Field Effect

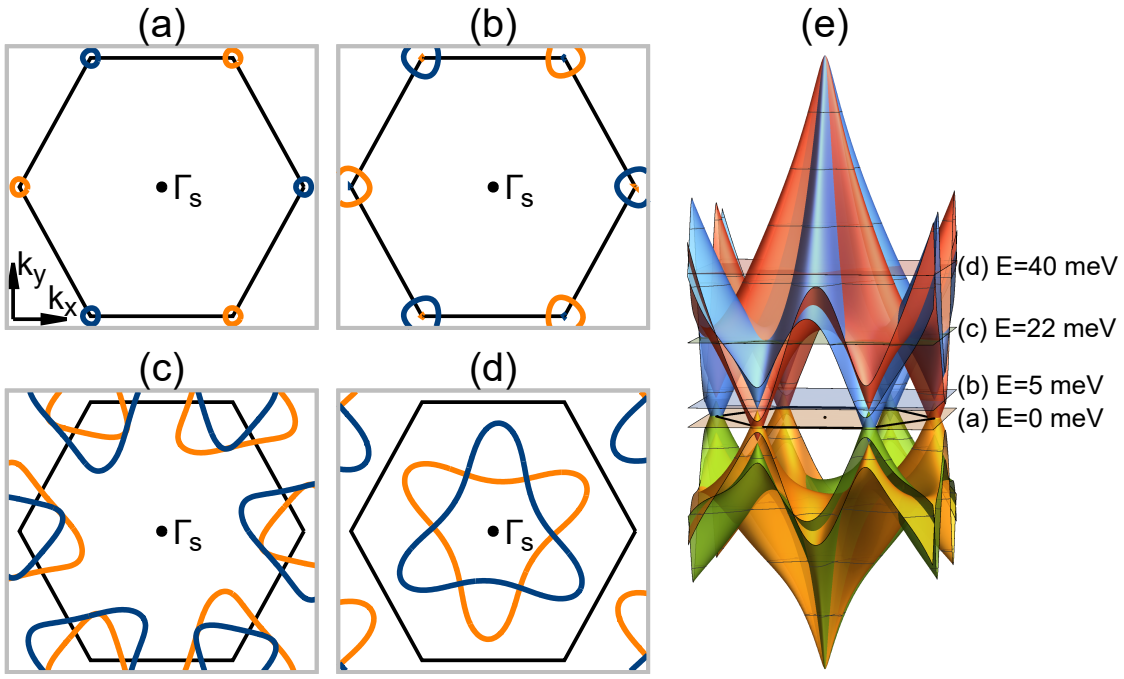

Figure B-5: (a-d) Fermi contours of a $\theta = 1.8°$ TwBLG with interlayer potential difference $\Delta V = 0.1\,\text{eV}$ at four different energies labeled in (e) the 3D plot of the band structure. Orange contours are K-polarized and blue contours are K'-polarized. In (a), each Fermi pocket is actually doubly degenerate. In (b), at each corner of the MBZ one of the Dirac cones has retracted to a single point.

By introducing a diagonal interlayer potential, we can simulate the effect of an electric field on the TwBLG. Fig. B-5 shows the calculated band structure and Fermi contours of a $\theta = 1.79°$ TwBLG with $\Delta V = 0.1\,\text{eV}$ potential difference between the two layers. The valley polarization arguments are still valid with the potential difference. Because of ΔV, the Dirac cones at $K^{(1)}$ and $K'^{(1)}$ are separated from the cones at $K^{(2)}$ and $K'^{(2)}$ in energy. However the separation is much less than ΔV for small angle TwBLG, an effect which is discussed in Ref. [126] and attributed to interlayer band mixing at the Dirac points. At finite energies where the bands are still approximately Dirac-like [panels (b) & (c) of Fig. B-5], we observe Fermi contours with different sizes due to the energy separation. However at higher energies near the superlattice band edge [panel (d) of Fig. B-5], the areas of the two Fermi contours remain identical. Therefore an electric field does not lift the degeneracy near the band

edge. The experimental observation of this effect is discussed later in this appendix.

B.4 Insulating States/Conductance Minima

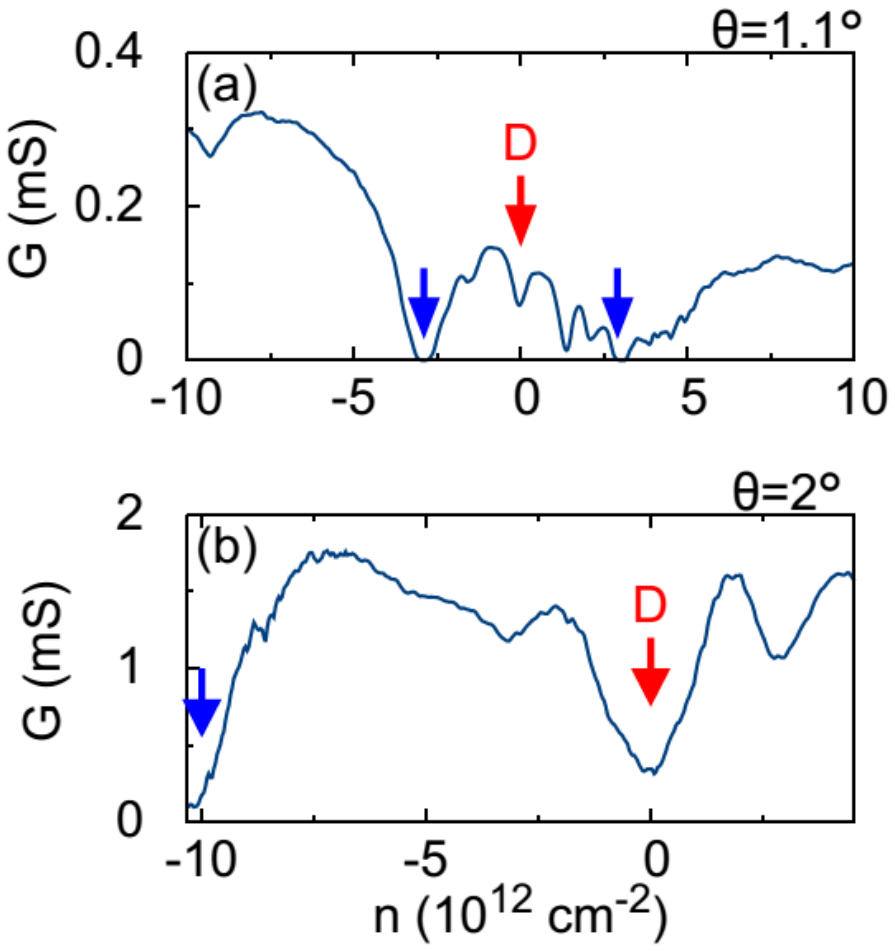

Figure B-6: The conductance G of device (a) S2 with $\theta = 1.1°$ and (b) S3 with $\theta = 2°$. Red arrows indicate the Dirac points. Blue arrows indicate the insulating states in S2 and the conductance minimum in S3.

We have observed insulating states/conductance minima associated with filled superlattice bands in three different samples. Apart from the $\theta = 1.8°$ device S1 extensively discussed in the main text, devices S2 with $\theta = 1.1°$ clearly shows a pair of insulating states and S3 with $\theta \approx 2°$ show a similar conductance minimum which is more insulating that the Dirac point. Their conductance as a function of gate voltage is shown

in Fig. B-6.

At zero magnetic field, while the resistance of device S1 reaches a maximum of 250 kΩ, the resistance of device S2 and S3 it reaches 10 MΩ and 5 kΩ respectively. The relative low resistance of S3 can be attributed to its higher twist angle and thus closing of the gap. The trend of increasing resistance for the superlattice gap states with decreasing twist angles agrees with the trend of increasing gap size with decreasing twist angle in this range (panel (e) of Fig. 4-7).

B.5 Temperature Dependence

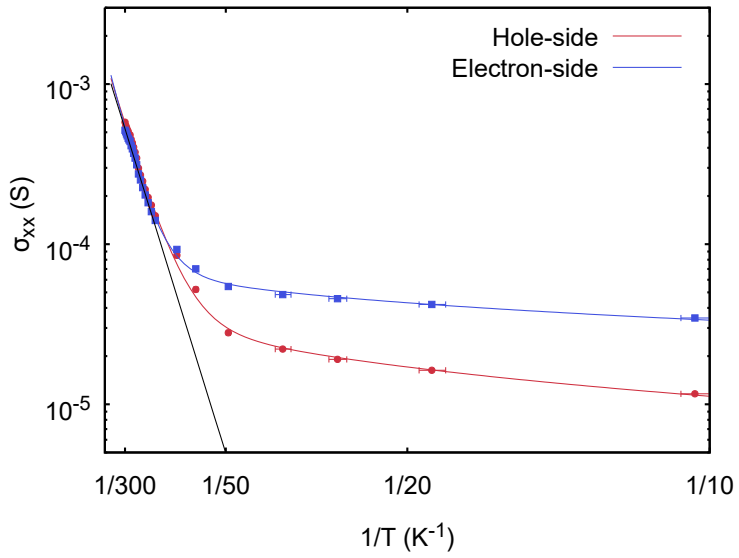

Figure B-7: Temperature dependence of the insulating states in device S1, from 10 K to 300 K.

The saturation of the conductivity of the insulating states at low temperatures indicates an alternative conduction mechanism to thermal activation, such as variable-range hopping (VRH). Assuming the VRH to be of Mott-type [111], we would expect the low temperature conductivity to be proportional to $\exp\left[-(T_0/T)^{1/3}\right]$. Therefore we fit the conductivity in the entire temperature range with a double exponential of

the form

$$\sigma = Ae^{-\frac{\Delta}{2kT}} + Be^{-\left(\frac{T_0}{T}\right)^{1/3}}. \tag{B.1}$$

This is shown in Fig. B-7. The parameters are fitted to be

$$\text{Hole side: } \Delta_- = (50 \pm 3)\,\text{meV}, T_{0-} = 18\,\text{K} \tag{B.2}$$

$$\text{Electron side: } \Delta_+ = (60 \pm 4)\,\text{meV}, T_{0+} = 86\,\text{K}. \tag{B.3}$$

. The uncertainty correspond to 2 standard errors in the value of Δ obtained from the least-squares fitting procedure. The good fit with Eq.(B.1) shows the viability of the Mott VRH mechanism. However we cannot rule out the possibilities of other possible VRH mechanisms at low temperatures, such as Efros-Shklovskii VRH which has $T^{-1/2}$ instead in the exponent.

B.6 Electric Field Dependence

We have studied the effect of applying a differential gate voltage to our TwBLG sample with $\theta = 1.8°$. By adding a perpendicular electric field E to the TwBLG, we can tune the interlayer potential difference which effectively sets the relative energy difference between the original Dirac cones of the two layers.

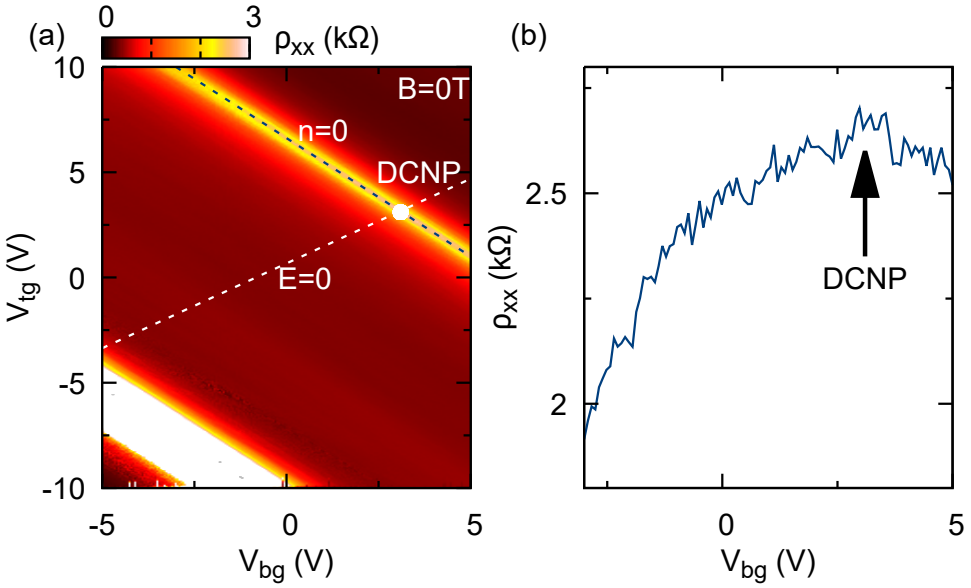

Figure B-8: (a) The resistivity of device S1 as a function of both top and bottom gate voltages at zero magnetic field. The upper peak in resistivity corresponds to the Dirac point, which occurs at $n = 0$. The lower peak corresponds to the hole side insulating state. Dashed lines correspond to zero electric field $E = 0$ and zero density $n = 0$. The double charge neutrality point (DCNP) where $n = E = 0$ is marked with a white dot. (b) The resistivity along the $n = 0$ line in (a).

Fig. B-8 shows the resistivity of device S1 versus the top gate voltage $V_{\rm tg}$ and back gate voltage $V_{\rm bg}$. The double charge neutrality point (DCNP) is where the carrier densities on both graphene layers are independently equal to zero. By applying a differential gate voltage from the DCNP, it remains at the total carrier density $n = n_t + n_b = 0$ but with $n_t = -n_b \neq 0$. In this case we observed a moderate *decrease* in resistivity at higher interlayer electric field E, in contrast to AB bilayer graphene where the resistivity increases with increasing E [127–129]. This effect can be understood assuming the low energy band structure to be two Dirac cones

which has a tunable energy difference by the interlayer electric field (see Fig. B-5). When $E \neq 0$, the minimum DOS does not drop to zero at charge neutrality point as opposed to two degenerate Dirac cones when $E = 0$, therefore reducing the maximal resistivity.

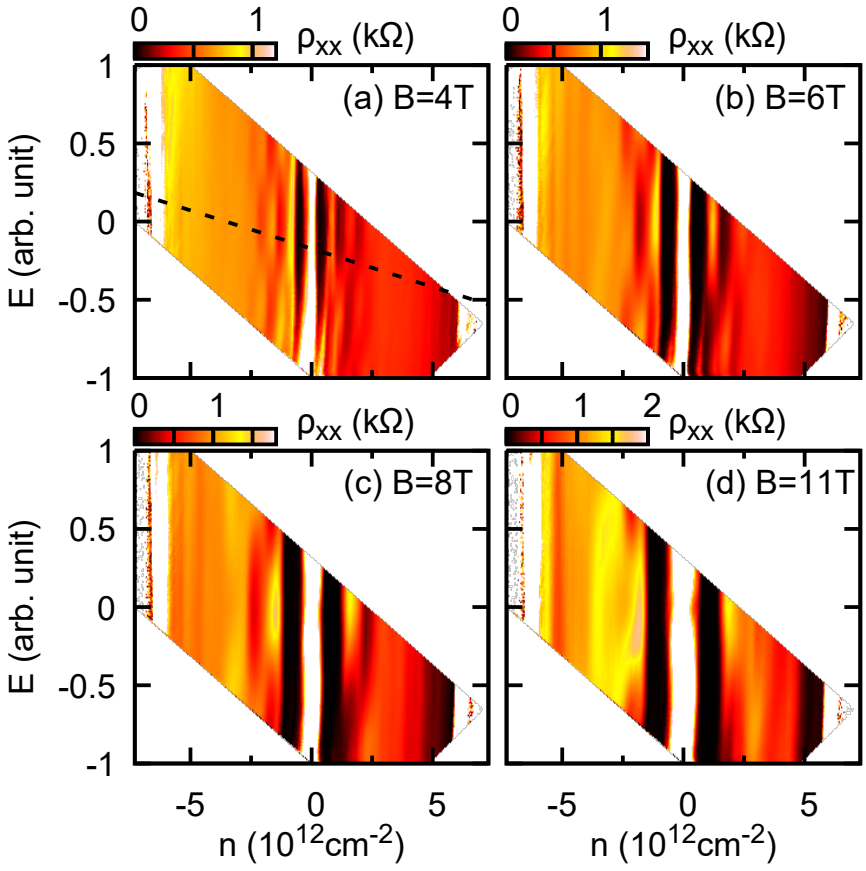

Figure B-9: Electrical field dependence of the Landau levels. The black dashed line indicates the line along which the main text Fig. 3 was measured. The conversion from gate voltages to n and E is given by $n = 0.54V_{\rm tg} + 0.49V_{\rm bg} - 2.6, E = 0.070V_{\rm tg} - 0.056V_{\rm bg} - 0.047$, where n is in unit of $10^{12}{\rm cm}^{-2}$ and $V_{\rm bg,tg}$ are in volts. E is in an arbitrary unit.

An electric field may induce Landau level crossings of the two graphene layers in a magnetic field [82]. Fig. B-9 shows the resistivity maps at different magnetic fields. The gate voltages are converted to total carrier density n and interlayer electric field E. We see that compared with $E = 0$ line, at large enough E the quantum Hall

sequence shifts from $\pm 4, \pm 12, \pm 20, \ldots$ to $0, \pm 8, \pm 16, \ldots$. This sequence is indicative of different filling factors in the two layers when an electric field is present. For example, $\nu_{\mathrm{tot}} = 0$ results from $\nu_{\mathrm{bot}} = -2$ and $\nu_{\mathrm{top}} = 2$; $\nu_{\mathrm{tot}} = 8$ results from $\nu_{\mathrm{bot}} = 2$ and $\nu_{\mathrm{top}} = 6$, *etc.*

In the magnetotransport study in the main text, we swept the gate voltages along the dashed line shown in Fig. B-9(a) at each magnetic field. We do not scan along a constant E line due to limitations in the gate voltage; thus a small amount of electric field is present at all points in the sweep. As a result in the Landau fan diagram (main text Fig. 3) we see faint traces of $\pm 8, \pm 16$ plateaus near the Dirac point. However near the insulating states the features are not strongly dependent on E in contrast to states near the Dirac point (*e.g.* no Landau level crossings), which is consistent with theoretical calculations (see Fig. B-5). Therefore, the massive non-Dirac quantum Hall sequence discussed in this Letter remains valid.

B.7 Extraction of Cyclotron Mass

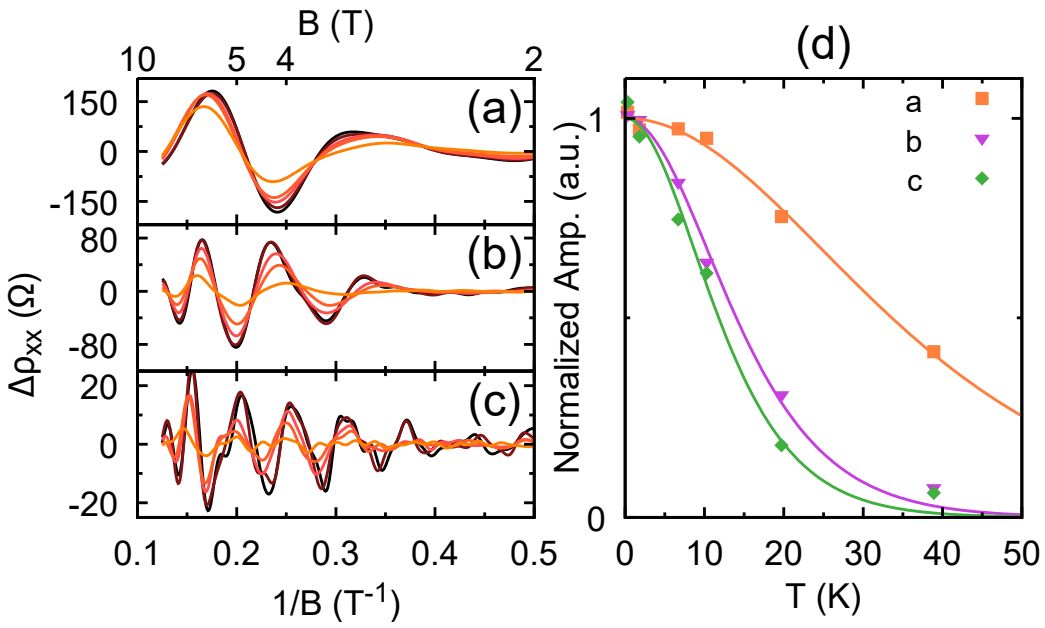

Figure B-10: (a-c) Examples of filtered SdH oscillations. From black to orange the temperature increases from 0.3 K to 40 K. (d) Fit of the temperature dependence of the normalized oscillation amplitudes of (a-c) to the Lifshitz-Kosevich formula.

We performed magnetotransport measurements from 0.3 K to 40 K. The SdH oscillation at each gate voltage is extracted and filtered, where high frequency noise and a polynomial background are removed. Temperature dependence of the most prominent peak is fitted with the Lifshitz-Kosevich formula

$$\Delta\rho_{xx} = \rho_0 \frac{\chi}{\sinh(\chi)}, \quad \chi = \frac{2\pi^2 kTm^*}{\hbar eB}, \tag{B.4}$$

and the cyclotron mass m^* is extracted from the fitting. Examples of the SdH oscillations and their temperature dependences are shown in Fig. B-10.

B.8 Phase Shift of Landau Fan Diagram

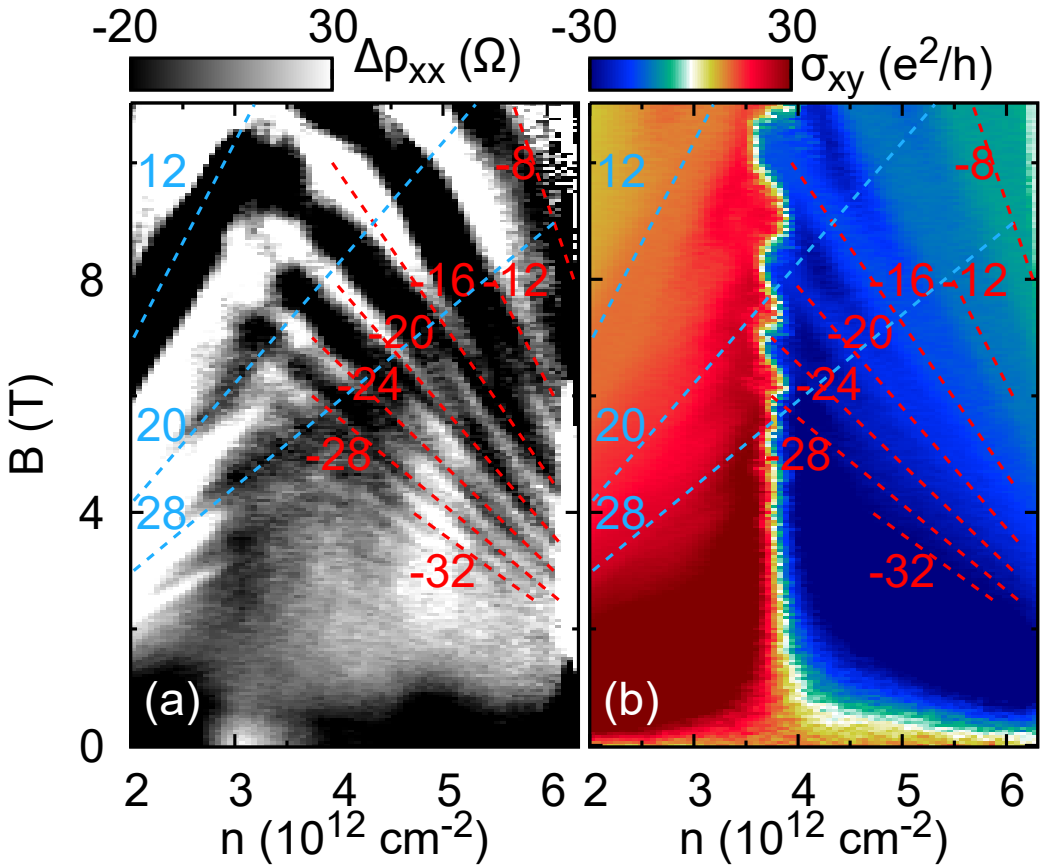

Figure B-11: (a) Longitudinal resistivity (background removed) and (b) Hall conductivity of device S1, zoomed in near the electron side insulating state. In (a), each ρ_{xx} minimum that corresponds to a fully filled Landau level (dashed lines) transitions to a maximum at high field $B > 5\,\mathrm{T}$. Light blue lines are part of the main Landau fan and the red lines are part of the secondary Landau fan on the electron side.

In addition to the magnetotransport features that are discussed in the main text, we report an additional phase shift of ρ_{xx} minima/maxima observed near the electron side insulating state. This effect become obvious only after polynomial background is removed from the raw data, and is shown in Fig. B-11. At lower fields $B < 5\,\mathrm{T}$, the minima of ρ_{xx} follow straight lines $B = (n - n_{0+})\phi_0/\nu$, where n_{0+} is the density at which the electron side insulating state occurs and $\nu = -4, -8, -12, \ldots$ are the filling factors. Above approximately 5 T, however, we observe a transition from ρ_{xx} minima to maxima and *vice versa* for each Landau level emanating from the insulating state.

This transition does not appear to manifest itself in the Hall conductivity map σ_{xy}.

This phenomenon is observed in only one device S1 so far and currently lacks a well-developed understanding. In a recent paper Ref. [130] a similar shift is observed in TwBLG but at the main Landau fan of the Dirac point. A proposed explanation is that the Landau levels from the main Landau fan can interfere with each level in the secondary Landau fan and switch the polarity of its induced change in ρ_{xx} due to many-body interactions. This effect may be significant only for small filling factors of the main Landau fan, *i.e.* only at relatively high fields where Landau levels with small filling factors intersect with the secondary fan.

Bibliography

[1] K. S. Novoselov, A. K. Geim, S. V. Morozov, D. Jiang, Y. Zhang, S. V. Dubonos, I. V. Grigorieva, A. A. Firsov. Electric Field Effect in Atomically Thin Carbon Films. Science **306**,666 (2004).

[2] A.H. Castro Neto, F. Guinea, N.M.R. Peres, K.S. Novoselov, A.K. Geim. The Electronic Properties of Graphene. Review of Modern Physics, **81**, 109 (2009).

[3] K. v. Klitzing, G. Dorda, and M. Pepper. New Method for High-Accuracy Determination of the Fine-Structure Constant Based on Quantized Hall Resistance. Phys. Rev. Lett. **45**, 494âĂŞ497 (1980).

[4] D. C. Tsui, H. L. Stormer, and A. C. Gossard. Two-dimensional magnetotransport in the extreme quantum limit. Phys. Rev. Lett., **48**, 1559âĂŞ1562 (1982).

[5] Berger, C. et al. Ultrathin epitaxial graphite: 2D electron gas properties and a route toward graphene-based nanoelectronics. J. Phys. Chem. B **108**, 19912âĂŞ19916 (2004).

[6] Berger, C. et al. Electronic confinement and coherence in patterned epitaxial graphene. Science **312**, 1191âĂŞ1196 (2006).

[7] K.R. Paton et al. Scalable production of large quantities of defect-free few-layer graphene by shear exfoliation in liquids. Nature Materials, **13**, 624-630 (2014).

[8] X. Liu et al. Shear Modulus of Monolayer Graphene Prepared by Chemical Vapor Deposition. Nano Lett. **12**, 1013-1017 (2012).

[9] A. B. Kuzmenko, E. van Heumen, F. Carbone, and D. van der Marel. Universal Optical Conductance of Graphite. Phys. Rev. Lett. **100**, 117401 (2008).

[10] N.M. Gabor et al. Hot CarrierâĂŞAssisted Intrinsic Photoresponse in Graphene. Science **334**, 648-652 (2011).

[11] Q. Ma et al. Competing channels for hot-electron cooling in graphene. Phys. Rev. Lett. **112**, 247401 (2014).

[12] C.R. Dean et al. Boron nitride substrates for high-quality graphene electronics. Nature Nanotechnology **5**, 722-726 (2010.)

[13] K.K. Kim et al. Synthesis and Characterization of Hexagonal Boron Nitride Film as a Dielectric Layer for Graphene Devices. ACS Nano **6**, 8583-8590 (2012).

[14] Giovannetti, G., Khomyakov, P., Brocks, G., Karpan, V., van den Brink, J. & Kelly, P. Doping graphene with metal contacts. Phys. Rev. Lett. **101**, 026803 (2008).

[15] J. Martin et al. Observation of electronâĂŞhole puddles in graphene using a scanning single-electron transistor. Mature Physics **4**, 144-148 (2008).

[16] K. v. Klitzing. Metrology in 2019. Nature Physics **13**, 198 (2017.)

[17] C. Kittel. Introduction to Solid State Physics (John Wiley & Sons, 1996).

[18] J.J. Sakurai. Modern Quantum Mechanics, Revised Edition. (Addison-Wesley Publishing Company, Inc., 1994).

[19] M. O. Goerbig. Quantum Hall Effects. https://arxiv.org/pdf/0909.1998v2.pdf. Retrieved Apr 30 2018.

[20] Novoselov, K. S. et al. Two-dimensional gas of massless Dirac fermions in graphene. Nature **438**, 197-200, (2005).

[21] S. K. et al. Direct Measurement of the Fermi Energy in Graphene Using a Double-Layer Heterostructure. Phys. Rev. Lett. **108**, 116404 (2012).

[22] Lopes dos Santos, J. M. B., Peres, N. M. R. & Castro Neto, a. H. Graphene Bilayer with a Twist: Electronic Structure. Physical Review Letters **99**, 256802, (2007).

[23] S. Shallcross, S. Sharma, E. Kandelaki, and O. A. Pankratov. Electronic structure of turbostratic graphene. Phys. Rev. B **81**, 165105 (2010).

[24] S. Shallcross, S. Sharma, O. Pankratov, Phys. Rev. B **87**, 245403 (2013).

[25] J. M. B. Lopes dos Santos, N. M. R. Peres, A. H. Castro Neto, Phys. Rev. B **86**, 155449 (2012).

[26] A.Y. Kitaev. Unpaired Majorana fermions in quantum wires. Physics-Uspekhi **44** (2001).

[27] J. Nilsson, A. R. Akhmerov, and C. W. J. Beenakker. Splitting of a Cooper Pair by a Pair of Majorana Bound States. Phys. Rev. Lett. **101**, 120403 (2008).

[28] L. Fu and C.L. Kane. Probing Neutral Majorana Fermion Edge Modes with Charge Transport. Phys. Rev. Lett. **102**, 216403 (2009).

[29] B.A. Bernevig et al. Quantum Spin Hall Effect and Topological Phase Transition in HgTe Quantum Wells. Science **314**, 1757-1761 (2006).

[30] S. Wu et al. Observation of the quantum spin Hall effect up to 100 kelvin in a monolayer crystal. Science **359**, 76-79 (2018).

[31] C. L. Kane, E. J. Mele, Phys. Rev. Lett. 95, 146802 (2005).

[32] C. Wu, B. A. Bernevig, S. C. Zhang, Phys. Rev. Lett. 96, 106401 (2006).

[33] C. Xu, J. Moore, Phys. Rev. B 73, 045322 (2006).

[34] C. L. Kane and E. J. Mele. Quantum Spin Hall Effect in Graphene. Phys. Rev. Lett. **95**, 226801 (2005).

[35] M. Kharitonov. Phase diagram for the $\nu = 0$ quantum Hall state in monolayer graphene. Phys. Rev. B 85, 155439 (2012).

[36] Zhang, Y. B., Tan, Y. W., Stormer, H. L. & Kim, P. Experimental observation of the quantum Hall effect and Berry's phase in graphene. Nature **438**, 201-204, (2005).

[37] Bolotin, K. I., Ghahari, F., Shulman, M. D., Stormer, H. L. & Kim, P. Observation of the fractional quantum Hall effect in graphene. Nature **462**, 196-199, (2009).

[38] Du, X., Skachko, I., Duerr, F., Luican, A. & Andrei, E. Y. Fractional quantum Hall effect and insulating phase of Dirac electrons in graphene. Nature **462**, 192-195, (2009).

[39] Young, A. F. et al. Spin and valley quantum Hall ferromagnetism in graphene. Nature Physics **8**, 550-556, (2012).

[40] Young, A. F. et al. Tunable symmetry breaking and helical edge transport in a graphene quantum spin Hall state. Nature **505**, 528âĂŞ532, (2014).

[41] I. Armidor. (2009) The Theory of the Moiré Phenomenon, Volume I: Periodic Layers. London: Springer.

[42] G. Li et al. Scanning Tunneling Spectroscopy of Graphene on Graphite. Phys. Rev. Lett. **102**, 176804 (2009).

[43] G. Li, A. Luican, J. M. B. Lopes dos Santos, A. H. Castro Neto, A. Reina, J. Kong, E. Y. Andrei, Nature Phys. **6**, 109 (2010).

[44] Luican, A. et al. Single-Layer Behavior and Its Breakdown in Twisted Graphene Layers. Physical Review Letters **106**, 126802, (2011).

[45] T. Ohta, J. T. Robinson, P. J. Feibelman, A. Bostwick, E. Rotenberg, T. E. Beechem, Phys. Rev. Lett. **109**, 186807 (2012).

[46] D.R. Hofstadter. Energy levels and wave functions of Bloch electrons in rational and irrational magnetic fields. Phys. Rev. **B** 14, 2239 (1976).

[47] B. Hunt, J. D. Sanchez-Yamagishi, A. F. Young, M. Yankowitz, B. J. LeRoy, K. Watanabe, T. Taniguchi, P. Moon, M. Koshino, P. Jarillo-Herrero, R. C. Ashoori. Massive Dirac Fermions and Hofstadter Butterfly in a van der Waals Heterostructure. Science **340**, 1427-1430 (2013).

[48] C.R. Dean et al. HofstadterâĂŹs butterfly and the fractal quantum Hall effect in moiré superlattices. Nature **497**, 598âĂŞ602 (2013).

[49] L.A. Ponomarenko et al. Cloning of Dirac fermions in graphene superlattices. Nature **497**, 594âĂŞ597 (2013).

[50] G. Giovannetti et al. Substrate-induced band gap in graphene on hexagonal boron nitride: Ab initio density functional calculations. Phys. Rev. B **76**, 073103 (2007).

[51] Min, H., Hill, J. E., Sinitsyn, N. A., Sahu, B. R., Kleinman, L. & MacDonald, A. H. Intrinsic and Rashba spin-orbit interactions in graphene sheets. Phys. Rev. B **74**, 165310 (2006).

[52] Yao, Y., Ye, F., Qi, X.-L., Zhang, S.-C. & Fang, Z. Spin-orbit gap of graphene: First-principles calculations. Phys. Rev. B **75**, 041401 (2007).

[53] X. Wan et al. Fractional quantum Hall effect at $\nu = 5/2$: Ground states, non-Abelian quasiholes, and edge modes in a microscopic model. Phys. Rev. B **77**, 165316 (2008).

[54] C. Nayak et al. Non-Abelian anyons and topological quantum computation. Rev. Mod. Phys. **80**, 1083 (2008).

[55] J.K. Jain. Composite-fermion approach for the fractional quantum Hall effect. Phys. Rev. Lett. **63**, 199 (1989).

[56] B.I. Halperin. Composite fermions and the FermionâĂŞChernâĂŞSimons theory. Physica E **20**, 71-78 (2003).

[57] C.R. Dean et al. Multicomponent fractional quantum Hall effect in graphene. Nature Physics **7**, 693-696 (2011).

[58] Schmidt, H. et al. Tunable graphene system with two decoupled monolayers. Appl. Phys. Lett. **93**, 172108 (2008).

[59] Lee, D., Riedl, C., Beringer, T., Castro Neto, A., von Klitzing, K., Starke, U. & Smet, J. Quantum hall effect in twisted bilayer graphene. Phys. Rev. Lett. **107**, 216602 (2011).

[60] Sanchez-Yamagishi, J.D., Luo, J.Y. et al. Helical edge states and fractional quantum Hall effect in a graphene electronâĂŞhole bilayer. Nature Nanotechnology **12**, 118-122 (2016).

[61] Qi, X.-L. & Zhang, S.-C. Topological insulators and superconductors. Rev. Mod. Phys. **83**, 1057-1110, (2011).

[62] Lutchyn, R. M., Sau, J. D. & Das Sarma, S. Majorana Fermions and a Topological Phase Transition in Semiconductor-Superconductor Heterostructures. Physical Review Letters **105**, 077001, (2010).

[63] Oreg, Y., Refael, G. & von Oppen, F. Helical Liquids and Majorana Bound States in Quantum Wires. Physical Review Letters **105**, 177002, (2010).

[64] Hasan, M. Z. & Kane, C. L. Topological insulators. Rev. Mod. Phys. **82**, 3045-3067, (2010).

[65] Konig, M. et al. Quantum spin hall insulator state in HgTe quantum wells. Science **318**, 766-770, (2007).

[66] Knez, I., Du, R.-R. & Sullivan, G. Evidence for Helical Edge Modes in Inverted InAs/GaSb Quantum Wells. Physical Review Letters **107**, 136603, (2011).

[67] Mourik, V. et al. Signatures of Majorana Fermions in Hybrid Superconductor-Semiconductor Nanowire Devices. Science **336**, 1003-1007, (2012).

[68] Lindner, N. H., Berg, E., Refael, G. & Stern, A. Fractionalizing Majorana Fermions: Non-Abelian Statistics on the Edges of Abelian Quantum Hall States. Physical Review X **2**, 041002, (2012).

[69] Cheng, M. Superconducting proximity effect on the edge of fractional topological insulators. Physical Review B **86**, 195126, (2012).

[70] Clarke, D. J., Alicea, J. & Shtengel, K. Exotic non-Abelian anyons from conventional fractional quantum Hall states. Nat Commun **4**, 1348, (2013).

[71] Barkeshli, M. & Qi, X.-L. Synthetic Topological Qubits in Conventional Bilayer Quantum Hall Systems. Physical Review X **4**, 041035, (2014).

[72] Gusev, G. M. et al. Nonlocal Transport Near Charge Neutrality Point in a Two-Dimensional Electron-Hole System. Physical Review Letters **108**, 226804, (2012).

[73] Nichele, F. et al. Insulating State and Giant Nonlocal Response in an In As/Ga Sb Quantum Well in the Quantum Hall Regime. Physical Review Letters **112**, 036802, (2014).

[74] Abanin, D. A., Lee, P. A. & Levitov, L. S. Spin-filtered edge states and quantum Hall effect in graphene. Phys Rev Lett **96**, 176803, (2006).

[75] Fertig, H. A. & Brey, L. Luttinger Liquid at the Edge of Undoped Graphene in a Strong Magnetic Field. Phys. Rev. Lett. **97**, 116805, (2006).

[76] Maher, P. et al. Evidence for a spin phase transition at charge neutrality in bilayer graphene. Nature Physics **9**, 154-158, (2013).

[77] Amet, F., Williams, J. R., Watanabe, K., Taniguchi, T. & Goldhaber-Gordon, D. Selective Equilibration of Spin-Polarized Quantum Hall Edge States in Graphene. Physical Review Letters **112**, 196601, (2014).

[78] de Gail, R., Goerbig, M. O., Guinea, F., Montambaux, G. & Castro Neto, A. H. Topologically protected zero modes in twisted bilayer graphene. Physical Review B **84**, 045436, (2011).

[79] Choi, M.-Y., Hyun, Y.-H. & Kim, Y. Angle dependence of the Landau level spectrum in twisted bilayer graphene. Physical Review B **84**, 195437, (2011).

[80] Moon, P. & Koshino, M. Energy spectrum and quantum Hall effect in twisted bilayer graphene. Physical Review B **85**, 195458, (2012).

[81] Novoselov, K. S. et al. Unconventional quantum Hall effect and BerryâĂŹs phase of 2π in bilayer graphene. Nature Physics **2**, 177-180, (2006).

[82] Sanchez-Yamagishi, J. D. et al. Quantum Hall Effect, Screening, and Layer-Polarized Insulating States in Twisted Bilayer Graphene. Physical Review Letters **108**, 076601, (2012).

[83] Schmidt, H., LÃijdtke, T., Barthold, P. & Haug, R. J. Mobilities and scattering times in decoupled graphene monolayers. Physical Review B **81**, 121403(R), (2010).

[84] Zhang, Y. et al. Landau-level splitting in graphene in high magnetic fields. Physical Review Letters **96**, 136806, (2006).

[85] Checkelsky, J. G., Li, L. & Ong, N. P. Zero-Energy State in Graphene in a High Magnetic Field. Phys. Rev. Lett. **100**, 206801, (2008).

[86] Wang, L. et al. One-dimensional electrical contact to a two-dimensional material. Science 342, 614-617, (2013).

[87] Zomer, P. J., GuimarÃčes, M. H. D., Brant, J. C., Tombros, N. & van Wees, B. J. Fast pick up technique for high quality heterostructures of bilayer graphene and hexagonal boron nitride. Applied Physics Letters **105**, 013101, (2014).

[88] Mayorov, A. S. et al. Micrometer-Scale Ballistic Transport in Encapsulated Graphene at Room Temperature. Nano Letters **11**, 2396-2399, (2011).

[89] A.M. Chang, L.N. Pfeiffer, and K.W. West. Observation of Chiral Luttinger Behavior in Electron Tunneling into Fractional Quantum Hall Edges. Phys. Rev. Lett. **77**, 2538 (1996).

[90] M. Grayson, D.C. Tsui, L.N. Pfeiffer, K.W. West, and A.M. Chang. Continuum of Chiral Luttinger Liquids at the Fractional Quantum Hall Edge. Phys. Rev. Lett. **80**, 1062 (1998).

[91] A.M. Chang, M.K. Wu, J.C.C. Chi, L.N. Pfeiffer, & K.W. West. Plateau Behavior in the Chiral Luttinger Liquid Exponent. Phys. Rev. Lett. **86**, 143 (2001).

[92] J. R. Wallbank, A. A. Patel, M. Mucha-Kruczynski, A. K. Geim, V. I. Fal'ko, Phys. Rev. B **87**, 245408 (2013).

[93] Cao, Y., Luo, J.Y. et al. Superlattice-Induced Insulating States and Valley-Protected Orbits in Twisted Bilayer Graphene. Phys. Rev. Lett. **117**, 116804 (2016).

[94] A. K. Geim, I. V. Grigorieva. Nature. **499**, 419-425 (2013).

[95] C. R. Woods, L. Britnell, A. Eckmann, R. S. Ma, J. C. Lu, H. M. Guo, X. Lin, G. L. Yu, Y. Cao, R. V. Gorbachev, *et al.* Nature Phys. **10**, 451-456 (2014).

[96] J. Jung, A. M. DaSilva, A. H. MacDonald, S. Adam, Nature Comm. **6**, 6308 (2015).

[97] P. San-Jose, A. Gutiérrez-Rubio, M. Sturla, F. Guinea, Phys. Rev. B **90**, 075428 (2014).

[98] J. C. W. Song, A. V. Shytov, L. S. Levitov, Phys. Rev. Lett. **111**, 266801 (2013).

[99] E. J. Mele, Phys. Rev. B **81**, 161405 (2010).

[100] E. J. Mele, Phys. Rev. B **84**, 235439 (2011).

[101] R. Bistritzer, A. H. MacDonald, Proc. Natl. Acad. Sci. U. S. A. **108**(30), 12233-12237 (2011).

[102] R. W. Havener, Y. Liang, L. Brown, L. Yang, J. Park, Nano Lett. **14**, 3353 (2014).

[103] W. Yan, M. Liu, R.-F. Dou, L. Meng, L. Feng, Z.-D. Chu, Y. Zhang, Z. Liu, J. C. Nie, L. He, Phys. Rev. Lett. **109**, 126801 (2012).

[104] I. Brihuega, P. Mallet, H. González-Herrero, G. Trambly de Laissardière, M. M. Ugeda, L. Maguad, J. M. Gómez-Rodríguez, F. Ynduráin, J.-Y. Veuillen, Phys. Rev. Lett. **109**, 196802 (2012).

[105] E. Suárez Morell, J. D. Correa, P. Vargas, M. Pacheco, Z. Barticevic, Phys. Rev. B **82**, 121407 (2010).

[106] S. Fang, E. Kaxiras, Phys. Rev. B **93**, 235153 (2016).

[107] D. S. Lee, C. Riedl, T. Beringer, A. H. Castro Neto, K. von Klitzing, U. Starke, J. H. Smet, Phys. Rev. Lett. **107**, 216602 (2011).

[108] H. Schmidt, J. C. Rode, D. Smirnov, R. J. Haug, Nature Comm. **5**, 5742 (2014).

[109] See Appendix B.

[110] K. Kim, M. Yankowitz, B. Fallahazad, S. Kang, H. C. P. Movva, S. Huang, S. Larentiz, C. M. Corbet, T. Taniguchi, K. Watanabe, *et al.* Nano Lett. **16**, 1989 (2016).

[111] N. F. Mott, J. Non-Cryst. Solids **1**, 1 (1968).

[112] D. Jérome, T. M. Rice, W. Kohn, Phys. Rev. **158**, 462 (1967).

[113] R. Nandkishore, L. Levitov, Phys. Rev. Lett. **104**, 156803 (2010).

[114] W. Bao, J. Velasco Jr., F. Zhang, L. Jing, B. Standley, D. Smirnov, M. Bockrath, A. H. MacDonald, C. N. Lau, Proc. Natl. Acad. Sci. U. S. A. **109**(27), 10802-10805 (2012).

[115] During the preparation of this manuscript we became aware of Y. Kim, P. Herlinger, P. Moon, M. Koshino, T. Taniguchi, K. Watanabe, J. H. Smet, arXiv:1605.05475 (2016).

[116] S. Fang, R. Kuate Defo, S. N. Shirodkar, S. Lieu, G. A. Tritsaris, E. Kaxiras, Phys. Rev. B **92**, 205108 (2015).

[117] G. W. Martin, D. L. Maslov, M. Y. Reizer, Phys. Rev. B **68**, 241309 (2003).

[118] It could also be the case that any hybridization is so small that magnetic breakdown has already occurred, as outlined in D. Shoenberg, *Magnetic Oscillations in Metals* (Cambridge University Press, Cambridge, 1984), Chap. 7.

[119] Y. Cao et al. Correlated insulator behaviour at half-filling in magic-angle graphene superlattices. Nature **556**, 80-84 (2018).

[120] Y. Cao et al. Unconventional superconductivity in magic-angle graphene superlattices. Nature **556**, 43-50 (2018).

[121] McCann, E. Asymmetry gap in the electronic band structure of bilayer graphene. Physical Review B 74 (2006).

[122] Taychatanapat, T. & Jarillo-Herrero, P. Electronic Transport in Dual-Gated Bilayer Graphene at Large Displacement Fields. Physical Review Letters, 105 (2010).

[123] K. Kim *et al.* Nano Lett. **16** 1989 (2016).

[124] K. Kim, S. Coh, *et. al.* Phys. Rev. Lett. **108**, 246103 (2012).

[125] J. P. Perdew, K. Burke, M. Ernzerhof, Phys. Rev. Lett. **77**, 3865 (1996).

[126] P. Moon, Y.-W. Son, M. Koshino, Phys. Rev. B **90**, 155427 (2014).

[127] T. Ohta *et al.* Science **313**, 951 (2006).

[128] J. B. Oostinga *et al.* Nature Mater. **7**, 151 (2008).

[129] Y. Zhang *et al.* Nature **459**, 820 (2009).

[130] J. C. Rode, D. Smirnov, H. Schmidt, R. J. Haug, arXiv:1603.04806.